OPTICAL SIGNAL PROCESSING WITH PHOTOREFRACTIVE MATERIALS

by

Sakellaris Mailis

Thesis submitted to the

Physics Department

University of Crete

for the degree of

Doctor of Philosophy in Physics.

HERAKLION

1996

ΝΔ : 10982
Κοε : 7905

ΕΘΝΙΚΟ ΚΕΝΤΡΟ ΤΕΚΜΗΡΙΩΣΗΣ
ΒΙΒΛΙΟΘΗΚΗ
13 ΜΑΙ. 1999

OPTICAL SIGNAL PROCESSING WITH PHOTOREFRACTIVE MATERIALS

by

Sakellaris Mailis

Thesis submitted to the

Physics Department

University of Crete

for the degree of

Doctor of Philosophy in Physics.

HERAKLION

1996

Στην Σοφία

ACKNOWLEDGMENTS

I express my gratitude to the people that helped me complete this work.

First, I would like to acknowledge the contribution of Dr. N. A. Vainos who introduced me to the subject. His guidance, steady encouragement and friendly attitude helped me throughout the many difficulties encountered along the way.

Many thanks to Professor C. Fotakis for his support during the course of my graduate studies. His very early advise is the reason for my studying at the University of Crete.

I am also grateful to Professor R. W. Eason for his very insightful advise and Dr. L. Boutsikaris for his invaluable help and fruitful discussions. I would also like to acknowledge the many interesting discussions with Professor D. Charalambidis on many subjects of general Physics.

I am deeply grateful to the Foundation for Research and Technology-Hellas (FORTH) for financial support throughout my graduate studies.

I wish to thank my family. Without their moral support this work would have never been completed.

Finally, it is with gratitude that I acknowledge all my friends at IESL that stood by me in good and bad times.

TABLE OF CONTENTS

LIST OF FIGURES

Figure Page

LIST OF TABLES

Table Page

ABSTRACT

Current advances in information technologies have stimulated a progressive interaction between "optics" and "information". In this context, non-linear optics and holography constitute alternative solutions, that establish new frontiers. The development of new dynamic holographic recorders, coupled with the understanding of their fundamental interaction with light, lead to novel information storage and processing methods. The present study focuses on the above issues.

A photorefractive barium titanate based system capable of performing coherent pulsed amplification of a weak continuous wave signal is demonstrated. The very large net amplification gain attained by this system implies great prospects in low light level cinehology.

A photorefractive adaptive transmission system based on the combined action of a photorefractive strontium barium niobate amplifier and a self-pumped barium titanate phase conjugator is presented. This system is capable of producing an amplified real-time phase conjugate replica of a weak signal beam, and simultaneously interchanging high frequency information between beams by utilizing the dynamic grating inertia. A multi-beam configuration which establishes an adaptive

linking scheme between different information channels is discussed here.

Bipolar photorefraction in photorefractive bismuth silicate in the near infrared (780nm) is observed. The dynamic behavior of this phenomenon is studied both experimentally and theoretically and a method for the determination of important materials parameters is developed. Demonstration of image processing and incoherent-to-coherent spatial information transfer underlines some application aspects of this work.

In the search for new holographic recording media, indium oxide and indium-tin-oxide polycrystalline and amorphous thin films are investigated. Ultraviolet radiation is used for highly efficient dynamic holographic recording in films grown by DC magnetron sputtering and pulsed laser deposition. Even though the nature of the effects involved is not fully comprehended, the applications explored verify the potential of these materials in the area of optical information storage and processing.

Chapter 1

INTRODUCTION

1.1 Optics in information storage and processing

In recent years, the steadily increasing information capacity demands, drive the efforts towards higher storage density and urges the development of new devices and parallel system architectures.

Serial, one or two dimensional, magnetic or optical recording technology represents the state-of-the-art in data storage devices. The serial mode of operation limits, however, the data processing speed. Significant progress in increasing access time has been performed by the development of new techniques but the limits of the serial mode of operation are still evident.

Holography provides an alternative solution to the above problem by introducing a novel new "parallel" approach for storing data. High density storage is possible, especially if short wavelengths are used, via multiplexing of holograms in the same photosensitive volume, exploiting both the high information content of a hologram and the capability for parallel processing. Research is not only directed towards new photosensitive materials but also focuses on new methods, and components that can also support the development, integration and

adaptation of this new technology. User-interfacing, having gone through a long period of development, is now very well established. The main advantages of the new technology, such as the high capacity, the parallel mode of operation and a relatively high speed that result in large data rates, may be exploited in the "heart" of a system utilizing all-optical information storage and processing methods.

Parallel information handling is a powerful way to increase substantially the processing speed. This fact has been realized by the computer industry and new methods and techniques, such as multistack technology in microelectronic devices, have already been implemented although problems of heat and cross talk between neighbor circuits continue to exist.

Optical signals can be considered as two dimensional arrays of pixels where every pixel can be amplitude and/or phase modulated. The simplest form of such an optical signal may be a single image. It is then understood that all the pixels constituting the image can be processed simultaneously. This important property, combined with high intensity of coherent laser radiation, is thus establishing the technique of coherent information processing and enhances the potential of optical systems.

A simple converging lens has the ability, when used with coherent radiation, to perform a speed-of-light complex operation of the two

dimensional Fourier transformation, which is the basis for many coherent data processing applications. Electronically this operation would require the use of rather complicated and dedicated electronic spectrum analyzers or rather slow processing software.

In extending the above schemes, dynamic holographic methods provide a novel perspective by introducing real time hologram processing and recording. Furthermore, the dynamic recording nature yields a series of novel laser matter interaction effects and associated information processing methods yet to be understood and further exploited.

1.2 The optical Fourier transform: a basic operation.

When coherent radiation is used for the illumination of a transparent object, placed at the front focal plane P_1 of a lens L_1 of focal length f, then the amplitude distribution of the electric field at the back focal plane P_2 of the lens represents the complex Fourier transform[1] of the amplitude transmittance at plane P_1 (Figure 1.1)

Let the amplitude transmittance function of the object be $t_0(x_0,y_0)$. If the object is illuminated by a plane wave of amplitude A then the field distribution on the plane P_1 will be:

$$U(x_0, y_0) = A\, t_0(x_0, y_0) \qquad (1.1)$$

where x_0, y_0 are the coordinates on the plane P_1

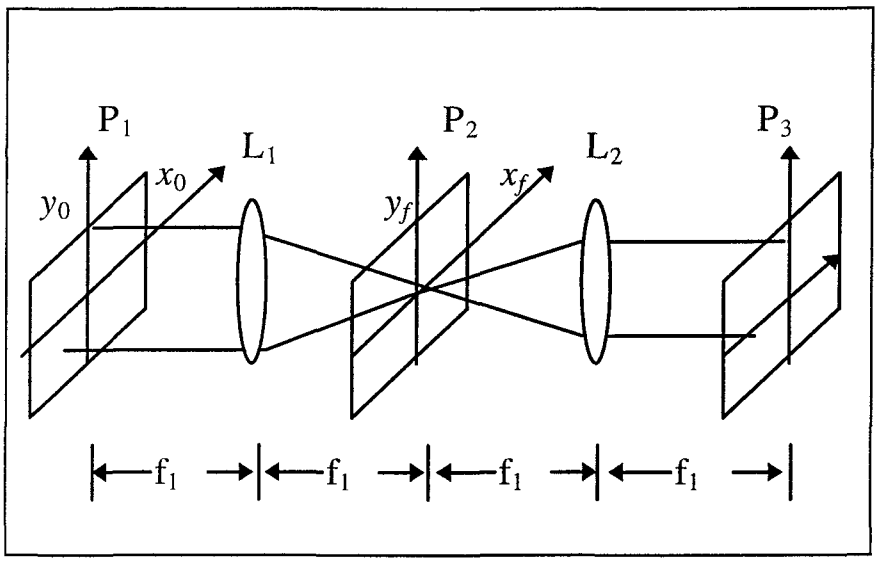

Figure 1.1 Set up for the realization of optical Fourier transform.

The Fourier spectrum of the object function will be:

$$F_0(\frac{x_f}{\lambda f},\frac{y_f}{\lambda f}) = \mathcal{F}\{At_0(x_0,y_0)\} \tag{1.2}$$

$$\text{where } \mathcal{F}\{At_0\} = \iint_{\infty} At_0(x_0,y_0)e^{[-i2\pi(\frac{x_f}{\lambda f}x_0+\frac{y_f}{\lambda f}y_0)]}dx_0dy_0 \tag{1.3}$$

The Fourier spectrum, F_l, incident on the lens L_1 will be related to F_0 by the following expression which describes the Fresnel diffraction at a distance f in the spatial frequency domain:

$$F_l(\frac{x_f}{\lambda f},\frac{y_f}{\lambda f}) = F_0(\frac{x_f}{\lambda f},\frac{y_f}{\lambda f})e^{[-i\pi\lambda f(\frac{x_f}{\lambda f}^2+\frac{y_f}{\lambda f}^2)]} \tag{1.4}$$

Where λ is the wavelength of the plane wave and x_f, y_f are the coordinates at the plane P_2. A constant phase factor has been neglected.

In order to find the amplitude distribution at the back focal plane of the lens, the Fresnel diffraction formula is applied

$$U_f(x_f, y_f) = \frac{e^{[i\frac{k}{2f}(x_f^2+y_f^2)]}}{i\lambda f}\iint_{\infty} U_1'(x,y)e^{[i\frac{k}{2f}(x^2+y^2)]}e^{[-i\frac{k}{2f}(xx_f+yy_f)]}dxdy \qquad (1.5)$$

Where x, y are the coordinates at the plane of L_1 and

$$U_1'(x,y) = U_1(x,y)e^{[-i\frac{k}{2f}(x^2+y^2)]} \qquad (1.6)$$

thus the amplitude distribution on the plane P_2 is given by:

$$U_f(x_f, y_f) = \frac{e^{[i\frac{k}{2f}(x_f^2+y_f^2)]}}{i\lambda f}F_1(\frac{x_f}{\lambda f}, \frac{y_f}{\lambda f}) \qquad (1.7)$$

By substituting equation (1.4) into equation (1.7) it takes the form:

$$U_f(x_f, y_f) = \frac{1}{i\lambda f}F_0(\frac{x_f}{\lambda f}, \frac{y_f}{\lambda f}) = \frac{A}{i\lambda f}\mathcal{F}\{t_0(x_0, y_0)\} \qquad (1.8)$$

which is the exact Fourier transform of the amplitude transmittance in the front focal plane of the ideal lens P_1. We must note here that in the previous analysis, the finite extent of the lens was totally ignored. In order to produce the exact Fourier transformation attention must be paid to the fact that the object must be small as compared to the dimensions of the lens, to minimize geometric vignetting. In a double

diffraction arrangement (Figure 1.1), a lens L_2 (identical to L_1) is placed at a distance f from P_2 as shown. The original amplitude transmittance is reconstructed at the back focal plane P_3 of lens L_2, by performing a second Fourier transform operation.

It must be noted here that the above described operation is bandwith limited, as there is only a certain number of diffracted field components (limited by diffraction and available aperture) that will be transmitted through the system and will be present at the output plane P_3.

By using appropriate masks at the Fourier plane P_2 shown in Figure 1.1specific spatial frequencies can, for example, be selected leading to geometric spatial filtering of the input image. Several filtering operations can be performed by this scheme, such as high, low or bandpass filtering.

Holography[2] however, enables the construction of diffractive, complex, Fourier plane filters capable of performing complicated processing operations, extending potential applications in image processing and pattern recognition and analysis.

1.3 Holography

The word "holography" comes from the Greek words "holos" denoting "the total" or "the complete" and "graphy" meaning "recording". It

describes "the total recording of optical information" that is the recording of both intensity and phase information of the coherent radiation diffracted or reflected off an object.

A hologram is produced by recording the interference between a beam scattered off a coherently illuminated object and a coherent reference wave, in the volume of a photosensitive material. Subsequent reillumination of the developed "hologram" with a wave proportional to the reference field, produces a field distribution proportional to the original image field, thus reconstructing a three dimensional image of the object. In contrast to "photography", it is the encoded phase information which is responsible for the reconstruction of the three dimensional characteristics in the reconstructed image. Furthermore, it is worth underlining the issue of information association, meaning that a single hologram enables the retrieval of each one wave by the other present in recording.

In the simple case of an absorption hologram, a photosensitive film may be used. Let $\mathcal{S}$ and $\mathcal{R}$ be the complex amplitudes of the object and reference waves incident on the holographic medium respectively $\mathcal{S}$=Sexp[$i\phi$(r)] and $\mathcal{R}$=R for a plane wave reference, as it is depicted in Figure 1.2 . A single beam is used here to provide both reference and object illuminating beams.

The amplitude transmittance t, defined as the amplitude of the transmitted light divided by the amplitude of the incident light, of the

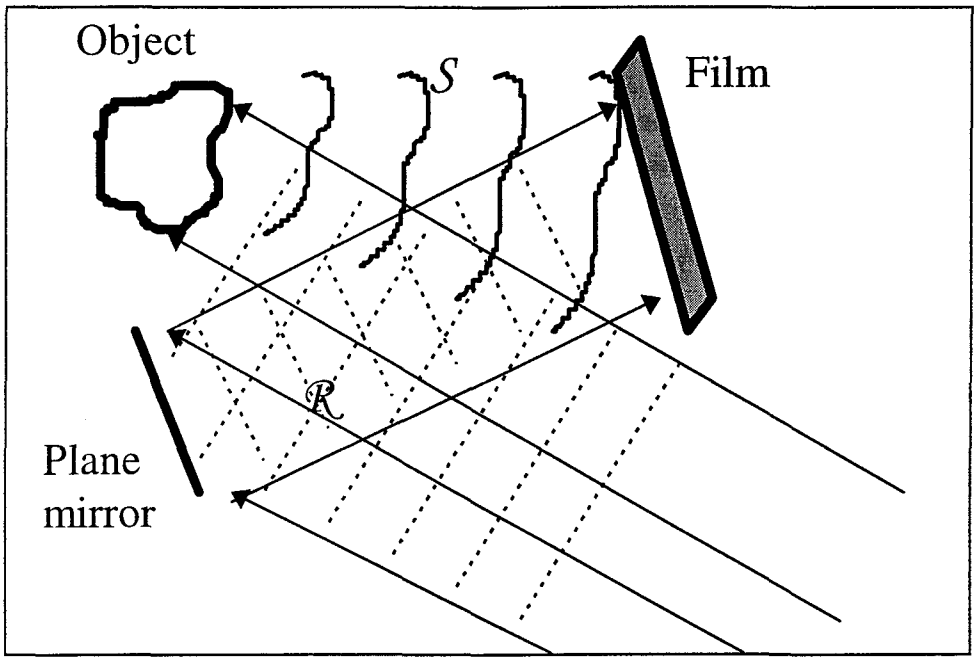

Figure 1.2 Schematic of holographic recording. S and R are the object and reference waves respectively.

exposed film is $t=t_0-kI$, (when the exposure value lies in the linear region of the film sensitivity curve), where t_0 is the amplitude transmittance of the unexposed film and k is a constant. The light intensity distribution on the film, during recording, is given by:

$$I = (S+R)(S+R)^* = I_S + I_R + SR^* + RS^* \qquad (1.9)$$

Where I_S and I_R are proportional to SS^* and RR^* respectively.

For the reconstruction of wavefront S the developed hologram is illuminated by R. The resulting complex wave amplitude, W, is the product of R by the hologram transmittance t.

$$W \propto \mathcal{R}I = \mathcal{R}(I_S + I_R) + \mathcal{R}\mathcal{S}^*\mathcal{R} + \mathcal{S}I_R \qquad (1.10)$$

Every term in equation (1.10) represents a diffracted wave emerging from the hologram. The last term, however, is analogous to $\mathcal{S}$ and represents the reconstruction of a wavefront proportional to that produced from the original object during recording. The second term corresponds to the real image of the object and for thick holograms it does not radiate due to violation of the phase matching conditions. Reconstruction of the wavefront permits the viewer to observe a virtual image of the object and a schematic of this geometry is presented in Figure 1.3 (a). A real image of the object, can also be generated from the recorded hologram by illuminating with a wave which is the phase conjugate to the reference wave, as depicted in Figure 1.3 (b).

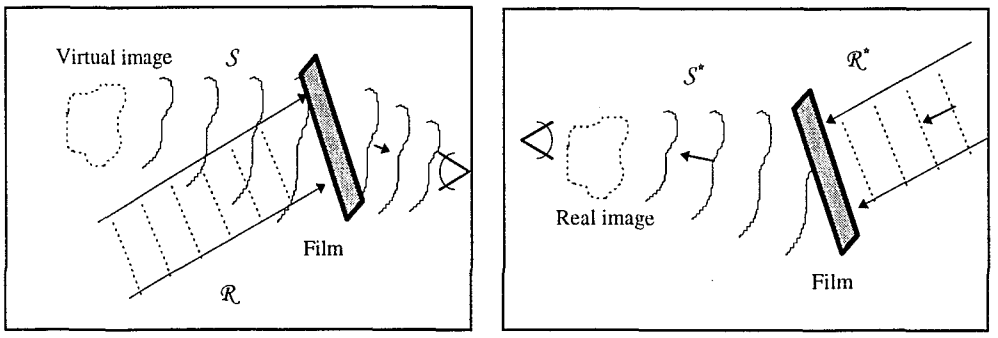

Figure 1.3 a) Reconstruction of the hologram using the reference wave $\mathcal{R}$ for hologram illumination, producing a virtual image and b) using the phase conjugate reference wave $\mathcal{R}^*$ for hologram illumination, producing a real image.

In this case the amplitude transmittance of the hologram will be:

$$W' \propto \mathcal{R}^* I = \mathcal{R}^* (I_S + I_R) + I_R S^* + \mathcal{R}^* \mathcal{R}^* S \qquad (1.11)$$

where the second term is proportional to S^*, which is the phase conjugate replica of the wave scattered off the original object while the third term corresponds now to the virtual image of the object and it is not radiating for thick holograms. The wave corresponding to the second term converges forming the real image of the original object. However, the phase conjugate nature of the wave results in an inverted image perspective and therefore peculiar parallax properties (pseudoscopic image).

With the use of holographic filters, complicated image processing and pattern recognition operations can be realized. By utilizing suitable arrangements, all optical correlation and convolution between optical signals, image synthesis operations such as addition and subtraction and also more advanced operations like image differentiation and deconvolution are possible[1].

All the above mentioned applications, and many more, can be realized with the use of dynamic optical recording materials. Photorefractive (PR) materials, in which holograms are dynamically recorded and erased in real time, are now exploited in such applications. Real-time holographic methods lead to numerous applications from real-time phase conjugation and coherent amplification, to image synthesis, correlation, convolution and adaptive transmission of signals.

1.4 Dynamic holography and the "Photorefractive effect"

Dynamic holography started developing after the discovery (by Ashkin *et al.*[3] at Bell Labs) of "optical damage" by intense laser pulses in a class of electrooptic nonlinear crystals. The laser pulses were seen to induce semipermanent refractive index changes that ruined phase matching conditions for second harmonic generation in $LiNbO_3$ and $LiTaO_3$. It thus became clear that this "optical damage" could be used for holographic recording. In 1968, Chen *et al.*[4] used this effect for high density optical storage of data. This effect was thereafter called "the photorefractive effect" and it essentially comprises the change of refractive index upon illumination with light.

Materials exhibiting photorefractive (PR) behavior are both photoconductive and electrooptic. An optical intensity distribution, produced for example by the interference of two waves in a photorefractive material, causes excitation and redistribution of charges. The optical field in the highly illuminated areas excites charge carriers, from donor states, N_D, lying in the band gap, to the conduction band. The carriers diffuse (or drift in the presence of an externally applied field) and get retrapped by ionized donors, N_D^+, or other trapping states as depicted in Figure 1.4 , thus establishing a space charge distribution.

This resultant space charge distribution is associated with a space

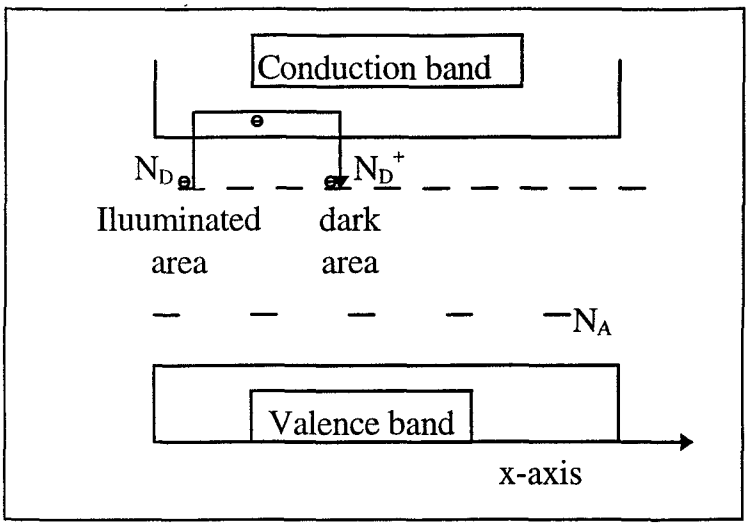

ΚΕΝΤΡΟ ΤΕΚΜΗΡΙΩΣΗΣ ΒΙΒΛΙΟΘΗΚΗ

Figure 1.4 Schematic the charge transport during the photorefractive process.

charge field which in turn modulates the index of refraction of the material, Δn, via the linear electrooptic effect. In effect this spatial modulation of the refractive index is a refractive index hologram with $\Delta n = -\frac{1}{2} n^3 r_{eff} E_{SC}$, where n is the background index of refraction, r_{eff} is the effective electrooptic coefficient (a linear combination of the electrooptic tensor components), and E_{SC} is the space charge field established in the material. It must be noted that the above represents a dynamic situation as at any change of the intensity distribution follows, within a certain response time which depends on the material properties, a corresponding change of the actual holographic pattern.

A schematic of the grating distribution is depicted in Figure 1.5 where sinusoidal illumination is assumed for simplicity as it is resulting from the interference of two plane waves.

The first theoretical modeling of the "photorefractive effect" was given

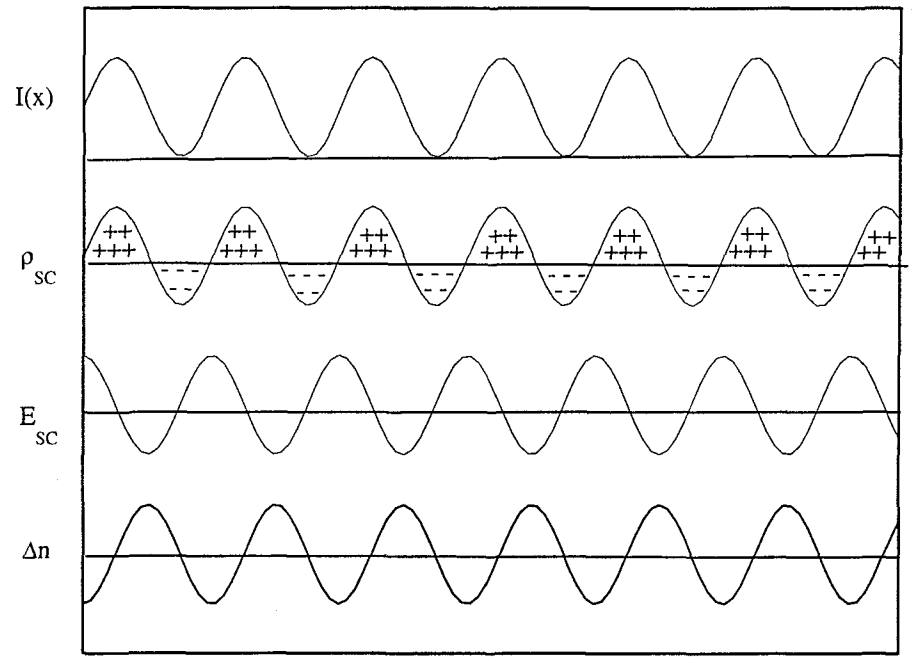

Figure 1.5 Schematic of the hologram formation procedure, in photorefractive crystals. I(x): intensity pattern, ρ_{SC}: space charge density, E_{SC}: space charge field, Δn: refractive index distribution.

by Chen[5] but a complete widely acceptable model was published by Kukhtarev *et al.*[6] later in 1979.

1.4.1 Formation of the PR grating

Assuming two plane waves $\mathcal{S}=S\exp[i(k_1 r-\omega t)]$ and $\mathcal{R}=R\exp[i(k_2 r-\omega t)]$ of the same frequency incident on the crystal with an angle ϑ between them, the resulting interference pattern can be described as follows.

$$I=(\mathcal{S}+\mathcal{R})(\mathcal{S}+\mathcal{R})^{*}=I_0[1+\frac{2\sqrt{I_S I_R}}{I_0}\cos(Kx)] \qquad (1.12)$$

Where $\mathbf{K} = \mathbf{k}_1 - \mathbf{k}_2$ is the grating wavevector, $K=|\mathbf{K}| = \frac{2\pi}{\Lambda}$, Λ is the fringe spacing, $\Lambda = \frac{\lambda}{2\sin(\frac{\vartheta}{2})}$, λ is the free space wavelength of the incident waves, ϑ is measured outside the crystal and $I_0=I_S+I_R$, represents the total intensity

The quantity defined as: $m = \frac{2\sqrt{I_S I_R}}{I_0}$ is the fringe modulation depth or index modulation and represents a very important parameter. Following the previously outlined approach, grating formation is based on combined charge excitation, transport, trapping, and electrooptic modulation of the refractive index. A full analysis of the effects is detailed in ANNEX 1. Analytical solution of the band transport equations can be given under the following assumptions.

i. The crystal is not conductive in the absence of illumination, therefore the ionized donor number density, N_D^+, exceeds the free electron, n, density, ($N_D^+ >> n$).

ii. The total density of donors, N_D, is much greater than ionized donors, N_D^+, ($N_D >> N_D^+$).

iii. Photoexcitation dominates thermal excitation, ($s >> \beta$)

iv. The grating wavevector, K, is parallel to the x-axis, so that only derivatives with respect to x coordinate are considered

v. There are no photovoltaic currents so the photovoltaic tensor, p, is zero.

Under these assumptions, the band transport equations are modified as follows.

$$\frac{\partial n}{\partial t} = \frac{1}{e}\frac{\partial J}{\partial x} \tag{1.13}$$

$$\frac{\partial N_D^+}{\partial t} = sIN_D - \gamma n N_D^+ \tag{1.14}$$

$$J = e\mu n(E_{SC} - E_0) - k_B T\mu \frac{\partial n}{\partial x} \tag{1.15}$$

$$\frac{\partial E_{SC}}{\partial x} = \frac{e}{\varepsilon_0 \varepsilon_r}(N_A - N_D^+) \tag{1.16}$$

Using the charge conservation principle $\frac{\partial J}{\partial x} = -\frac{\partial \rho}{\partial t}$ along with equations (1.15) and (1.16), an equation for the temporal evolution of the space charge field can be obtained.

$$\frac{\partial E_{SC}}{\partial t} = -\frac{e}{\varepsilon_0 \varepsilon_r}[\mu n(E_{SC} - E_0) - \frac{k_B T\mu}{e}\frac{\partial n}{\partial x}] \tag{1.17}$$

In the analysis presented here, only the first Fourier component of the space charge field is considered, and that leads to some more assumptions concerning the spatially modulated terms. There are two theoretical approaches to this problem. The first one proposed by Moharam *et al.*[7] is valid for all values of the modulation index, m, but

only for large values of fringe spacing, Λ. The other method, proposed by Kukhtarev[6], is using m as the perturbation parameter and is valid for all values of Λ. According to the second approach contributions of higher spatial harmonics are neglected for small values of m, so that the solutions of the band transport equations can be expressed as follows.

$$J = J_0 + (J_1 e^{iKx} + c.c) \tag{1.18}$$

$$n = n_0 + (n_1 e^{iKx} + c.c) \tag{1.19}$$

$$E_{SC} = E_{SC_0} + (E_{SC_1} e^{iKx} + c.c) \tag{1.20}$$

By substituting the above expressions into equation (1.17) and neglecting quadratic terms of the first Fourier components, an equation for the time evolution of the first Fourier component of the space charge field is obtained.

$$\frac{\partial E_{SC_1}}{\partial t} = -\frac{e}{\varepsilon_0 \varepsilon_r}[\mu(n_0 E_{SC_1} + n_1 E_{SC_0}) - \frac{k_B T \mu}{e} iKn_1] \tag{1.21}$$

Expressions for the zeroth and first component of the electron number density can be obtained by substituting equation (1.19) and (1.12) into the materials' equations:

$$n_0 = \frac{sI_0 N_D}{\gamma N_A} \tag{1.22}$$

$$n_1 = \frac{n_0[m + iE_{SC_1}(\frac{K\varepsilon_0\varepsilon_r}{eN_A} - \frac{\mu K}{\gamma N_A})]}{1 + (iE_{SC_0} + \frac{k_B TK}{e})(\frac{\gamma N_A}{\mu K})^{-1}} \tag{1.23}$$

Substituting the above results in equation (1.21) a final form for the evolution of the space charge field is obtained.

$$\frac{\partial E_{SC_1}}{\partial t} = -\frac{(1 + \frac{E_D}{E_q} + i\frac{E_0}{E_q})E_{SC_1}}{\tau_M(1 + \frac{E_D}{E_M} + i\frac{E_0}{E_M})} + \frac{m(iE_D - E_0)}{\tau_M(1 + \frac{E_D}{E_M} + i\frac{E_0}{E_M})} \tag{1.24}$$

Where: $E_D = \frac{k_B TK}{e}$ is the diffusion field,

$E_q = \frac{eN_A}{\varepsilon_0\varepsilon_r K}$ is the saturation field (the largest space-charge field that can be obtained in the crystal at K grating wavevector),

$E_M = \frac{1}{\mu\tau K}$,

E_0 is an externally applied electric field

$\tau = \frac{1}{\gamma N_A}$ is the photoexcited charge recombination time,

$\tau_M = \frac{\varepsilon_0\varepsilon_r}{e\mu n_0}$ is the dielectric relaxation time.

The steady state solution for the space charge field is obtained by setting $\frac{\partial E_{SC_1}}{\partial t} = 0$ in equation (1.24) and is given by:

$$E_{SC_1} = \frac{m(iE_D - E_0)}{1 + \frac{E_D}{E_q} + i\frac{E_0}{E_q}} \tag{1.25}$$

The complex form of the above expression for the space charge field describes the existence of a phase shift between the space charge field, and consequently the index of refraction, and the intensity interference pattern.

In the absence of an external applied field, the expression for the space charge field becomes purely imaginary giving a phase shift of $\pm\pi/2$ (depending on the sign of carriers) between the intensity interference pattern and the refractive index grating which leads in effect to a very useful energy exchange between the two recording beams as described below.

1.4.2 Photorefractive two beam coupling

In the grating formation process described in the previous section, the resulting index of refraction distribution is $\pi/2$ shifted, with respect to the intensity distribution of the incident waves, if no external electric field is applied to the crystal. The refractive index grating formed in the crystal is able to diffract both participating waves (self diffraction), causing a redistribution of energy between the two waves. The part of each wave diffracted in the direction of the other wave, suffers a $\pm\ \pi/2$ phase shift, depending on the direction of diffraction. This shift adds to the $-\pi/2$ phase shift, produced on diffraction by a dielectric grating[8]. The result is the observation of constructive interference between transmitted and diffracted optical waves in the direction of zero total phase difference, and destructive interference in the direction of π total phase difference. Therefore, net energy transfer between two waves is attained. This coherent optical coupling is a very interesting phenomenon producing several exciting effects thus, leading to unique

applications in coherent image amplification, signal modulation and transmission.

1.4.3 Four wave mixing (4WM)

Phase conjugate generation has been demonstrated by mixing three waves in a nonlinear medium by utilizing the third order nonlinearity, $\chi^{(3)}$, of a material. The result of the interaction is the generation of a fourth optical wave which is the phase conjugate replica of a signal beam. In general, however, high power lasers must be used in order to obtain a considerable effect yielding a relatively high phase conjugate reflectivity. It has been demonstrated that the four wave mixing process can also be described in terms of real time holography[9], in which two waves record a hologram and a readout beam, phase conjugate to one of the recording beams, is used for the production of a phase conjugate replica of the other recording beam via diffraction. This operation can also be performed in photorefractive materials, in which the large second order optical nonlinearity, $\chi^{(2)}$, enables the use of low power CW lasers. An extremely high phase conjugate reflectivity, in some cases much larger than 100%[10] is achieved by utilizing a combination of 4WM along with two beam coupling processes[11]. In these latter cases, however, noise growth effects may limit the usefulness of such a process for certain applications.

1.4.4 Self-pumping

In the usual four wave mixing arrangement using a photorefractive crystal as a nonlinear medium, three different beams must be present. The interaction of two recording beams a "pump" and a "signal" as well as a readout beam produces an output PC replica of the signal beam. However in certain photorefractive materials exhibiting very large two beam coupling gain such as $BaTiO_3$ and SBN, four wave mixing may take place in the presence of only one input beam. The rest of the required beams can be "self-generated" internally within the crystal either by amplified noise and internal reflections on the polished sides of the crystal, or by utilizing linear or ring resonator cavities formed by external mirrors.

The first demonstration of a self-pumped phase conjugate mirror was performed by White *et al.*[12] in 1982 and consisted of a photorefractive crystal in an optical resonator cavity, in which the beams that were self generated from amplified noise, served to pump the conjugator.

A very useful self pumping arrangement (known as the "cat" phase conjugator) was also proposed by J. Feinberg[13] in 1982 and consists of a single suitably aligned photorefractive crystal alone. The pumping and readout beams were self-generated in the crystal by self-diffraction and coherent amplification of a single input beam, aided by total internal reflection at the facets of the crystal. This arrangement (shown

in Figure 1.6 c) can exhibit phase conjugate reflectivity as high as 76% Ross *et al*[14] including Fresnel losses.

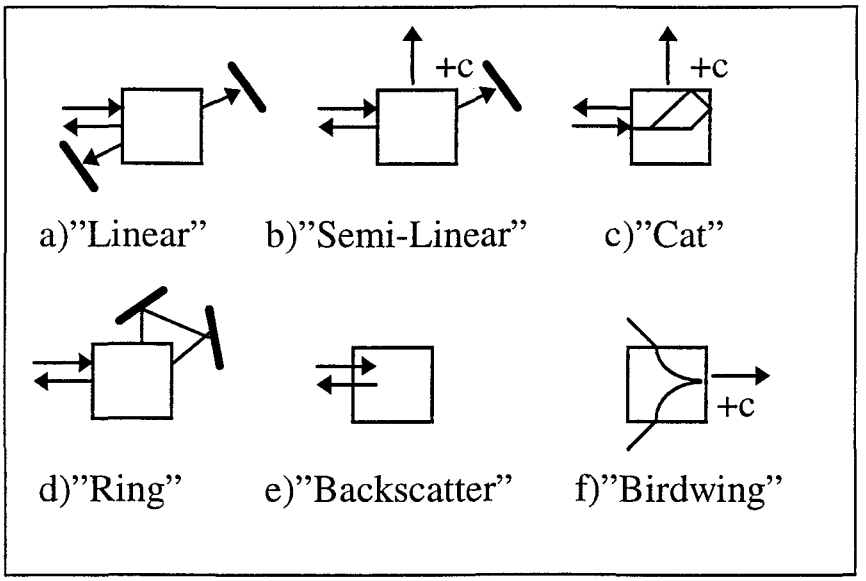

Figure 1.6. Various "self-pumping" arrangements using photorefractive crystals.

These first experiments have been followed by numerous works on novel resonator type schemes some of which are presented in Figure 1.6. In addition other interesting effects have been explored which are based on coupling between mutually incoherent beams[15]. In these schemes each participating beam utilizes gratings formed by another in a mutually consistent manner.

1.5 Photorefractive Materials

In the previous section the main properties of materials exhibiting photorefractive behavior were outlined. Materials of different classes can exhibit photorefractive behavior. They can be either semiconductors (GaAs, InP) or insulators (BSO, $BaTiO_3$ etc) and they

can be anisotropic. Their photorefractive performance can be modified by using appropriate doping or processing (annealing) techniques. Finally research on the development of new materials such as photorefractive polymers[16], is currently under way.

In this section details concerning photorefractive materials, used in the progress of this work, will be presented. In addition, other materials such as In_2O_3 and In_2O_3:Sn, although not considered as photorefractives in the strict sense, exhibit similar properties and are also included here.

1.5.1 Barium Titanate ($BaTiO_3$)

$BaTiO_3$ is a ferroelectric material[17] with perovskite structure. It is one of the first ferroelectrics discovered and recognized as photorefractive[18]. The crystal exhibits a sequence of phase transitions with decreasing temperature: cubic → tetragonal → orthorhombic → rhombohedral. At room temperature, $BaTiO_3$ is in its tetragonal phase, with point group symmetry 4mm and a Curie temperature of $T_c \approx 130°C$. In the as-grown crystals various orientations of the spontaneous polarization usually occur and the crystal is in a multidomain state. The useful optical, electrical and mechanical properties of the material are averaged out because they all depend on the direction and the sign of the crystal polarization. There are several techniques for crystal poling[19,20] which rely on a combination of application of electric field, heating and/or mechanical stress. The most extensively used poling

method is the direct application of relatively large electric fields (500-1000 V/cm) at the Curie temperature. This latter technique may be employed (with alternating fields) in the study of hysteresis loops in ferroelectrics. Good quality crystals of $BaTiO_3$ can be grown by the top-seeded solution growth (TSSG) technique[21]. Single crystal boules grown by this method are typically 2-3 cm in diameter, but only small (typically 0.5x0.5x0.5 cm^3) clear, free of visible defects, polished and poled samples can be produced from the grown boules.

The crystal is negative uniaxial with n_o=2.488 and n_e=2.424 at λ=514.5 nm. Electrooptic tensor component values for $BaTiO_3$ single crystals are presented in Table 1.1 . $BaTiO_3$ exhibits large phase conjugate reflectivity and coupling gain coefficient due to the large values of the electro-optic tensor components.

	r_{13} [pm/V]	r_{33} [pm/V]	r_{42} [pm/V]
Unclamped*	24 [22]	80 [22]	1640 [24]
	19.5 [23]	97 [23]	
Clamped	8 [25]	28 [25]	820 [26]

Table 1.1 Electrooptic coefficients for single $BaTiO_3$ crystal at room temperature. All measurements (except the one in Ref 23) were performed using flux grown samples.

Deep energy levels in the $BaTiO_3$ energy gap, considered to participate in the photorefractive effect, are attributed to vacancies and impurities.

* "Unclamped" refers to measurements that involves application of electric fields with frequencies much lower than characteristic piezoelectric resonant frequencies of the crystal. Under the influence of such fields the crystal vibrates freely and no constant strain is applied.

Oxygen vacancies introduce shallow levels (near the conduction band), Error! Reference source not found., and they are expected to be completely ionized at room temperature, while Ba vacancies are deep acceptors and they are expected to participate in the photorefractive process.

Various impurities have been detected in $BaTiO_3$ crystals, but only transition metal impurities have a significant contribution in the photorefractive process.

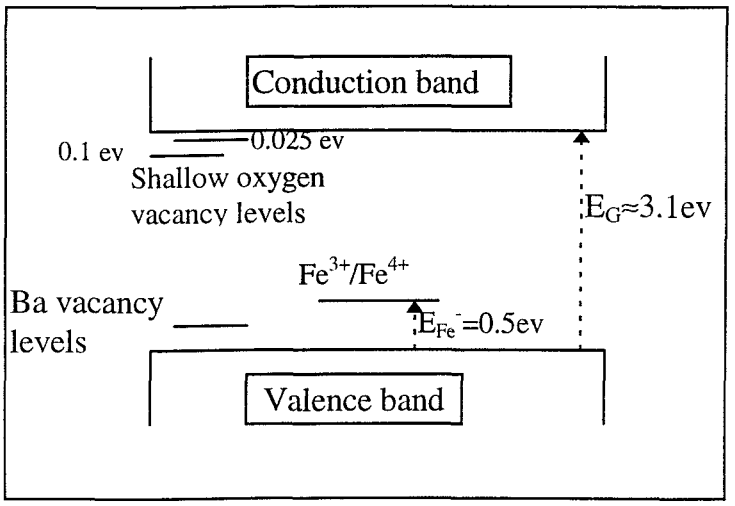

Figure 1.7 Energy levels of oxygen vacancies and Fe^{n+} ions in $BaTiO_3$ after Klein[17]. The energy gap is E_G=3.1eV.

Transition metals, like Cr, Co, Ni, Cu, are frequently present in $BaTiO_3$ crystalline samples in concentrations up to 50 ppm but Fe is the most commonly met impurity in larger concentrations. As in other photorefractive materials[27], Fe is expected to have the main contribution to the photorefractive process. The transition metals are

usually acceptor impurities and therefore the samples exhibit hole (p-type) dark conductivity and photoconductivity.

1.5.2 $Sr_xBa_{1-x}Nb_2O_6$

Strontium Barium Niobate $Sr_xBa_{1-x}Nb_2O_6$ (SBN) is a ferroelectric material[28].of the tungsten bronze structure with point group symmetry 4mm. The transition temperature can be controlled, by adjusting the Ba/Sr concentration ratio from $T_c \approx 60°C$ for Ba/Sr=1/3 to $T_c \approx 205°C$ for Ba/Sr=3, while Ce doping improves photorefractive characteristics.

	r_{13} [pm/V]	r_{33} [pm/V]	r_{51} [pm/V]
$Sr_{0.75}Ba_{0.25}Nb_2O_6$	67	1400	42
$Sr_{0.6}Ba_{0.4}Nb_2O_6$		420	42

Table 1.2 Electrooptic coefficients for $Sr_xBa_{1-x}Nb_2O_6$ at room temperature after R.. R Neurgaonkar *et al*[28]

SBN crystals present good photorefractive behavior due to their large r_{33} electrooptic coefficient (presented in Table 1.2) and large coupling gains have been reported. The poling procedure for SBN crystal is much more easier than for $BaTiO_3$ since electric fields ~2 KV/cm are required at room temperature and cracks are not likely to occur. This property has been also used in the fixing of holograms recorded by selective poling of illuminated areas. Crystals of good optical quality can be prepared using the Czochralski technique.

1.5.3 $Bi_{12}SiO_{20}$ (BSO)

Bismuth Silicon Oxide, $Bi_{12}SiO_{20}$ (BSO), together with Bismuth Germanium Oxide $Bi_{12}GeO_{20}$ (BGO), and Bismuth Titanium Oxide $Bi_{12}TiO_{20}$ (BTO), known as Sillenites, are paraelectric, electrooptic and photoconductive materials[29]. BSO is optically isotropic, having the 23 point group symmetry. It becomes birefringent under the application of an electric field due to the non-vanishing Pockels coefficient r_{41} (r_{41}=3.4 pm/V). Very large samples of high optical quality can be grown from the melt. BSO exhibits very large optical activity (ρ_0=45°/mm at λ=514.5 nm). This fact can improve very much the quality of image reconstruction in holographic experiments where a polarizer is used for optical noise suppression[30] since diffracted beams exhibit different polarization states with respect to the recording beams.

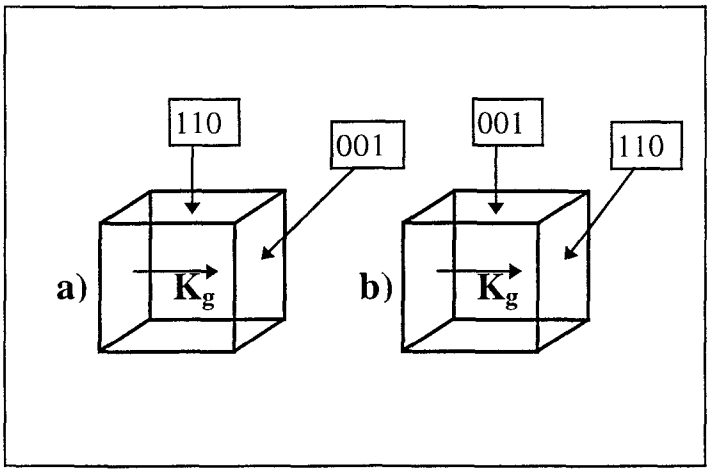

Figure 1.8 a) **Kg** ⊥ (001) plane: crystal orientation for maximum beam coupling, b) **Kg** ⊥ (110) plane: crystal orientation for maximum diffraction efficiency.

Optical activity is also responsible for the reduction of the diffraction efficiency of a recorded phase grating, as compared to the prediction of Kogelnik's classical theory for media without optical activity.

In experiments, two crystal orientations have been identified and are depicted in Figure 1.8 .

The orientation in which the grating wavevector (K_g) is normal to the (001) plane is specified for optimum energy transfer while $K_g \perp (110)$ leads to optimum diffraction efficiency.

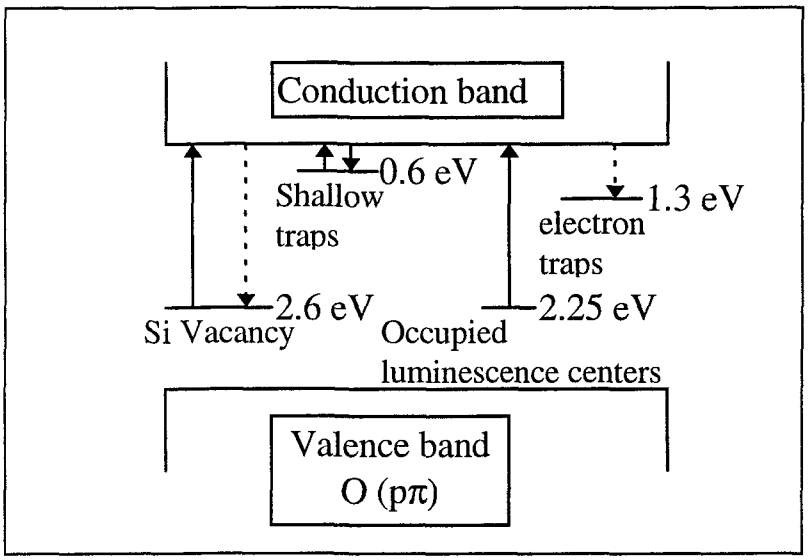

Figure 1.9 Energy level diagram of $Bi_{12}SiO_{20}$ at room temperature[11].

The energy gap in BSO is E_g=3.25 eV. The energy level diagram of BSO is depicted in Figure 1.9 . A broad energy level, centered 2.6 eV below the conduction band (when occupied by an electron), is attributed to a Si vacancy. A luminescence center located 1.3 eV below the conduction band (when occupied by an electron) and 2.25 eV when it is ionized, is

believed to participate in the charge transfer process. However depending on crystal nature other centers are also present resulting in bipolar photorefraction as is discussed in chapter 4.

Photoconductivity is n-type, explaining the fast response of the material, while dark conductivity is p-type. The photoconductivity is extremely large yielding high recording sensitivity, while the dark conductivity is sufficiently low to allow large storage times useful in some applications.

1.5.4 Indium oxide (InO_x) and indium tin oxide (InO_x:Sn).

In_2O_3 (InO_x) and InO_x:Sn are oxide materials with very interesting optical and electrical properties. Thin films of the above materials can be grown by various methods such as evaporation, sputtering, reactive ion plating, chemical vapor deposition, spray pyrolysis, etc. Because of their extended transparency and large conductivity, they are extensively used as transparent conductors in many applications such as conductive optical coatings in electro-optic devices including electro-optic modulators and liquid crystal displays (LCD's)[31].

InO_x films prepared by various methods are usually polycrystalline with a body centered cubic structure in the bulk material[32] and a lattice parameter of a=10.118Å. InO_x thin films exhibit mobilities in the range of about 10-75$cm^2V^{-1}sec^{-1}$, free electron densities of $n \approx 10^{19}$-$10^{20}cm^{-3}$ and typical conductivity $\sigma \geq 10^3(\Omega cm)^{-1}$. After a reducing heat

treatment higher values of conductivity are obtained. The index of refraction in the visible region ranges from n ≈ 1.9 to 2.08[33].

The conductivity and the lattice constant of the films increases with Sn doping. The values of the electron concentration in InO_x:Sn films is $n\sim10^{21}cm^{-3}$ and the measured mobility ranges from $15cm^2V^{-1}sec^{-1}$ to $40cm^2V^{-1}sec^{-1}$ leading to a conductivity in the range of $1.5x10^4$-$2x10^3(\Omega cm)^{-1}$.

The conductivity of polycrystalline InO_x and InO_x:Sn films grown by DC sputtering can be modified upon illumination with ultraviolet (UV) radiation (hv>3.5 eV), resulting in a variable electrical state of the films, from highly resistive to purely conductive[34]. Illumination of In_2O_3 (InO_x) and InO_x:Sn films with UV radiation also produces changes in the refractive index of the films enabling holographic recording[35] as it will presented in chapter 5. In the frame of this work thin films which are exhibiting similar properties are fabricated by pulsed laser deposition as outlined in the following section.

1.6 Materials development

1.6.1 Pulsed laser deposition (PLD)

Pulsed laser deposition (PLD)[36] has evolved as an important laser application in the deposition of thin film materials. In this application, a laser is used exclusively as a source of high energy density

monochromatic radiation. Radiation bandwidth is not as important here as compared to the importance of high photon flux necessary for ablation.

In a typical PLD arrangement the laser beam is focused on the surface of the target material causing ablation and forming a plume of plasma. The ablated material is deposited on the surface of the substrate, appropriately positioned facing the target.

A typical experimental setup for Pulsed Laser Deposition is shown in Figure 1.10 .

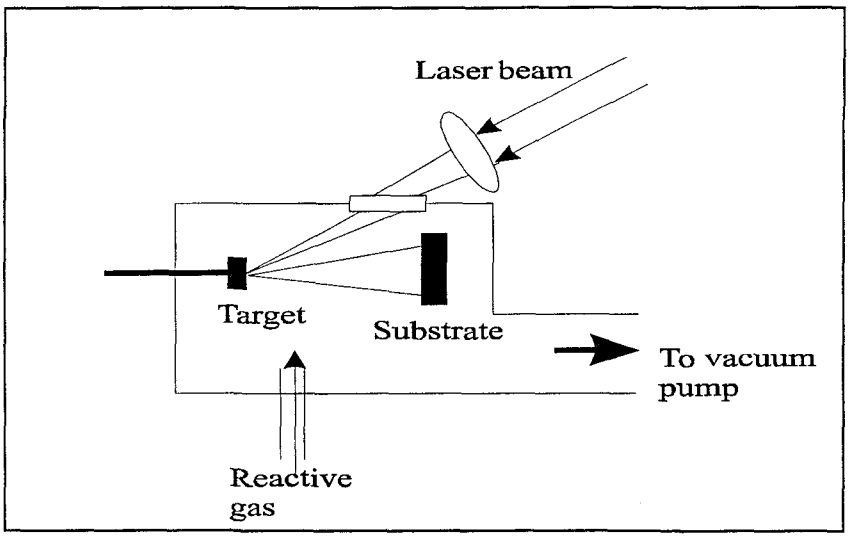

Figure 1.10 Schematic diagram of a PLD process.

The system consists of a vacuum chamber, incorporating ports for visible and invisible radiation, holders for the target and the substrate as well as valves for controlling possible reactive or inert gas input. Finally, a high power laser together with an optical system (mirrors

and lenses) providing laser beam control is used for ablating the target material.

In contrast to the simplicity of the PLD experimental arrangement the laser-target interaction is a very complex physical process. Although this work is not aiming at the understanding of the laser-target interaction phenomena, an outline of the mechanism will be given for clarity.

Theoretical descriptions are multidisciplinary and combine both equilibrium and non-equilibrium processes. The mechanism that leads to material ablation depends on laser characteristics, as well as the optical, geometrical, and thermodynamical properties of the target. The absorbed electromagnetic energy is converted into thermal, chemical, and mechanical energy causing excitation, evaporation, ablation, plasma formation, and exfoliation. "Evaporants" form a plume consisting of energetic species such as atoms, molecules, electrons, ions, clusters, micron-sized solid particles, and molten globules. The collisional mean free path in the dense plasma is very short and this leads to rapid expansion of the plume, immediately after laser illumination, into the vacuum. A nozzle jet with hydrodynamical flow characteristics is thus emanating from the target.

The first PLD experiment was realized in 1965 by Smith and Turner[37], but the scheme remained little known until the late 1980's when the

method was applied for the growth of high T_C superconductors[38,39]. Optical materials, like single crystalline ferroelectrics[40,41] or nonlinear electrooptic materials such as KTN[42] and BGO[43] single crystals and photosensitive glasses[44] can also be grown by PLD and that opens up a new area for applications in the field of optoelectronics.

Chapter 2

PULSED AMPLIFICATION OF CW SIGNAL FIELDS IN PHOTOREFRACTIVE $BaTiO_3$

2.1 Introduction

Amplification of continuous wave (CW) signal fields by two wave mixing (TWM) in photorefractive (PR) materials is now well established[6,45]. However highly nonlinear photorefractive materials such as $BaTiO_3$ exhibit slow response times and this prohibits their use where time varying CW signal fields are considered. On the other hand, pulsed holographic experiments in the visible spectral region performed in photorefractives, such as $BaTiO_3$ [46] and $Bi_{12}SiO_{20}$ [47], involve high intensity pulsed signal fields which may be inappropriate in some applications. These applications include holographic recording of living organisms where, for safety reasons, only very low intensity illumination is permitted. The development of a suitable method for the amplification of such weak signals is therefore essential and would extend the potential of holographic systems. Amplification of a CW signal field in a pulsed manner would, on the other hand, lead to a frame-by-frame holographic recording, as is appropriate for cineholographic applications.

In this chapter the study of pulsed amplification of low intensity CW signal fields[48] is presented. The operation is achieved by mixing two mutually coherent fields, a CW signal field, and a pulsed pump field in a photorefractive $BaTiO_3$ crystal.

The present work encompasses two quite distinct experimental tasks. First, the pulse amplification of a CW beam (λ=514.5nm) in a series of excimer-pumped dye-laser amplifiers is considered in order to obtain highly coherent intense nanosecond pulses. Second, two wave mixing in $BaTiO_3$ was performed, in which the pulse-amplified beam produced was used to pump the PR crystal, thus in turn coherently amplifying a weak CW beam.

2.2 Pulse amplification of a CW beam.

2.2.1 Development and characterization of a dye pulsed-CW laser amplifier

The development of a pulsed-CW laser amplifier is an integral part of this work. In Figure 2.1 a schematic layout of the experimental arrangement used is depicted. An argon ion laser operating in multi-longitudinal mode (~1.5 W) was used, together with three dye-laser amplifiers pumped by a XeCl excimer laser delivering ~200 mJ/pulse, 13 nsec (FWHM) pulses at 308 nm. The CW beam delivered by the ion laser was polarized perpendicular to the plane of the figure. The beam was elevated and 90° polarization rotated by the elevation stage, ES,

and was subsequently filtered and expanded by a spatial filter-telescope assembly, SF/TL. A variable beam-splitter, BS, was used to provide the CW signal, S, at a maximum power of ~30 mW. The rest of the argon ion laser beam (~500 mW) was directed through three dye laser amplifiers operating in series.

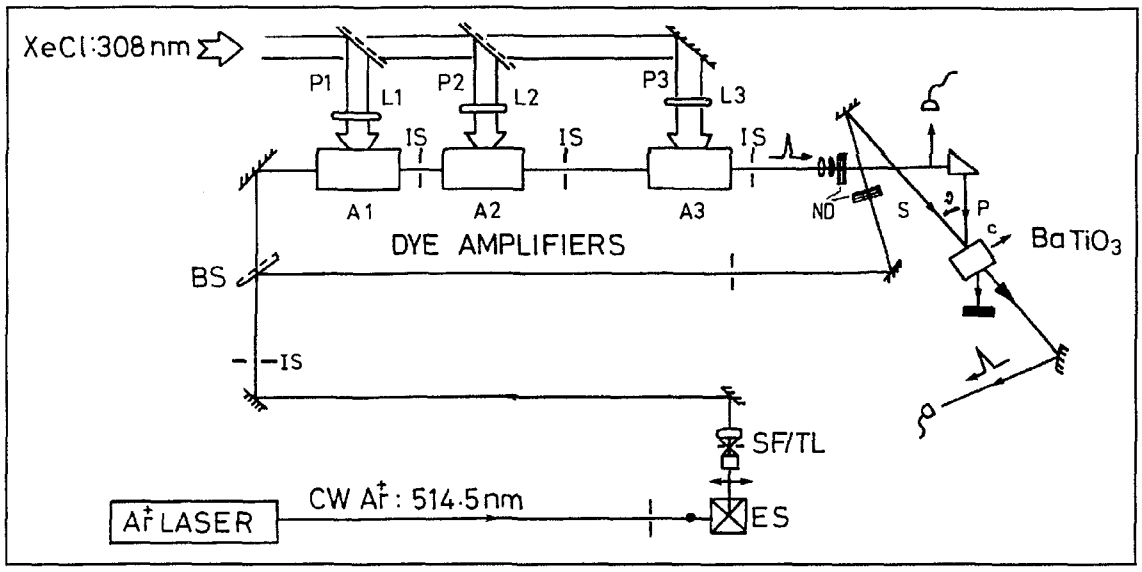

Figure 2.1 Schematic of the experimental configuration used for the pulsed amplification of a CW Ar^+ laser beam (514.5 nm). The system consists of three excimer-pumped dye laser amplifiers in series, enabling three step amplification of the CW beam.

The CW beam was focused by the SF/TL into the preamplifier A_1 and was left to diverge with ~2 mrad divergence through the dye laser amplifiers A_2 and A_3. The excimer laser was split as shown to provide pumps P_1, P_2, and P_3 at ratios 1.0:2.7:6.3. Beams P_1, P_2, and P_3 were line focused by cylindrical lenses L_1 (f=150 mm), L_2 (f=150 mm) and L_3 (f=250 mm), respectively.

In order to achieve maximum amplification and optimum performance, of the excimer-pumped amplification system, it was necessary to study the system's response as a function of various experimental parameters. Only one stage of the amplification setup (one dye amplifier) was used for that purpose as shown in Figure 2.2 .

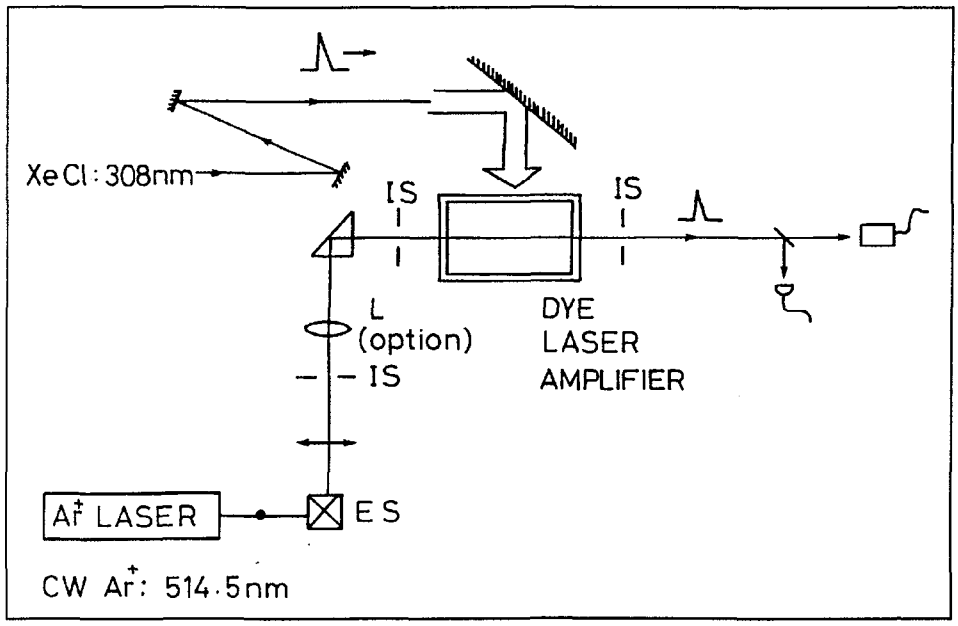

Figure 2.2 Experimental setup used for the optimization of dye laser amplifiers' performance

Measurements of the output pulse energy with respect to input CW-laser power, for various excimer laser pulse energy levels and dye concentrations, were taken. Typical results for various dye concentrations are depicted in Figure 2.3. Based on these results decisions regarding the optimum conditions for best performance can be made. It is interesting to note that it is not the highest excimer laser pump energy that produces the highest amplification and also that

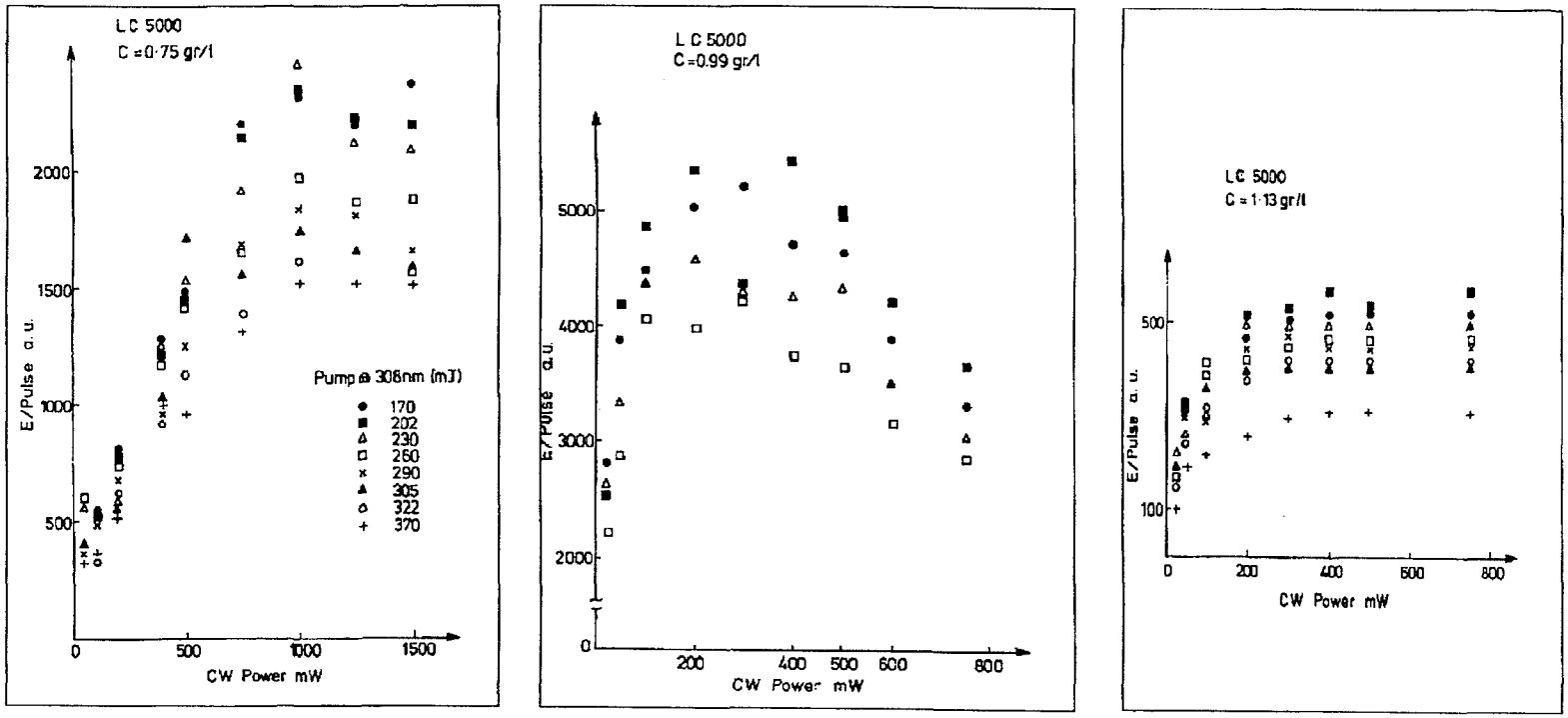

Figure 2.3 Typical plots of the pulse amplification of CW beam (preliminary studies) using a single dye-laser amplifier. Variation of output pulse energy as a function of input CW power, for different excimer laser pulse energy and dye concentration levels.

gain saturation of the medium occurs at relatively low input CW laser power.

The dye laser medium used was Coumarin 307 at concentrations of 1.14, 0.85 and 0.68 g/lt respectively for the amplifiers A_1, A_2 and A_3 at the final setup. Iris apertures IS, were used to reduce broadband amplified spontaneous emission (ASE) from the amplifiers. The optimized system was capable of modulating the CW laser beam at 514.5 nm and producing 12 mJ coherent pulses of ~13 nsec duration with ASE between 5% and 10%.

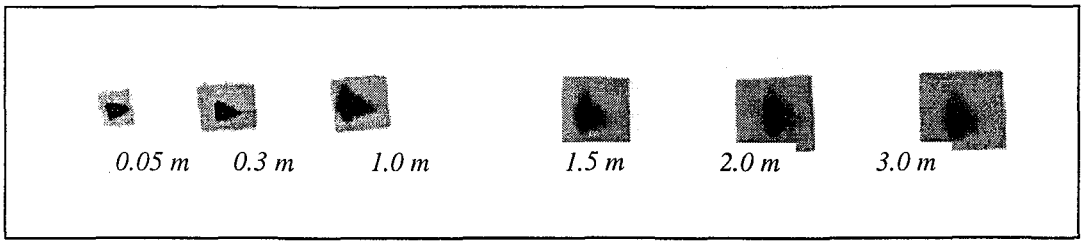

Figure 2.4 Traces of the pulsed amplified CW beam profile, on photographic paper, at various distances from the amplifiers' output.

The pulsed amplified beam, $\mathcal{P}$, produced was coherent with and had the same polarization (in the plane of the figure) with respect to the CW signal beam $\mathcal{S}$. Beams $\mathcal{P}$ (and also $\mathcal{S}$) were attenuated by using neutral density (ND) filters. Naturally the CW part of the beam $\mathcal{P}$ was greatly attenuated passing through the dye amplifier system, the optics and the ND filters used.

2.3 Coherent pulsed-amplification of weak CW signal fields by two beam coupling in $BaTiO_3$.

Beam $\mathcal{P}$ was used to pump a poled single domain $BaTiO_3$ crystal amplifier, with dimensions 5x4x6 mm^3. Signal beam $\mathcal{S}$ was incident almost perpendicular to the crystal surface that was parallel to the c-axis of the crystal with the pump beam $\mathcal{P}$ directed at an angle ϑ~40° with respect to the surface normal as depicted in Figure 2.5

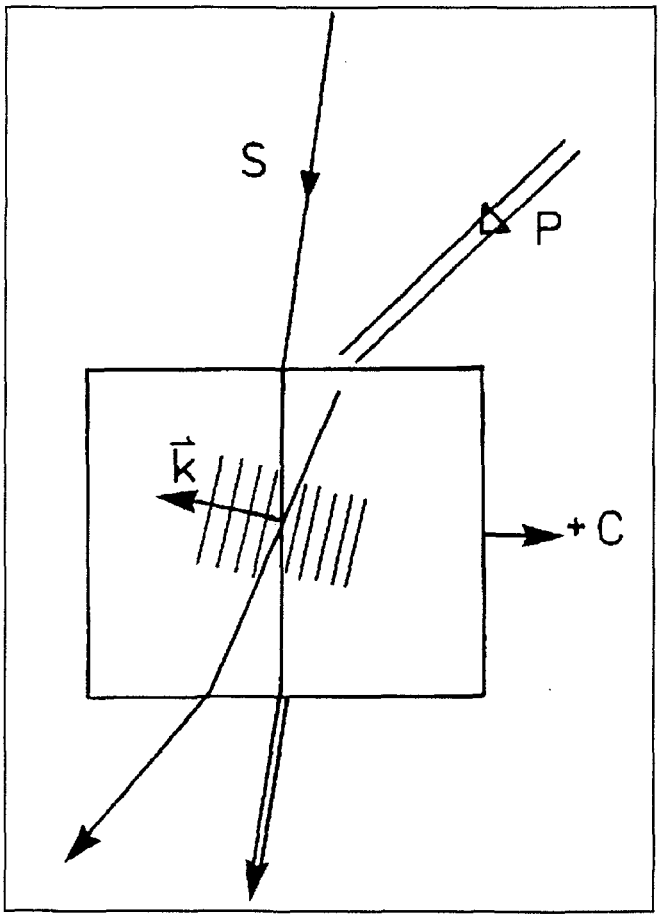

Figure 2.5 Two beam coupling in photorefractive $BaTiO_3$. The directions of +c-axis and grating wavevector **K** are shown.

Both beams were e-polarized with respect to the crystal orientation. The optical path lengths were matched for maximum mutual

coherence. The whole arrangement was intentionally setup on an ordinary laboratory table, having no vibration isolation, and the crystal was positioned on a rotational stage which could be motor- or hand-driven at relatively high speed. Under these conditions CW holographic recording between $\mathcal{S}$ and $\mathcal{P}$ could not be achieved with the crystal nominally stationary as interferometric stability could not be achieved.

Amplification of the CW signal beam was successfully performed in a pulsed fashion by the pulsed-amplified pump beam $\mathcal{P}$. The apparent sensitivity of the crystal was very high and amplification factors of several thousands were achieved in single pulse recording. The temporal behavior of the amplified output signal was detected by using calibrated p-i-n photodiodes and a Hewlett-Packard digital oscilloscope while the energy was monitored with a Gentec joule-meter. After each shot the crystal was irradiated by several pulses, with beam $\mathcal{S}$ turned off, to ensure erasure of the grating. Furthermore, recording was also performed by rotating the crystal continuously at relatively high speeds (~5 deg/sec) either manually or electrically with the same results. Beam fanning at maximum intensities used was erratic and could be eliminated by rotating the crystal at relatively low speeds ensuring the total absence of scattering off CW gratings.

2.4 Results and discussion.

Figure 2.6 depicts the typical temporal behavior of the pulsed-amplified CW signal output. The top trace is the simultaneously recorded pump beam $\mathcal{P}$. The important effect here is the appearance of peaks in the output pulse which may be attributed to competing fast and slow components contributing to pulse formation.

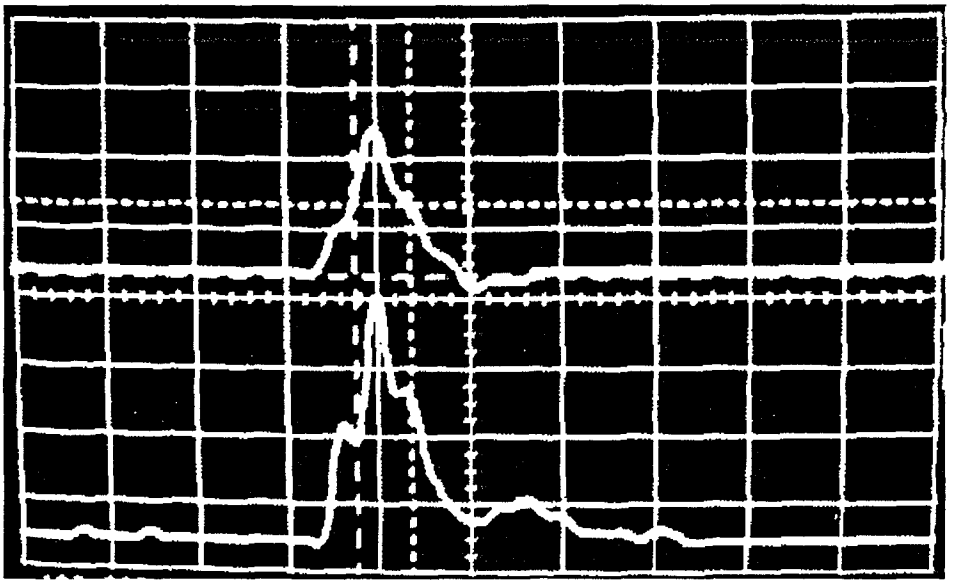

Figure 2.6 Simultaneously obtained oscilloscope traces of the pump pulse (top) and the two-wave-mixing amplified output pulse (bottom) obtained (time scale of 20 ns/div).

This effect is probably due to strong bipolar photorefraction[48,49] which becomes very pronounced under the present experimental conditions. Similar effects were observed in two beam coupling experiments in $BaTiO_3$ by using high intensity pulses[50]. In effect, electrons and holes are excited respectively from donor and acceptor levels present in the

crystal at different concentrations and generally exhibit different photoexitation cross sections. This variation in donor and acceptor concentrations leads to different saturation properties of the material and the value of the photoexitation cross section affects the carrier production rate.

The direction of coupling in photorefractive crystals is associated with the sign of carriers excited by the illuminating beams. Since both electrons and holes coexist in the crystal and have different mobilities, variations of the two beam coupling gain in a single pulse is likely to occur. We note here that similar bipolar effects in BSO are studied extensively in chapter 4.

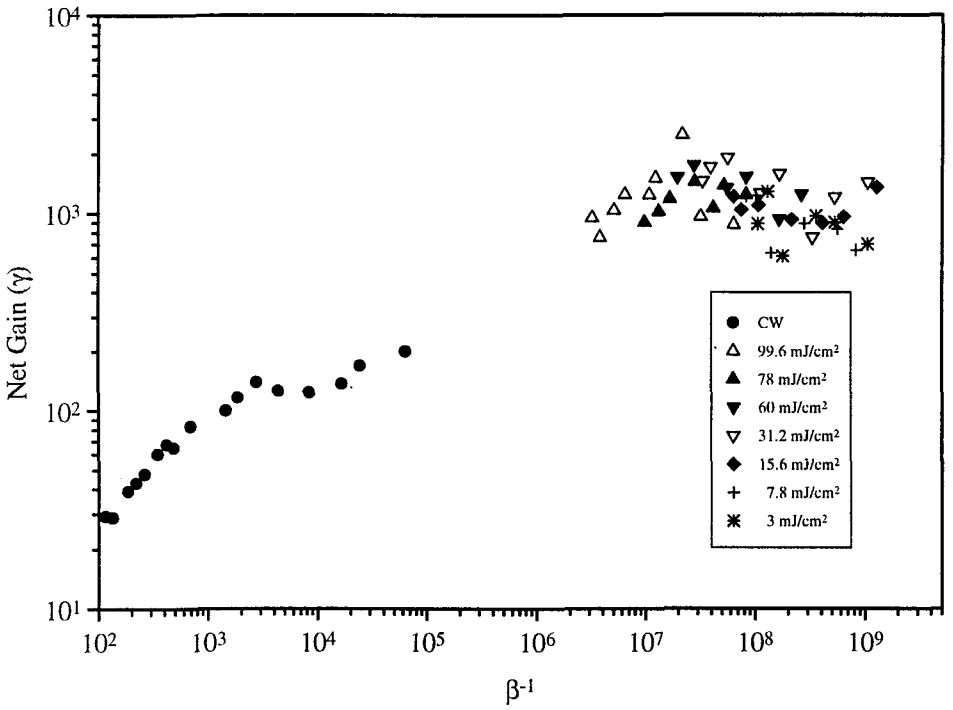

Figure 2.7 Net energy gain, γ, as a function of pump-to-signal energy ratio, β^{-1} for various pump energy densities. CW results (solid circles) obtained by the same crystal and experimental geometry are also shown for comparison.

Figure 2.7 depicts plots of the net photorefractive energy gain $\gamma(=\Delta S/S)$ as a function of the reciprocal signal-to-pump beam energy density ratio, β^{-1}.

The energy density of the signal beam, S, is the integral of the intensity over the pulse duration. The net energy exchange is ΔS. The saturated gain coefficient ($\Gamma=[1/d]\ln\gamma$; d is the interaction length) is about 15 cm^{-1} for all cases. Results of CW measurements using the same crystal and experimental geometry are also depicted for comparison. In that case β^{-1} refers to the corresponding beam intensity ratios. We note that the saturation of the CW gain (Γ~10 cm^{-1}) is observed for $\beta^{-1}>\sim10^4$ ratios. At higher levels noise dominates the amplified signal. The effective recording of signals lower than several tens of microwatts/cm^2 cannot be accomplished, even when using properly stabilized arrangements, probably because of the lack of the required longer term interferometric stability combined with a higher material sensitivity. In the present case recording and amplification at much higher pump to signal beam ratios, $\beta^{-1}\sim10^9$, with very low (subnanojoule/cm^2) effective signal energy densities can be performed. Here we underline that the material operates at saturation and near maximum amplification gain is obtained even for pump energy density $\mathcal{P}$~3mJ/cm^2, in which case the CW part of the pump beam is less than 1.5 mW/cm^2. It should also be noted that the response time of the crystal is intensity dependent and, provided that enough energy is supplied for

photoexitation, no problem exists for nanosecond recording. However, the total energy density in the crystal is determined by the pump beam and ranges from 3mJ/cm^2 to ~100 mJ/cm^2. We measured that 60% of this energy is absorbed in the crystal which implies a photo-generated carrier concentration of ~10^{16} cm^3 (assuming a 10% quantum efficiency).

In CW experiments high amplification usually requires high diffraction efficiencies (20% - 50%) of the PR grating[45]. In the present case, we can achieve high net gains at relatively low (<1%) diffraction efficiencies for single pulse operation, even though for CW amplification such recording may generally be considered inefficient.

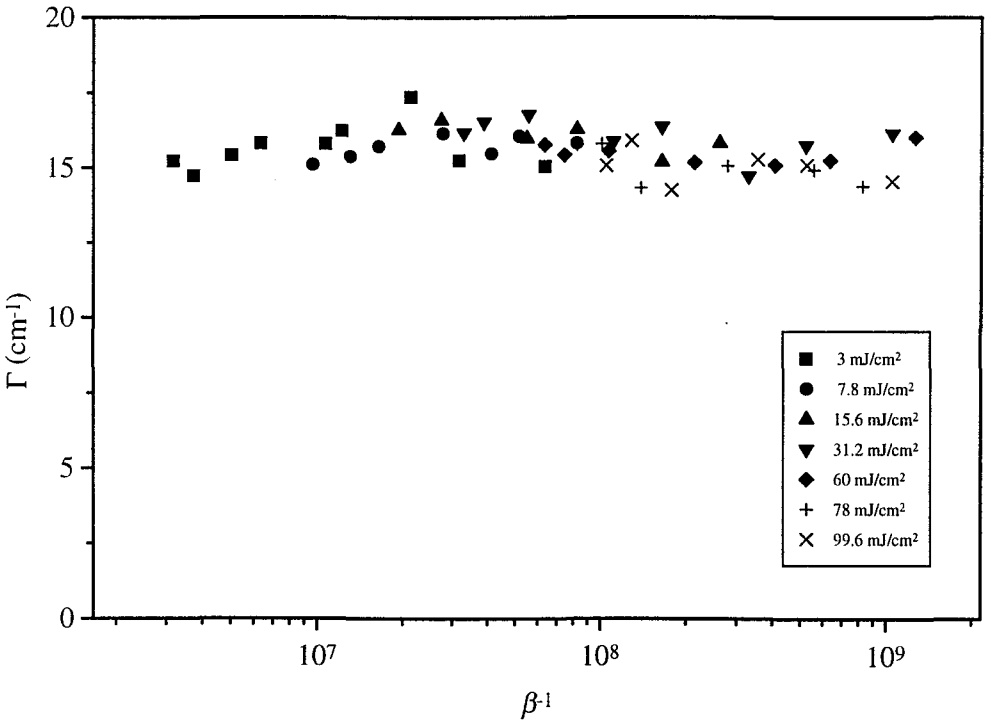

Figure 2.8 Gain coefficient Γ as a function of pump-to-signal beam intensity ratio β^{-1} for different pump energies.

The gain saturation of the amplifier is also verified from the linear diffraction efficiency plots and the errors involved are mainly due to the random fluctuation of the pumping pulse energy. The observed gain coefficient Γ is depicted in Figure 2.8 and the corresponding diffraction efficiency is depicted in Figure 2.9 at different pump levels as a function of pump-to-signal intensity ratio. The energy density of the signal beam is the integral of the intensity over the pulse duration because this is the CW energy participating in the process.

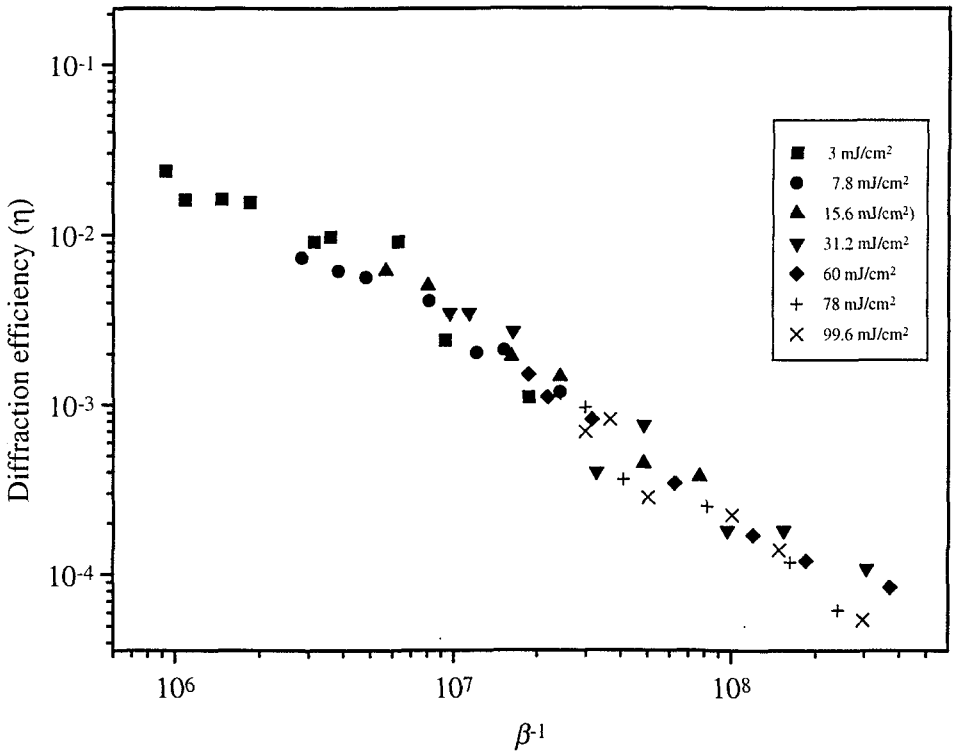

Figure 2.9 Diffraction efficiency η, as a function of pump-to-signal beam intensity ratio β^{-1} for different pump energies.

The gain saturation of the $BaTiO_3$ amplifier is verified here by the linear diffraction efficiency plots. The errors involved are mainly to the fluctuation of the pump energy, reflecting the fluctuation of the

excimer laser energy. These results prove that high gain can be achieved although the diffraction efficiency is low.

To increase the output energy from the photorefractive system a second barium titanate crystal was used in series. Unfortunately, at the intensity levels used, this crystal exhibited permanent recording behavior[51] and therefore it was considered inappropriate for the present operation. The nature of the material is certainly a significant parameter here and our original crystal also exhibited some deterioration of its gain after long periods of exposure to high intensities, although its main recording behavior was preserved.

In the specific case of repetitive recording with the crystal stationary, the superposition of gratings naturally yields an erratic recording behavior which is caused by the alteration of interference conditions from shot-to-shot. The large dynamic range of the material is verified, however, by the observed large random increases of gain. In further experiments, the temporal behavior due to the superposition of gratings was investigated. In Figure 2.10 the erratic output from a series of sequentially superimposed holograms with no alteration of the recording conditions is depicted.

As we have previously mentioned, no permanent noise component was observed. Therefore, the development of noise gratings scattering along the signal beam direction may be considered minimal at the time

a)

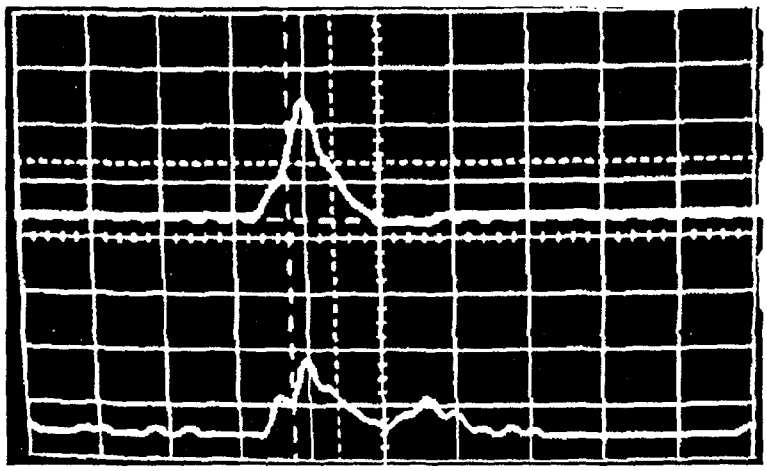

b)

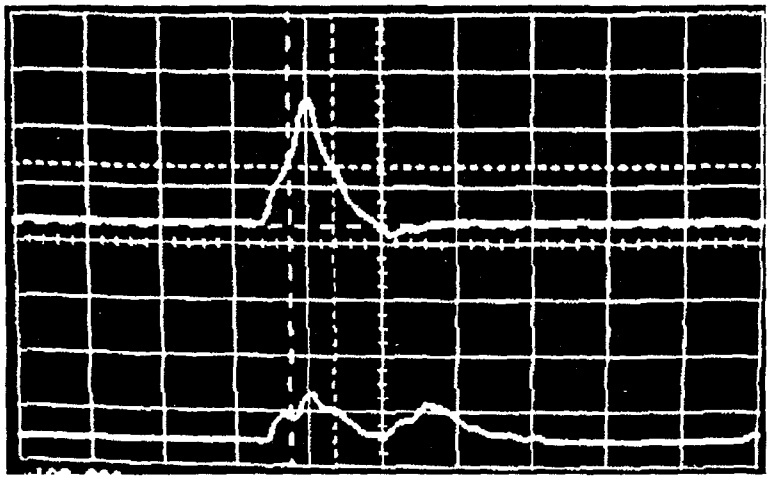

c)

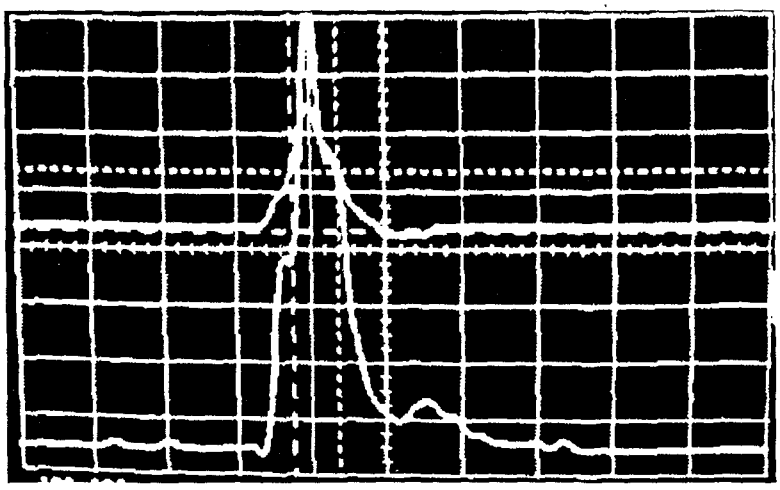

d)

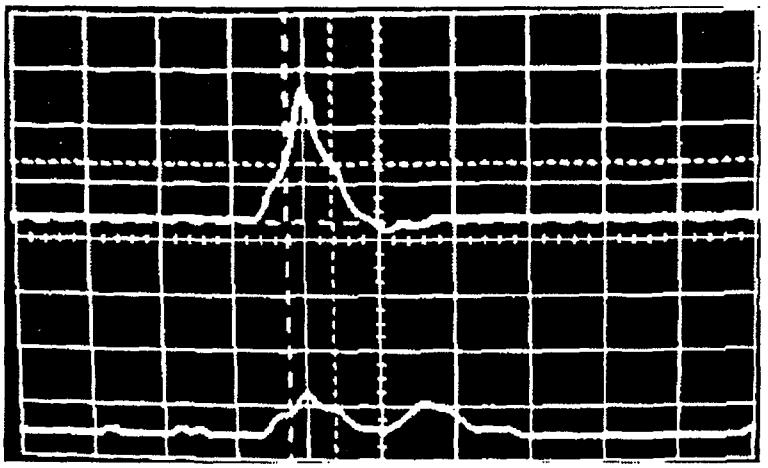

e)

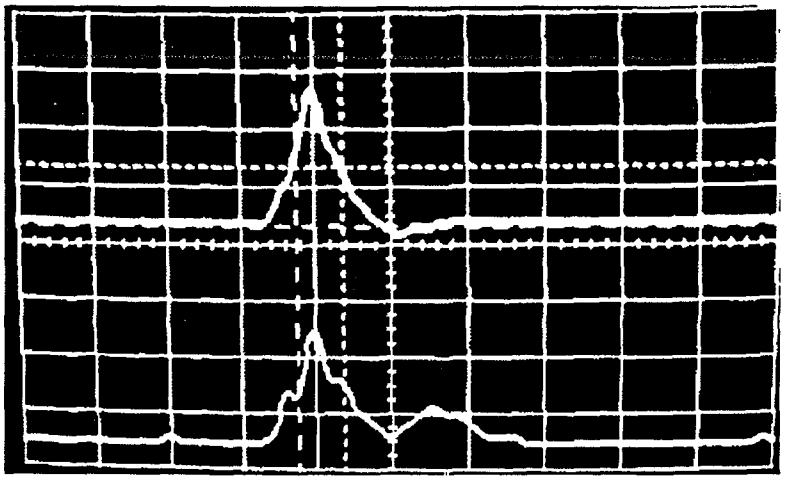

f)

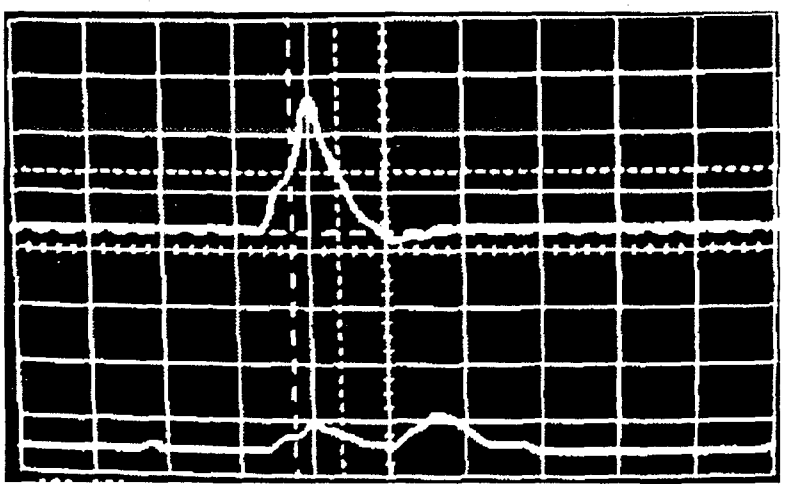

Figure 2.10 (a)-(f) Sequence of output traces observed by superimposing photorefractive gratings.

scales involved. The high recording sensitivity achieved in the present experiments can be explained in terms of the several novel features of the scheme. First, the system is not affected by object motion or vibrations. Interferometric stability of $\lambda/8$ for example may be satisfied for speed of <~3 m/sec which is a particularly large figure.

Second, in our present arrangement the crystal is continuously illuminated and therefore, in contrast to purely pulsed experiments where excitation from a purely relaxed population is used, a uniform dynamic excitation and trapping is already taking place in a fashion similar to a CW experiment, prior to the arrival of the pumping pulse. In this case intermediate trapping sites[52], which may easily become ionized by the incoming pulse, will certainly play an important role. The combination of these facts could be responsible for the great increase in the sensitivity of the crystal over the CW case. This scheme utilizes the insensitivity with respect to stability which is an exclusive characteristic of pulsed recording together with a higher recording sensitivity which appears to be an exclusive characteristic of CW recording. Furthermore, the sensitivity observed here may not be the actual sensitivity of the material itself since the incident pulse produces a large pyroelectric field[53] along the direction of the c-axis which may be responsible for producing, transiently, higher diffraction efficiencies.

2.5 Conclusions.

The feasibility of a novel scheme of pulsed coherent amplification of low intensity CW signal beams in photorefractive materials has been successfully investigated. The present system utilizes a CW laser beam that has been pulsed amplified by dye-laser amplifiers to perform high sensitivity real-time holographic recording in photorefractive barium titanate and produce net gains of almost 10^4. The capability of the system to perform high-gain coherent amplification at simultaneously extremely low effective signal energy and very low signal-to-pump energy ratios appears to benefit from the most advantageous properties of both high sensitivity CW techniques and high stability pulsed techniques. The method certainly appears to be very promising in the pulsed recording and projection of moving objects and the prospective development of cineholographic systems.

Chapter 3

PHOTOREFRACTIVE ADAPTIVE TRANSMISSION SYSTEM

3.1 Introduction

Systems based on the combination of photorefractive (PR) crystals[54] have proved advantageous in a range of real-time optical processing applications such as amplified phase conjugate (PC) generation[55], optimal filtering[56], resonators and memories[57,58,59], and high fidelity PC imaging[60].

In the context of optical signal modulation, the electrooptic property of the photorefractive bulk crystal has been utilized for temporally modulating the generated PC fields, via the external application of electric signal fields to the crystal[61]. Two wave mixing using beams that are temporally modulated at frequency higher than the reciprocal photorefractive response results in temporally modulated output beam intensity. Such effects have been exploited in adaptive interferometry[62,63,64] as well as in differential signal amplification and detection schemes[65,66,67]. Temporally modulated interacting beams may also produce time-varying photorefractive gratings and these

effects have been successfully employed in optical lock-in detection and frequency conversion applications[68,69].

In contrast to previous single PR element systems which have been concerned with temporal signal modulation, multi-element systems may exhibit several distinct features that are exploited in this work. Where amplification and phase-conjugation are performed in two separate stages, controlled amplification can be applied to the input signal, thus, enhancing the system's potential for operation at very low input signal fields. The additional degrees of freedom provided, result in a system exhibiting an overall net PC reflectivity exceeding unity at extremely low input intensities, although utilizing a low reflectivity PC element, which is advantageous in signal transmission applications. The use of self-pumped phase conjugators[13] may however, in this case prove beneficial in suppressing noise via the inherent thresholding processes involved. In addition, high-frequency amplitude and/or phase modulation can be performed all-optically by utilizing the inertia of the PR gratings to exchange information between beams while maintaining the overall *real-time tracking* character of the phase conjugation process.

In this chapter, a two-element Photorefractive Adaptive Transmitter System[70] (PATS) relying on the combined operation of a strontium barium niobate (SBN) input amplifier and a barium titanate ($BaTiO_3$) self-pumped phase conjugator, is presented and analyzed. The system

is simultaneously capable of: (i) amplifying a low intensity probe signal input, (ii) modulating it all-optically and (iii) re-transmitting it back to its source in a real-time amplified phase conjugate manner. Preliminary experimental results and theoretical considerations supporting the operation are presented.

3.2 Characterization of PR crystals

Prior to the realization of the amplifier-conjugator system, preliminary studies of the crystal behavior were carried out in order to achieve the conditions for best performance of the combined system. Such procedure is necessary as this behavior is a function of the specific crystal properties as outlined in chapter 1.

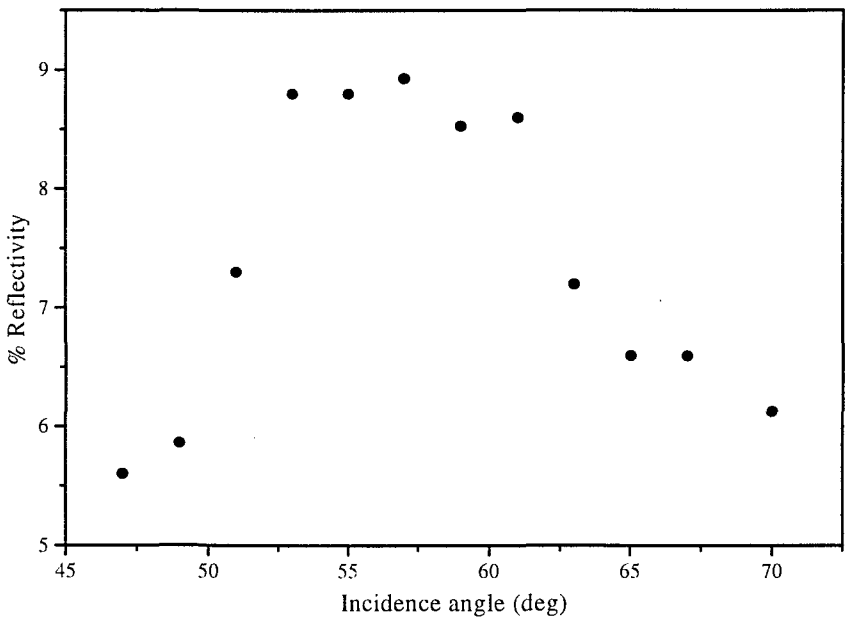

Figure 3.1 Phase conjugate reflectivity of the $BaTiO_3$ crystal (in self pumping configuration) for various incidence angles (with respect to the crystal facet normal).

In Figure 3.1 the phase conjugate reflectivity from a self pumped $BaTiO_3$ phase conjugator is plotted against the angle of incidence of the pump beam, in order to determine the angle for maximum reflectivity. We observe here that for an arbitrary input beam intensity this configuration yields a bell-shaped angular response.

Figure 3.2 depicts the variation of PC reflectivity of $BaTiO_3$ with input intensity for an angle of 65° with respect to the crystal entrance facet normal. No self-pumping occurs for intensities less than $62mW/cm^2$ (thresholding), while for large intensities saturation of the reflectivity is observed.

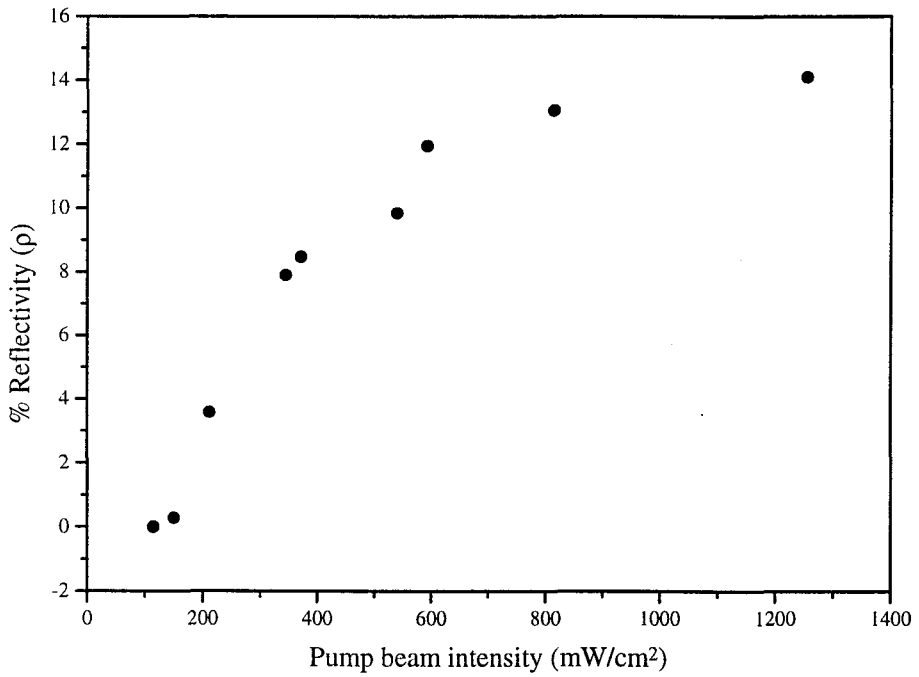

Figure 3.2 Study of phase conjugate reflectivity as a function of input (pump) intensity.

Two beam coupling experiments with the SBN amplifier, were performed in order to find the fringe spacing for optimum

amplification. From the results plotted in Figure 3.3 we observe that a maximum gain of γ=7 is observed for about 65° to 70°. At this angle the gain constant corresponding to a pump-to-signal intensity ratio of β^{-1}=62 is found to be Γ=6.5cm^{-1}.

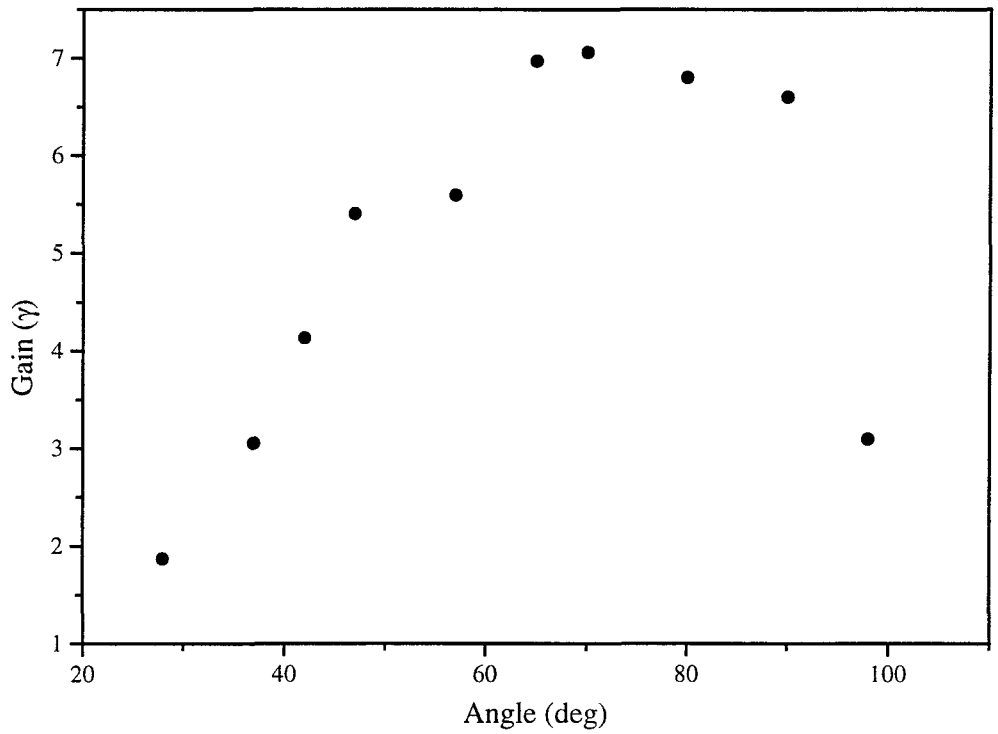

Figure 3.3 Two beam coupling net gain γ as a function of the angle between recording beams. The pump-to-signal beam intensity ratio is β^{-1}=62.

The high net gain points are enclosing a field of over 40°, yielding no severe limits for the operation of the combined system described in the next section.

3.3 Amplified PC field generation

3.3.1 Experimental considerations

Figure 3.4 depicts the experimental arrangement used. A poled single-domain $BaTiO_3$ crystal, PCM, with dimensions 5mmx6mmx6mm and a poled SBN:Ce crystal, AMP, with dimensions 10mmx9mmx3mm were used. A He-Cd laser operating in multilongitudinal mode at 442nm was also used. The unexpanded laser beam is divided by variable dielectric beam splitters (not shown) to provide a weak probe signal beam, $\mathcal{S}$, and a pump beam, $\mathcal{P}$, with maximum intensities of 35.4mW/cm^2 and 1.7W/cm^2 respectively. Power measurements were performed with a Newport 835 digital picowatt-meter. Beams $\mathcal{S}$ and $\mathcal{P}$ are incident on the AMP crystal at an angle $\vartheta \approx 70°$ in which AMP operates at near maximum beam coupling gain. Both beams are e-polarized with respect to the AMP c-axis. After the amplification stage the amplified beam $\mathcal{S}_a$ passes through a lens L (f=50mm, f/1.5) and is incident on the self-pumped phase conjugate mirror (PCM) crystal at an angle $\vartheta \approx 60°$ to the input surface normal. $\mathcal{S}_a$ is e-polarized with respect to the PCM c-axis. The crystal operates above threshold only with the use of an amplified beam $\mathcal{S}_a$ having intensity over 62mW/cm^2, and it exhibits a maximum PC reflectivity ρ=14%. The self pumped PCM produces the PC field $\mathcal{S}_{pc}$, which after back-transmission through the system, is aberration compensated, and propagates back to the source. A beam splitter BS with reflection-to-transmission

intensity ratio r:t=50:50 is used to obtain the output. The present system is capable of operating with an overall net reflectivity exceeding unity. However, as it is discussed below, this is achieved under certain conditions depending on the input signal-to-pump intensity ratio as well as the AMP gain and PCM reflectivity. This limitation is caused by the fact that the back-propagating PC field couples back to the pump beam via the gratings already formed in the AMP crystal. The input intensity dependent nonlinearity of the PCM also reinforces such limitations.

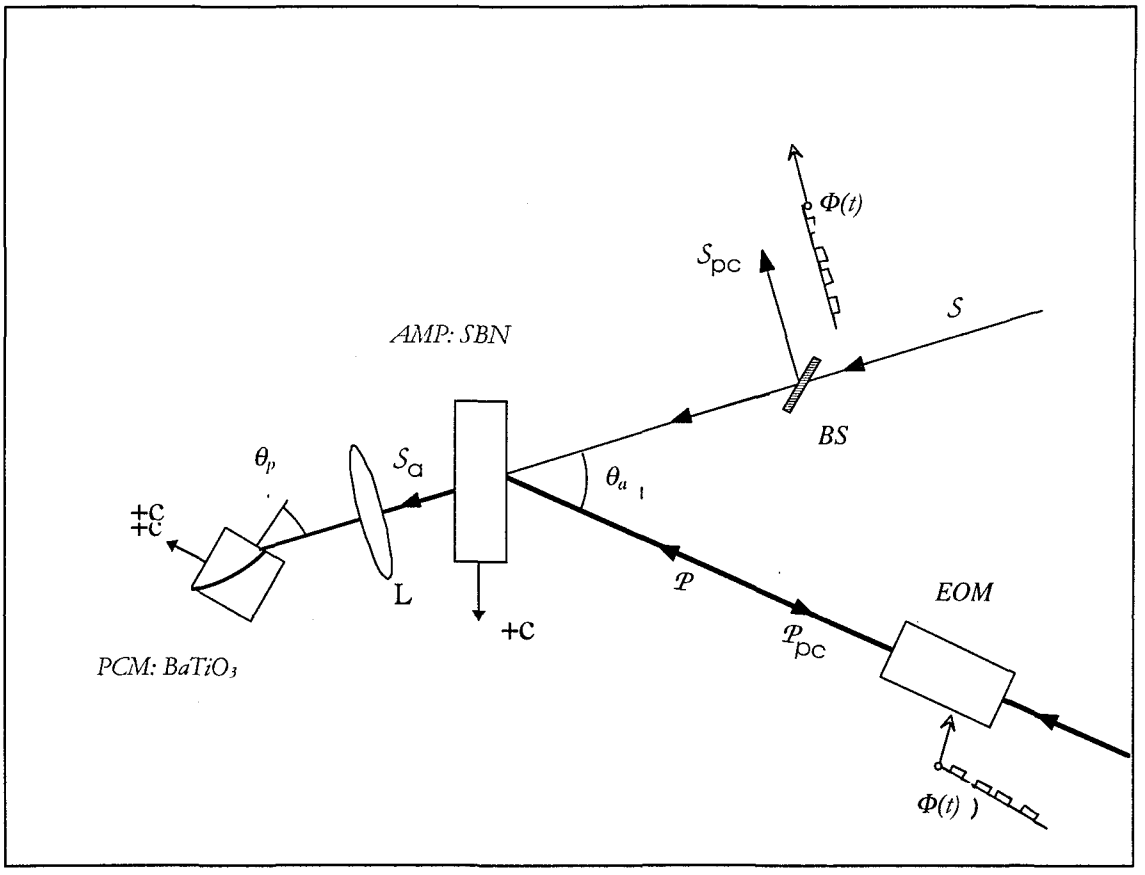

Figure 3.4 Schematic of the experimental arrangement used to demonstrate all-optical modulation and amplified PC transmission.

Four-wave-mixing in the AMP is performed in all cases and produces the PC field, $\mathcal{P}_{pc}$, of beam $\mathcal{P}$. However, secondary relatively weak grating recording between S_{pc} and $\mathcal{P}_{pc}$ is in phase with the primary grating written by S and $\mathcal{P}$ and thus we only anticipate a small modification in the index modulation. This indeed is the simplest case encountered as additional wave-mixing processes which enhance the losses may occur. Experimentally this is avoided here by adjusting the optical path length between the crystals to exceed the coherence length of the laser used (about 10 cm in our experiments).

The response time of the amplifier and conjugator crystals at the intensity levels used is about 1 second and 3 seconds respectively. This response time compatibility acts to smooth out any input spatial phase instabilities in the AMP output and results in stabilization of self-pumping and consequently in the successful operation of the system.

3.3.2 Theoretical Analysis and Results

Considering that the PCM crystal operates well above threshold with a saturated reflectivity ρ, and that the net gain and diffraction efficiency of the AMP crystal are γ and η respectively, the overall net reflectivity, R, of the system at an input signal-to-pump beam intensity ratio, β, may be given by :

$$R = \frac{|S_{pc}|^2}{|S|^2} = rt\gamma\rho(1-\eta) \tag{3.1}$$

where t, r are the intensity transmission and reflection coefficients of BS respectively.

In order to achieve $R \geq 1$, for a constant PCM reflectivity η, we require:

$$\beta rt\gamma^2 - rt\gamma + 1 \leq 0 \tag{3.2}$$

provided $\gamma=\eta/\beta$ for small signals. Equality in the above expression holds for R=1.

The inequality (3.2) implies however simultaneous satisfaction of the following conditions:

$$\beta < \frac{rt\rho}{4}$$

and (3.3)

$$\frac{[q-(q^2-4\beta q)]^{\frac{1}{2}}}{2\beta q} < \gamma < \frac{[q+(q^2-4\beta q)]^{\frac{1}{2}}}{2\beta q}$$

where q=rtρ. Therefore, in order to obtain amplified PC generation for a given ρ and a low enough value of β, the AMP gain Γ must be tuned (for example by Bragg or c-axis angular adjustment) within the limits described by (3.3). Equivalently, an operational region regarding the useful diffraction efficiency range may be found. Under the stated assumptions, it is clear from the above equation (3.1) that r=t=0.5

maximizes R and this is in line with the experimentally observed behavior.

Figure 3.5 depicts experimental results of the net overall reflectivity performance of the system as a function of beam intensity ratio, β^{-1}. We observe that the net reflectivity R approaches 400% for β^{-1} ~10^5. This result agrees quite well with the limits set by relations (3.3) above and the gain value γ=2x10^3 is within the theoretically specified range of $57<\gamma<5x10^5$.

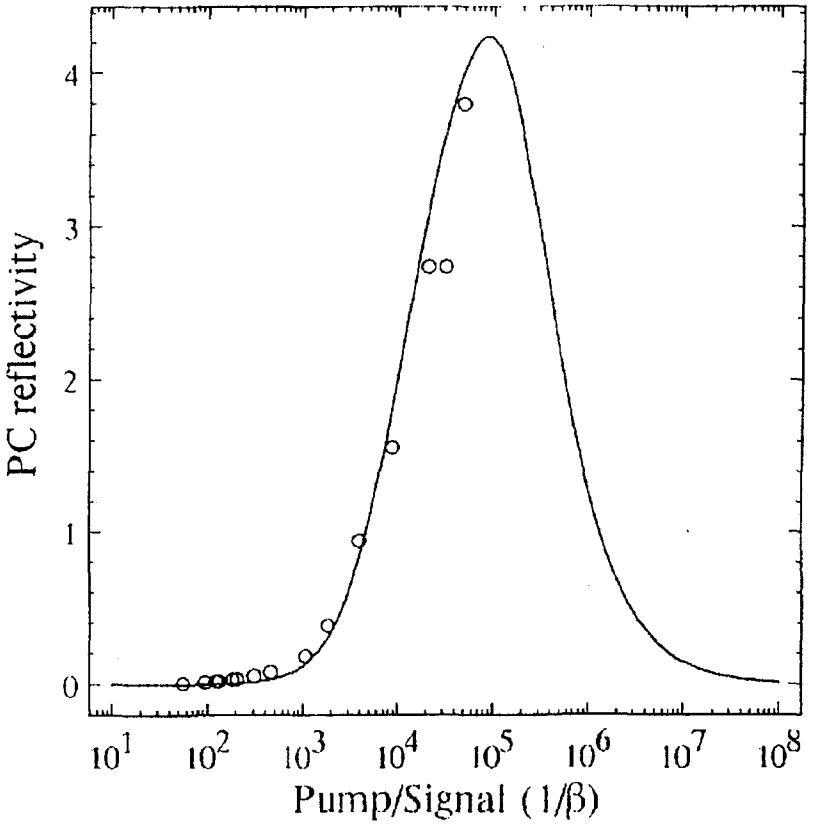

Figure 3.5 Phase conjugate net reflectivity of the system, R, as a function of pump-to-signal beam intensity ratio, β^{-1}. Pump intensity is 1.7W/cm^2. Experimental points and theoretical line plot are depicted.

We note however, that a lower limit in β exists owing to signal-to-noise-ratio considerations and the thresholding characteristics of the PCM. Operation near the large upper limit of β^{-1} predicted, certainly implies severe noise growth. We also state that a constant saturated PCM reflectivity assumed above only represents a useful special case in which, for example, the image contrast is preserved. The inclusion of the PCM nonlinearity requires a more detailed theoretical account. By incorporating in equation (3.1) analytical expressions[54] for γ and η and an experimentally determined exponential behavior for the PCM we have obtained a quite complicated dependence of R on β^{-1}. This, predicts very well the observed behavior although a slightly higher value (~10%) for the experimentally determined gain constant is required to provide full agreement with the experimental results as plotted in Figure 3.5. From these theoretical considerations it is apparent that for a specific pump beam intensity a maximum in reflectivity exists. This is the natural consequence of competition between the processes outlined previously. The model includes the decrease of PCM reflectivity with input but not the thresholding which would produce a reflectivity cut-off. Experimentally only the left-hand-side, low β^{-1}, wing of the theoretical plot has been accessed, while the usefulness of the upper β^{-1} region appears to be limited.

Figure 3.6 depicts an example of a pictorial result obtained by the system operating with high gain at about 50μW/cm^2 input signal

intensity. The fidelity of the conjugation process under the present experimental conditions, and in particular under these low input signal beam intensities, remains at acceptable levels.

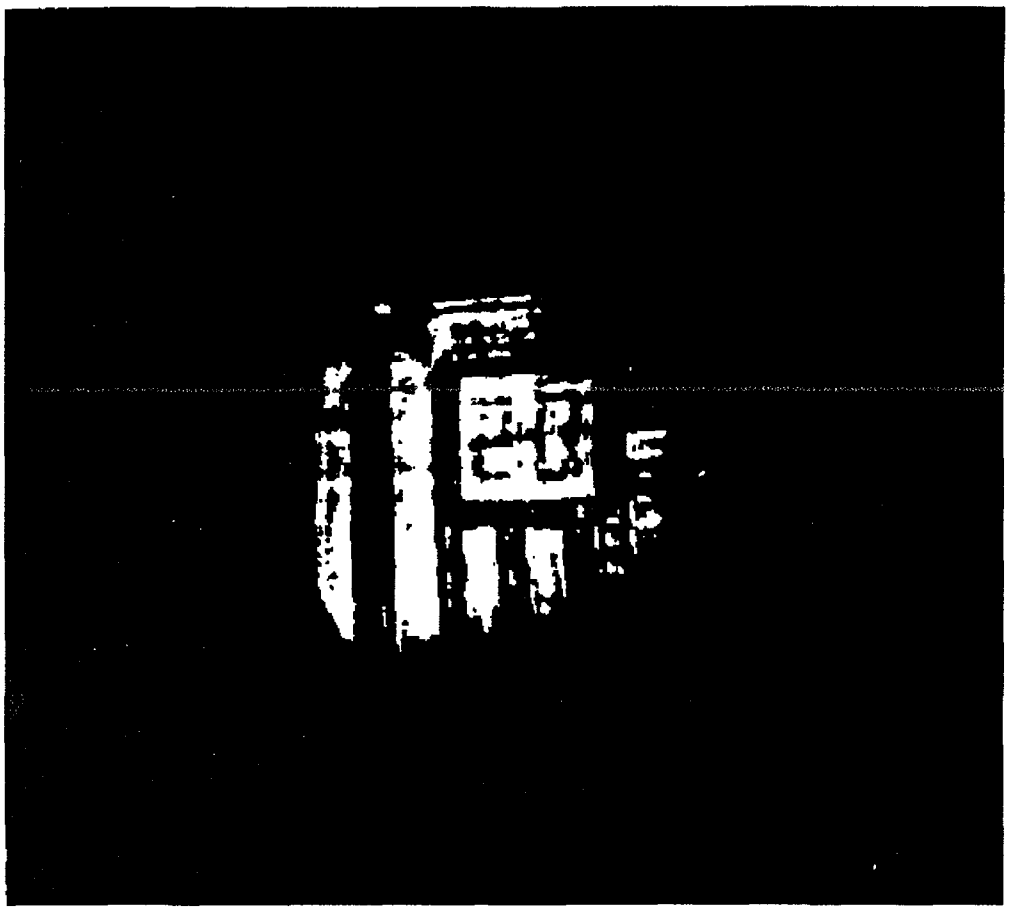

Figure 3.6 PC image of a test-chart object obtained by the system at low input intensity and high PC reflectivity (20 refers to 20 μm line-width).

Nevertheless, in these experiments not all the available space-bandwidth-product of the system has been exploited since the SBN crystal used had growth striations, which limited the operation to within a rather small useful interaction volume. We would like to note again that an important operational feature of the system is that noise

generated in the amplifier is filtered out in the output PC. This is attributed to the thresholding mechanism of the self-pumped PCM[68].

3.4 Optical signal modulation

3.4.1 Operation Analysis

The system presented so far has also been used for the simultaneous temporal phase-modulation and amplified dynamic phase-conjugate transmission of low intensity probe signal beams. A slightly modified experimental arrangement includes a lithium niobate electrooptic phase modulator, EOM, as shown in Figure 3.4 , as well as piezoelectrically driven mirrors (PZM) not shown. Beam $\mathcal{P}$ is modulated by the EOM at frequencies from 1kHz to 10kHz. The input and output of the system is detected interferometrically at several positions. The low frequency operation up to 1kHz has also been investigated by using PZMs.

The two fields input in the system, a low intensity unmodulated probe signal, $\mathcal{S}$, and a high intensity phase-modulated pump, $\mathcal{P}$, ($|\mathcal{S}|<<|\mathcal{P}|$), with respective wavevectors k_s and k_p, are given in the simplest case of sinusoidal phase-modulation of $\mathcal{P}$ by:

$$\mathcal{S} = Se^{[i(\omega t - k_s r)]}, \quad \mathcal{P} = Pe^{\{i[\omega t + \Phi(t) - k_p r]\}} \tag{3.4}$$

where ω is the carrier optical frequency of the laser beam used, and $\Phi(t) = \delta[1+\sin(\omega_m t)]$ is the phase modulation at frequency ω_m imposed

experimentally with a phase modulation depth, δ. We note that generally S and P may include spatial wavefront phase dependence while here for simplicity we treat them as magnitudes. For simplicity, we ignore the beam-splitter factors r and t (reflection and transmission coefficients).

Holographic recording in the AMP crystal is produced by an intensity interference pattern of wavevector $K=k_s-k_p$ which may be expressed by :

$$\begin{aligned} I &= (\mathcal{S}+\mathcal{P})(\mathcal{S}+\mathcal{P})^* = S^2+P^2+2SP\cos\{\mathbf{k}\cdot\mathbf{r}+\delta[1+\sin(\omega_m t)]\} \\ &= S^2+P^2+2SP\{\cos(\mathbf{K}\cdot\mathbf{r}+\delta)\cos[\delta\sin(\omega_m t)] \\ &\quad -\sin(\mathbf{k}\cdot\mathbf{r}+\delta)\sin[\delta\sin(\omega_m t)]\} \end{aligned} \tag{3.5}$$

which by using Fourier expansions may be written as:

$$I_0[1+m_a(t)\cos(\mathbf{K}\cdot\mathbf{r}+\delta)-m_b(t)\sin(\mathbf{K}\cdot\mathbf{r}+\delta)] \tag{3.6}$$

where $I_0=S^2+P^2$ is the total intensity and

$$\begin{aligned} m_a(t) &= 2(\frac{S}{P})[J_0(\delta)+2\sum J_\mu(\delta)\cos(\mu\omega_m t)], \\ m_b(t) &= 4(\frac{S}{P})\sum J_\nu(\delta)\sin(\nu\omega_m t)] \end{aligned} \tag{3.7}$$

$(\mu=2,4,.....)$

$(\nu=1,3,.....)$

are the time-varying modulation indices of the pattern and $J_{\mu,\nu}(\delta)$ are cylindrical Bessel functions of the first kind. Since the interference

pattern comprises two superimposed components, respectively shifted by $+\delta$ and $(\delta+\pi/2)$ with respect to the unmodulated beam interference pattern, we may define for convenience two time-varying modulation indices m_a and m_b as above.

By maintaining the lowest order terms of m_a and m_b, which represent the central and the first upper and lower modulation bands in the time-domain spectrum, we have for the present case obtained a solution for the usual differential equation[54,71,72] describing the temporal behavior of the space charge field in the AMP crystal:

$$E_{SC} = 2(\frac{ShJ_0}{P})\cos(\mathbf{K}\cdot\mathbf{r}+\delta) + 4(\frac{ShJ_1}{Pg})[1+(\frac{\omega_m}{g})^2]^{-\frac{1}{2}}\cos(\omega_m t+\varphi)\sin(\mathbf{K}\cdot\mathbf{r}+\delta)$$

$$\varphi = -\tan^{-1}(\frac{g}{\omega_m}), \qquad (3.8)$$

where the parameters:

$$g = -\frac{(1+\mathbf{K}^2 l_s^2)}{\tau_M(1+\mathbf{K}^2 r_D^2)},$$

$$h = \frac{iE_D}{\tau_M(1+K^2 r_D^2)}$$

involve :

E_D: Diffusion field

l_s: Debye screening length

τ_M: Maxwell relaxation time

r_D : Carrier diffusion length

and the parameter g represents the characteristic crystal response frequency f_c[54,71]. We underline that the second Lorentzian term in equation (3.8) above becomes negligible for modulation frequencies $f_m=\omega_m/2\pi$ greatly exceeding the characteristic frequency response, f_c, of the material. The first term of interest, however, which is responsible for useful PR grating recording incorporates a reduced index modulation, as compared to the case of unmodulated beams ($m_0=2S/P$), and it consequently implies a reduction in amplification gain.

We can obtain identical results by heuristically assuming either a small modulation depth δ, for which $J_0\rightarrow 1$, and $m_b\rightarrow 0$, which results in a stationary pattern or by alternatively considering the more generic case of time-averaging the intensity pattern in equation (3.6) over the crystal response time for $f_c<<\omega_m/2\pi$ for which we obtain again $m_a\rightarrow(2SP/I_0)J_0(\delta)$.

To illustrate further the above discussion we stress that recording is performed by the carrier frequency (central) band of the fields while the oscillating interference components produced by band-mixing reduce the overall interference pattern contrast and consequently the PR grating index modulation. Nevertheless, for a small input modulation depth δ, no apparent reduction in grating strength has been observed.

Simultaneous readout of the PR grating by beam $\mathcal{P}$ will produce an amplified output $\mathcal{S}_a$, which is the result of constructive interference between the transmitted signal and the scattered part of the pump beam. As it has been experimentally verified not only the component of the optical field $\mathcal{P}$ which corresponds to the center frequency ω but also the components of $\mathcal{P}$ at $\omega \pm \xi\omega_m$ (ξ=1, 2, 3,..) are participating in the scattering process. Information is transferred by this means from field $\mathcal{P}$ to field $\mathcal{S}$. The resultant field is given by:

$$\mathcal{S}_a = S[1 + (\frac{\sqrt{\eta}P}{S})\Sigma J_\xi e^{i(\xi\omega_m + \delta)}]e^{i(\omega t - k_s \cdot r)} \qquad (3.9)$$

The above consideration is valid as far as the frequency ξf_m of a particular component remains within the range implied by the Bragg selectivity frequency range[54], $\Delta f = c\cos(\theta a/2)/[d\sin^2(\theta a/2)]$ (where d is the interaction length and c is the speed of light), which is generally very large compared to the modulation bandwidth, and in our case exceeds the frequency bandwidth of the laser used. The available bandwidth estimated to the $\eta = 0.5\eta_{max}$ is $\Delta f \approx 125$ GHz in our case. This value sets a quite high operational frequency upper limit verifying the great potential of the scheme proposed.

The signal amplified in the crystal AMP, enters the PCM crystal and its phase-conjugate is generated. In the self pumping process no absolute phase reference for the incoming wave exists and thus the PCM

remains insensitive to any background (spatially uniform) phase changes imposed in the input. Scattering off the recorded set of gratings in the PCM will produce the output PC signal :

$$S_{PC} = S_a^*[\rho(1-\eta)]^{\frac{1}{2}} \tag{3.10}$$

We note that similar arguments regarding the available modulation bandwidth also apply for the self-pumped PCM. Nevertheless, as discussed in ref 73, this available PCM bandwidth exceeds several GHz. For the frequencies used in our experiments, no problem has been encountered.

The overall process preserves its real-time phase conjugation characteristics even though the AMP-PCM system responds in a slower fashion determined by the PR response. Any slowly varying phase shifts, intensity or angular variations of the input signal cause redistribution of the PR gratings within the response time of the crystals. The system is capable of slowly tracking the signal source.

3.4.2 Amplitude Modulation

It is readily apparent from equations (3.9), (3.10) that the PC field is phase modulated as well as amplitude modulated. Its intensity may be expressed as:

$$I_{PC} = S_{PC}S_{PC}^{*} = [\rho(1-\eta)]\{S^2 + \eta P^2 +$$

$$+ 2\sqrt{\eta}SP[J_0(\delta)\cos(\delta) + \sum J_{\mu}(\delta)\cos(\delta)\cos(\mu\omega_m t)$$

$$- \sum 2J_{\nu}(\delta)\sin(\nu\omega_m t)]\} \qquad (3.11)$$

(μ=2,4,...)

(ν=1,3,...)

The amplified signal intensity contains a bias as well as intensity modulation terms. The relative amplitudes of these terms depend on the value of δ. For a small value of δ, power is distributed mainly among the lower terms and thus we may consider only up to the first side band components of the PC field, representing DC and modulation at $\pm\omega_m$, and obtain:

$$I_{PC} = I_{DC}\{1 - 2[\frac{\sqrt{\eta}SPJ_1\sin(\delta)}{I_{DC}}]\sin(\omega_m t)\}, \qquad (3.12)$$

where: $I_{DC} = [\rho(1-\eta)][S^2 + \eta P^2 + 2\sqrt{\eta}SPJ_0\cos(\delta)]$

is the intensity of the central carrier frequency (time-domain) band. The output intensity modulation index, (M_{I1}), is given by:

$$M_{I1} = \frac{4[\rho(1-\eta)\sqrt{\eta}SPJ_1\sin(\delta)}{I_{DC}} \qquad (3.13)$$

Clearly, M_{II} remains at very low levels in any case and this fact prohibits the applicability of the present scheme in amplitude modulation applications. The above contrasts with the adaptive interferometry and detection schemes[64,66] in which large M_{II} should be considered.

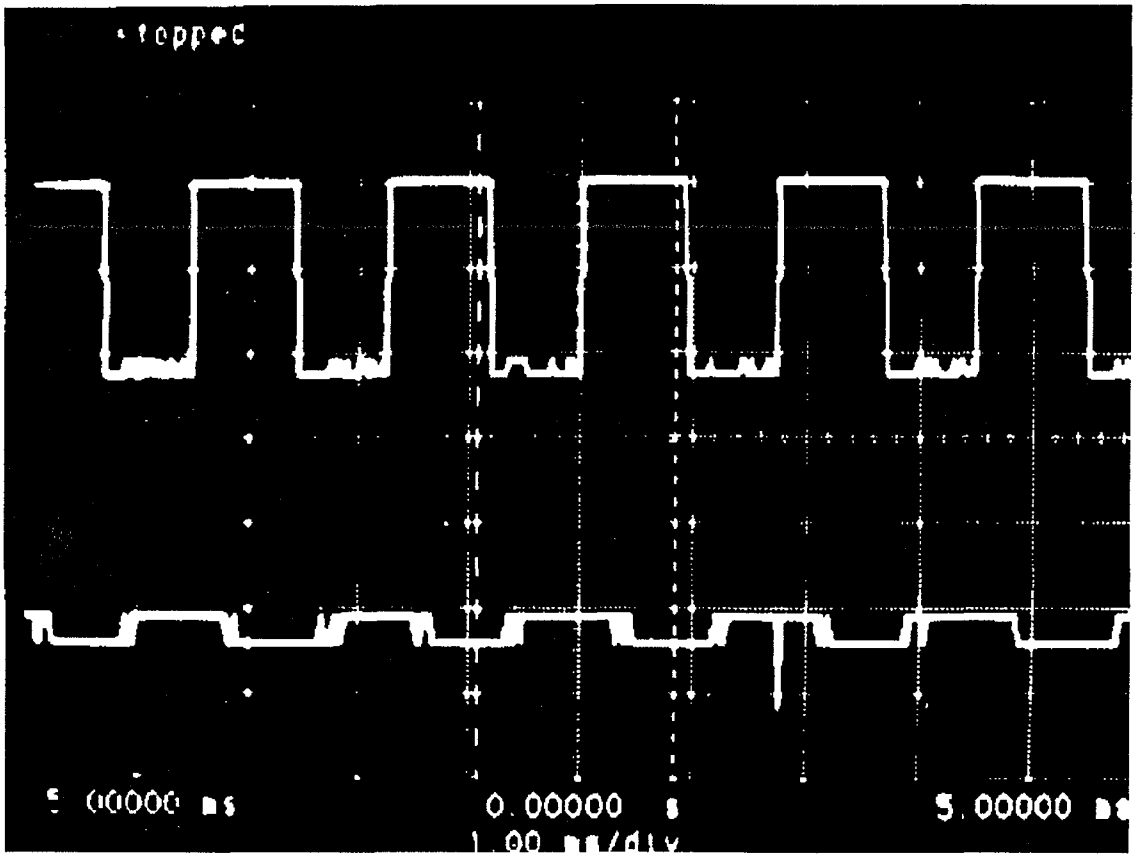

Figure 3.7 PC intensity modulation. Oscilloscope traces of the trigger voltage applied to the EOM (top trace) and the PC output intensity modulation (lower trace). The modulation is not detectable at high frequencies.

Figure 3.7 depicts a typical oscilloscope trace of the detected intensity modulation observed with the use of a phase-only modulated pump beam $\mathcal{P}$ with $\delta \approx 1.8$. The top trace depicts the square-wave trigger at a

frequency of ~570Hz applied to the EOM, and the lower trace depicts the resultant modulated intensity.

The actual voltage waveform applied at low frequencies is approximately a square-wave. We note here that even by carefully adjusting the modulation depth δ in order to maximize M_{I1}, the observed output intensity modulation depth remains below 2% and varies with amplification gain as in equation (3.13).

At very low modulation frequencies, comparable to the reciprocal of crystal response time, the observed output is a result of moving grating recording and follows the modulation frequency and/or its harmonics[68,74] depending on the magnitude of the phase modulation as described by eq. (3.8).

3.4.3 Phase Modulation

Let us now consider, without making any further assumptions regarding the input modulation depth, the case of phase modulation. From equations (3.9), (3.10) we obtain for small signals:

$$S_{PC} \approx S\sqrt{\gamma}[\rho(1-\eta)]^{\frac{1}{2}}[\sum J_{\xi} e^{i(\xi\omega_m+\delta)}]e^{i(\omega t+\mathbf{k}_s\cdot\mathbf{r})} \qquad (3.14)$$

from which it is readily apparent that the PC field becomes modulated with a phase modulation depth δ identical to that of the pump beam. The above expression certifies the potential of the scheme in phase modulation applications. We note that a small modification on the

output modulation occurs by inclusion of a finite signal, which nevertheless corresponds to a low amplification gain situation.

Experimentally, homodyne detection is applied to observe the output. The interference between $\mathcal{S}_{pc}$ ($S_{PC}=\kappa S_a$) and a reference field $\mathcal{A}=A\exp(i\omega t)$ will result in a temporally modulated intensity given by:

$$I_{int} = (A+S_{PC})(A+S_{PC})^*$$

$$= (A+kS)^2 + k^2\eta P^2 + 2k^2\sqrt{\eta}P(A+kS)\cos[\delta + \delta\sin(\omega_m t)]$$

$$= (A+kS)^2 + k^2\eta P^2 + 2k^2\sqrt{\eta}P(A+kS)$$

$$\times[J_0(\delta)\cos(\delta) + \sum 2J_\mu(\delta)\cos(\delta)\cos(\mu\omega_m t)$$

$$-\sum 2J_n(\delta)\sin(\delta)\sin(\nu\omega_m t)]$$

$$\mu=2,4,\ldots..,\ \nu=1,3,\ldots., \qquad (3.15)$$

which is detected by a fast photodiode. The temporal modulation index of the interferometer output is a function of A and is generally given for the $\xi\omega_m$ spectral component by:

$$M_{P\xi} = \frac{m_0 J_\xi \begin{cases}\sin\\ \cos\end{cases}(\delta)}{1+m_0 J_0\cos(\delta)} \qquad (3.16)$$

where m_0 represents the modulation index with no phase modulation and sin(•) or cos(•) terms are used for odd and even harmonics

respectively. The above $M_{P\xi}$ index can be maximized for the particular ξth harmonic by adjusting δ and maintaining $m_0=1$.

Figure 3.8(a) shows typical traces of the interferometrically detected PC output. The top trace depicts the trigger to the EOM modulator and the lower trace depicts the observed output.

This agrees with our low modulation assumption preventing decrease of gain. As we have presented in equation (3.14) the modulation depth of the PC output δ_{pc} is expected to be nearly equal to the input modulation δ. A maximum input modulation index of about 60% for the fundamental f_m is attained at low frequencies for which $\delta \approx 1.8$rad. This is in full agreement with equation (3.16). The input modulation is decreasing with frequency to about 10% for 10kHz due to limitations in the electronics. Figure 3.9 shows the experimentally determined input and output modulation indices as a function of frequency. A 10% estimated error is due to vibrations. The output modulation index may be used to determine the actual modulation transfer function of the system.

However, a direct normalization is not possible in the present case as the real modulation transfer function of the system is a function of amplification gain which is, in turn, affected by the input modulation depth.

a)

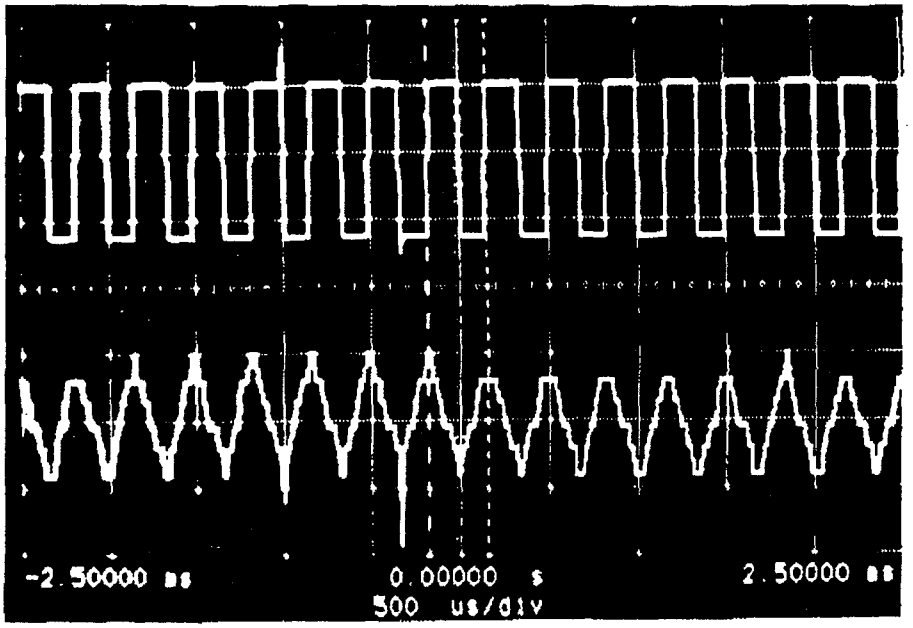

b)

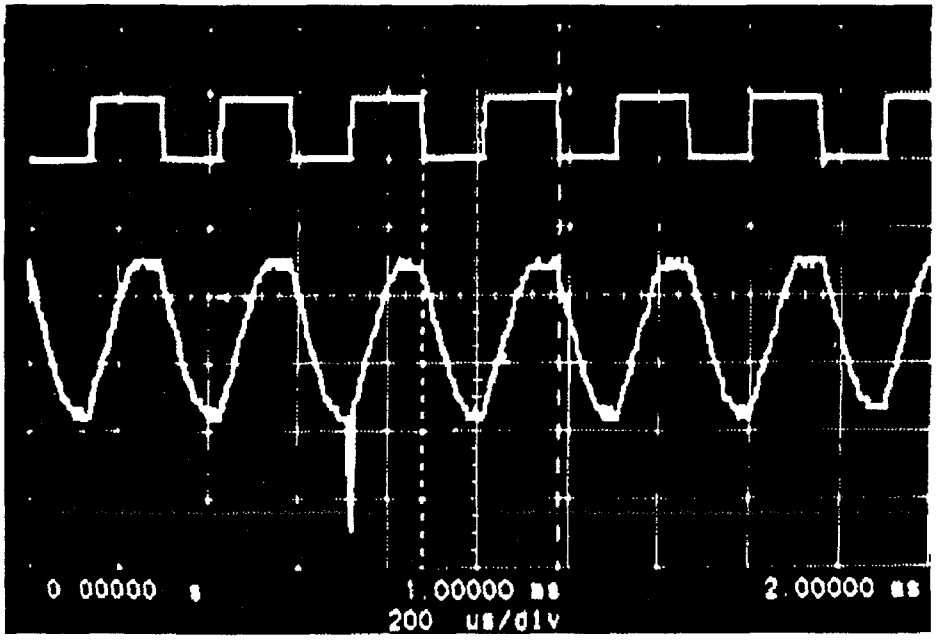

Figure 3.8 PC phase modulation. (a) Oscilloscope traces of the interferometer output detecting the PC beam (lower trace); corresponding trigger to the EOM driver (upper trace). (b) Example of interferometrically detected input phase modulation (of beam P) in the same frequency range (lower trace) and trigger to the EOM (upper trace).

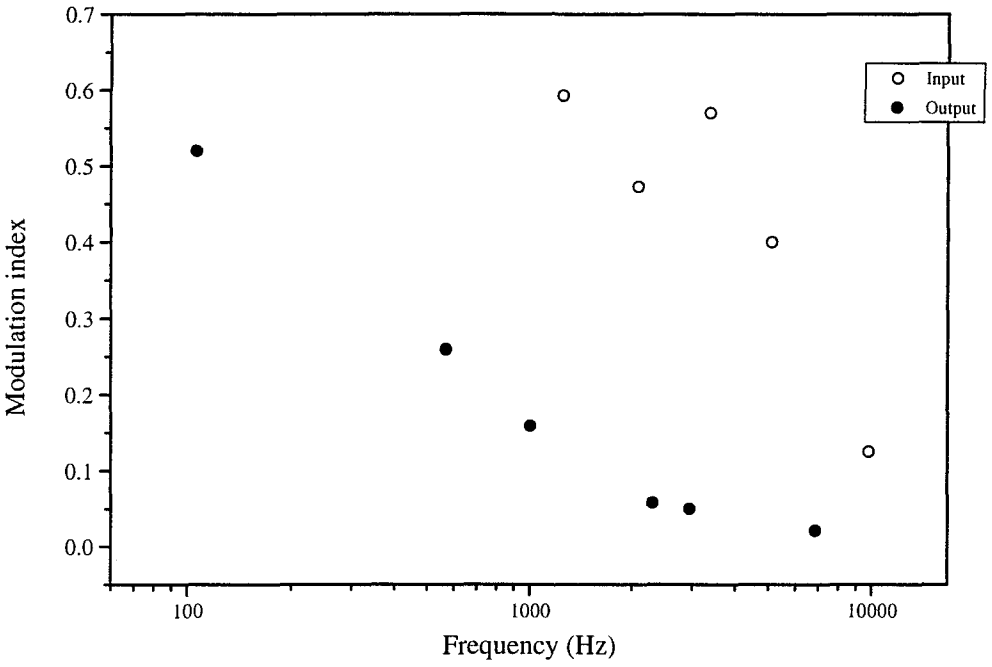

Figure 3.9 Interferometrically observed modulation indices as a function of frequency. Experimentally observed PC output modulation index (solid points) and corresponding input modulation index (phase modulation of pump) (open circle).

As far as the output modulation index is concerned, by examining equation (3.16) in combination with equation (3.14) we observe that the index m_0 becomes inversely proportional to the input phase modulation depth δ and this reflects in the fast drop of the detected M_{P1} at high frequencies, since the intensity of the reference beam A used was kept constant. However at low input modulation depth, low input signals and high gain operation a flat phase-modulation transfer function near unity is expected. Limitations may arise only at very high modulation frequencies and further investigation is in progress.

3.5 Adaptive multichannel signal transmission and switching

In another realization more than one pump beams at different optical frequencies are used. These beams may be phase modulated and said to represent distinct information channels. A single signal beam may extract the information from each of the above channels in an adaptive transmission mode, as described in the previous sections, by tuning its optical frequency to the desired channel. Switching between different information channels is thus achieved by simply shifting the frequency of the signal beam.

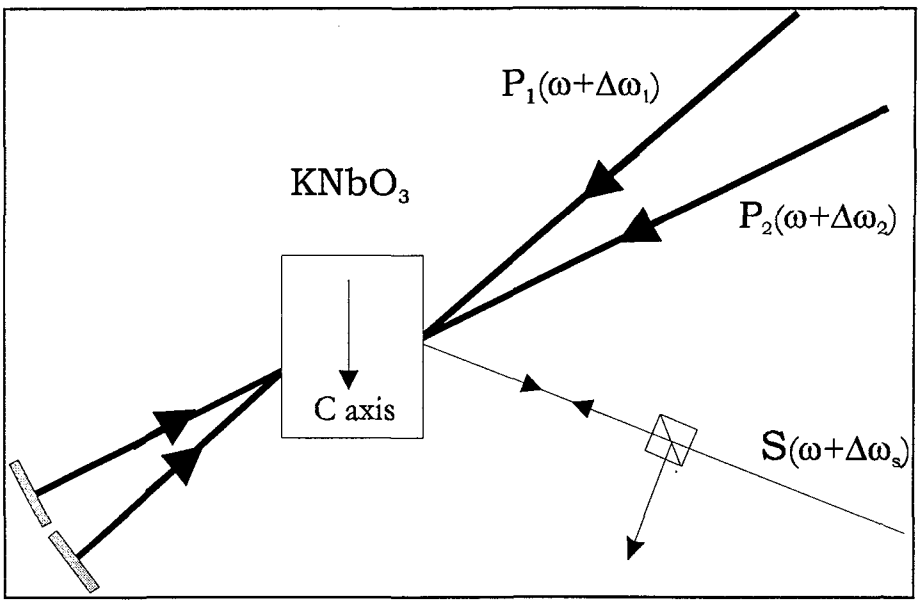

Figure 3.10 Experimental setup for multibeam adaptive transmission and switching.

Preliminary results of a setup capable of performing the above described operation are presented here. The system consists of a single phase conjugate mirror utilizing a $KNbO_3$ crystal in a four wave mixing

arrangement depicted in Figure 3.10. In this "demonstration" setup two pump beams P_1 and P_2 are mixed with a signal beam S. All three beams are frequency shifted by the use of piezoelectrically driven mirrors (PZMs).

The original beams are provided by a HeCd laser and they are mutually coherent. After reflection on the surface of a PZM, driven by a saw-tooth function, the beams P_1, P_2, S are frequency shifted by $\Delta\omega_1$, $\Delta\omega_2$, $\Delta\omega_S$,respectively. If the frequency shift is larger than the inverse response time of the $KNbO_3$ crystal no photorefractive grating is recorded.

By adjusting the frequency of the signal beam, to match the carrier frequency of one of the pumps, a grating between the two beams S and P_j is recorded. Information can thus be transferred between a pump and the signal and return back as a phase conjugate replica of the signal beam. Different pump beams may have different frequency shifts, thus switching between different ports, represented by the pump beams, is achieved.

Additional phase modulation of the participating pump beams at frequencies well above the characteristic response of the crystal will not affect the grating recording. As shown in the previous sections, due to the crystal inertia, the information content will be transferred at the phase conjugate output of the signal beam.

The detection of the phase conjugate reflection was performed by introducing (for convenience) a slight vertical misalignment of the readout beams so that the diffracted (not exact phase conjugate) output beams appeared at different locations. Extension of the system's performance can be achieved by the use of fan-out diffractive elements[75], studied in parallel to this activity, for the generation of an array of beamlets.

Multiple beam setups have been presented before[76], where the possibility of using a dynamic grating for fan-in and fan-out of multiple beams was investigated. There is a limit on the amount of gratings that can be recorded in the same crystal volume introduced due to the finite dynamic range and bragg selectivity of the specific photorefractive crystal used. However, for the case investigated in this work no such limit exists since only one photorefractive grating is recorded. However, the beams that are not participating in the photorefractive recording, affect the recorded grating by reducing its contrast.

3.6 Conclusions

In conclusion we have presented and analyzed the operational characteristics of an adaptive transmitter system based on the combined operation of two photorefractive crystals, an amplifier and a conjugator. The system is capable of generating amplified, phase-modulated, phase-conjugate signals of low-intensity probe signal fields.

The generation of amplified PC replicas is seen to be limited to within a specific range of low input signal intensities but this conforms with potential applications.

The interesting case of phase modulation at frequencies greatly exceeding the characteristic response of the PR materials has been investigated. We have argued that the temporal frequency side bands, representing the information content of the signal, are utilizing the gratings actually written by the central carrier frequency band, in order to generate phase-modulated, amplified phase conjugate signals. Even though the system has been tested at relatively low frequencies, the operation is based on the utilization of the photorefractive grating inertia and thus the method could be extended to very high frequency, in the GHz range, operation. Further, it may also be applicable to guided-wave architectures. The overall system is seen to preserve its real time phase-conjugation character. Additionally, the system was extended for multi-pump beam operation and a single crystal demonstration system is presented. Such a method of performing an adaptive interconnection amongst information channels may lead to a novel architecture and requires further attention.

Considering these unique properties, the scheme presented here may be seen as a potential *adaptive transmitter system* capable of real-time *receiver tracking*, all-optical *signal modulation* and *amplified phase-conjugate signal transmission*

Chapter 4

PHOTOREFRACTION AT 780 nm IN $Bi_{12}SiO_{20}$ CRYSTALS: EFFECTS AND APPLICATIONS

4.1 Introduction

The dynamic nature of photorefractive (PR) holographic recording makes photorefractive crystals promising candidates in the area of optical signal and image processing. The 3-D nature of holographic recording in PR crystals enables the storage of a large amount of information. However, the high sensitivity and the relatively short response time that these materials exhibit, limit applications in which direct long storage of information is desired. For this reason, several hologram fixing techniques have been developed, leading to either permanent or semipermanent holographic recording. The formation of extended-lifetime holograms in photorefractive materials has been attributed, depending on the type of the recording and the material used, to the photochromic effect[51], thermal fixing[77], electrical fixing[78], two-photon absorption[79], and complementary grating formation[80,81,82,83]. The last method, which has been accomplished experimentally by temperature tuning and storage in the dark or application of electric fields and prolonged recording, involves the creation of secondary charge carriers inside the material (e.g. $KNbO_3$,

BSO, BTO, $BaTiO_3$), which in turn move under the influence of the electric space charge field created by the primary charge carriers. Both the visible and the near infrared portion of the electromagnetic spectrum have been used in the formation and revelation of these extended lifetime holograms.

In this chapter photorefractive recording of holograms which exhibit extremely long lifetimes at 780 nm in $Bi_{12}SiO_{20}$ is investigated[84]. No special fixing technique is required for the extension of hologram lifetime and a very simple recording method was used based on a typical four wave mixing arrangement. The photorefractive recording is found to present a dual temporal behavior, fast and slow. The recorded slow hologram exhibits a decay time typically of thousands of seconds, even with relatively high reading beam intensities of several tens of mW/cm^2. The extension of the hologram lifetime is attributed to the existence of two different charge carriers (electrons and holes) excited from different types of active centers, activated by the near infrared radiation, which take part in the photorefractive recording process. The presence of two distinct charge carriers gives rise to the creation of two different space charge distributions (SCD) interacting with each other, thus extending the decay time periods beyond those corresponding to the individual relaxation time constants.

A theoretical model[85,86], which explains the role of electron-hole transport in the development of such gratings as well as the

experimentally observed dynamics of recording and erasure has been investigated and discussed further. The model presented in this chapter can be also applied for the, all optical, determination of a number of photorefractive parameters such as effective trap density, diffusion length and dielectric relaxation time.

Uniform preillumination of the crystal with light of shorter wavelength causes enhancement of the semipermanent recording. This effect, which is also observed with prior spatially modulated illumination, can be used for the selective sensitization of the material. This is attributed to the density changes of the active centers responsible for semipermanent recording in the illuminated area of the crystal. This enhanced semipermanent recording leads to incoherent-to-coherent-information-transfer and also to potential image processing schemes, some of which are exploited here.

4.2 Two-level photorefractive effects in the N.I.R

4.2.1 Experimental Considerations

The experimental arrangement depicted in Figure 4.1 is a typical four wave mixing setup which incorporates a single, nominally undoped, BSO crystal [110] cut and oriented for maximum diffraction efficiency. The laser used for both hologram recording and reconstruction was a single transverse-single longitudinal mode diode laser, delivering ~30mW of average power at 780nm. The Phase Conjugate (PC) output

was monitored by a pico-Watt power meter facilitating observations of the development and decay of the grating. The angle between beams S and P, having intensities I_S and I_P respectively, was varied so that a fringe spacing with values from 0.6μm to 2.2μm could be achieved.

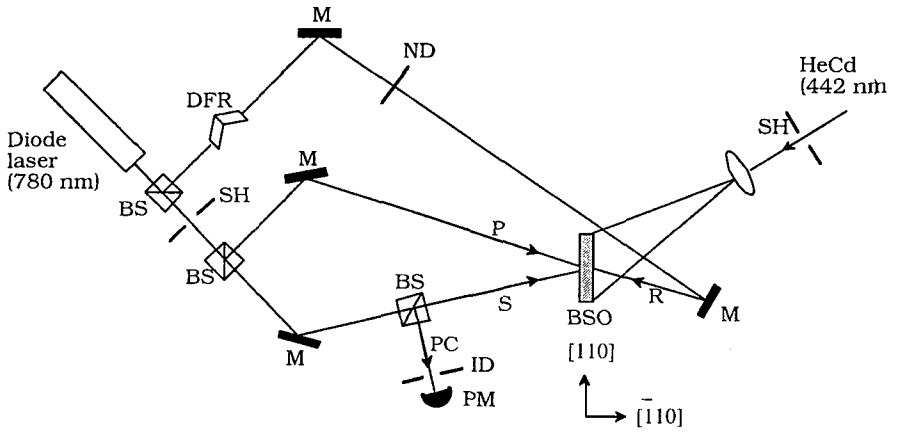

Figure 4.1 Schematic of the experimental arrangement used for grating recording and readout in BSO. P,S and R: optical beams at 780 nm, PC: Phase Conjugate signal, BS: Beam splitter, M: Mirror, SH: Mechanical Shutter, IR: Iris Diaphragm, ND: Neutral Density filter, PM: Power Meter head, DFR: Double Fresnel Rhomb.

The intensities of the two writing beams during the hologram development and decay experiments were I_S=115.6mW/cm^2 and I_P=119.6mW/cm^2, while the intensity of the reading beam R, I_R, varied from 56.6mW/cm^2 to 21.3mW/cm^2 and could be reduced further to very low levels.

The polarization of the writing beams was perpendicular to the plane of incidence, the reading beam, however, was guided through a double

Fresnel rhomb causing polarization rotation for determining the nature of holograms recorded.

During recording all the beams are present so that the development of holograms can be monitored in real time. A HeCd laser, a HeNe laser, and a usual polychromatic source were used for erasing all photorefractive gratings stored in the crystal between successive experimental runs and also for enhancing the semipermanent recording. No electric fields were applied on the crystal at this stage and thus recording takes place in the diffusion regime. A shutter was used to block both writing beams, thus enabling the uniformly illuminating reading beam to monitor the decay of the recorded holograms. A second shutter was used to control the beam of the HeCd laser.

4.3 Observations and analysis of hologram competition effects.

The holographic recording in BSO crystals at 780 exhibits a dual temporal behavior with respect to exposure time. For short exposures (less than 30 sec) the crystal exhibits the normal photorefractive behavior. The PC output, which is proportional to the diffraction efficiency of the recorded hologram, develops and saturates after a few seconds. During erasure, the PC signal decays to zero under uniform illumination of the reading beam I_R. If the recording time exceeds 30

sec or if the crystal is uniformly preilluminated by the HeCd beam, the following sequence of events is observed. During the writing period and after the fast grating saturation occurring, a systematic decrease of the diffraction efficiency is observed as depicted in Figure 4.2. By blocking the writing beams a rapid drop followed by a rise of the diffraction efficiency (Phase B) is observed which after a few seconds reaches a maximum (Phase C) .

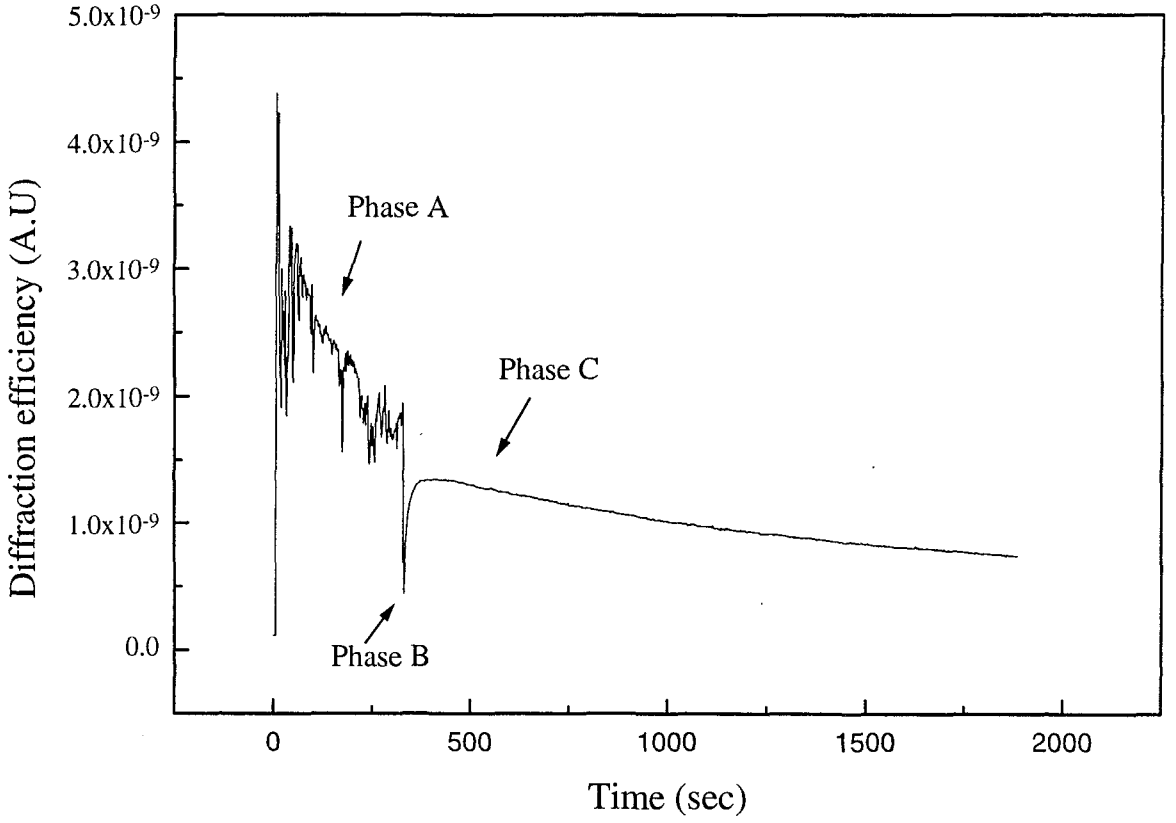

Figure 4.2 Temporal behavior of the PC beam intensity during recording and erasure of the hologram combination for a recording period of 2 minutes and fringe spacing of 1 μm. Phase A: evolution of the overall hologram recording, Phase B: rapid decay and Phase C: observation of the semipermanent, slow decaying, hologram.

The remaining hologram decays with an extremely slow rate even though the reading beam intensity is kept quite high. This nearly permanent holographic grating is not affected by ambient room illumination and temperature. The photorefractive nature of this remaining slow-response hologram has been verified by a polarization dependence experiment. Having the polarization of the reading beam rotated by the double Fresnel rhomb, the diffraction efficiency showed no polarization dependence in contrast to the case of multiplexed photochromic and photorefractive gratings[87]. The polarization dependence results are depicted in Figure 4.3.

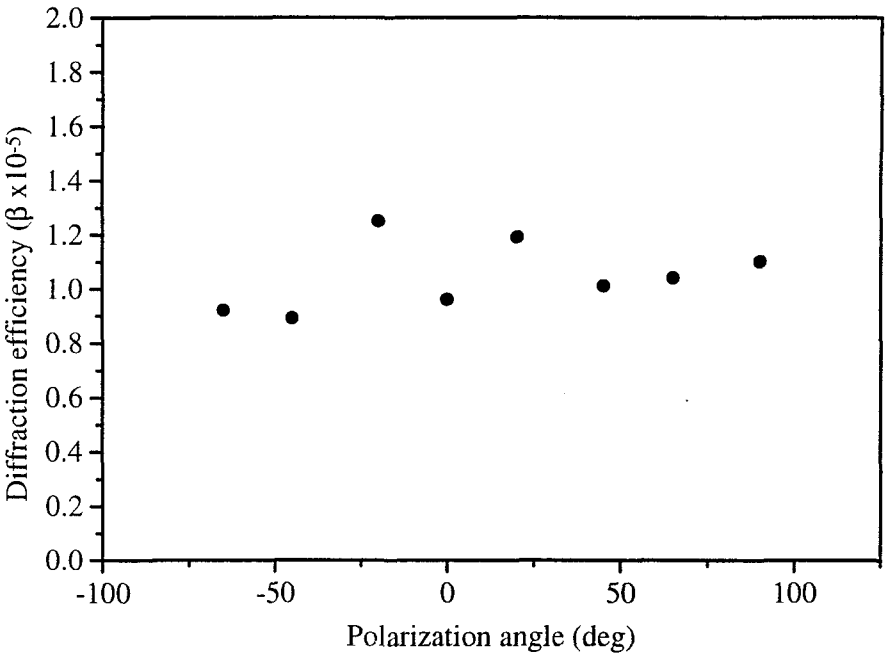

Figure 4.3 Dependence of the diffraction efficiency of the slow grating component upon readout beam polarization state.

The associated errors are attributed to the double Fresnel rhomb imperfections. Furthermore, no coloration of the crystal over the interaction region, inherent in photochromism, was observed.

The temporal behavior of the overall grating, depicted in Figure 4.2and described above, can be explained by considering the existence of a second PR grating, with a much slower response, which is shifted with respect to the principal fast one. The two gratings are attributed to the existence of two different space charge distributions (SCD), caused by the periodic spatial distribution of electron and holes excited by the near infrared radiation from two different active centers. The two space charge distributions are recorded simultaneously and they interact with each other. The development of the slow response SCD, due to holes, is yielding a decrease of the diffraction efficiency, shown in phase A of Figure 4.2, due to the presence of a π-shift with respect to the already saturated electron SCD.

When the writing beams are blocked, the uniformly illuminating reading beam causes redistribution of the charges, and thus decay of the overall grating. Because of the response time difference between the two SCD the fast one decays first (Phase B) and diminishes. Finally the slow decaying hologram is revealed (Phase C).

Close examination of Figure 4.2shows that the diffraction efficiency does not reach a zero value as it was expected from the assumed π-

shift between the two gratings (i.e. complete compensation when the two gratings have equal strengths). Similar effects have been observed in works performed in the visible[88,89] and the near infrared[81] region and a variety of explanations were given involving the incorporation of a non shifted photochromic grating[88] or assuming a non π-shift between the two gratings[80]. In ref 89 the non zero value of the minimum reached was attributed to vibrations which alter the relative phase between the two writing beams. The random phase fluctuation caused by vibrations is sensed by the fast response (transient) grating leading to a relative non π-shift between the two gratings. This phase shift is also responsible for the large fluctuations of the diffraction efficiency observed during recording which are caused by the random movements (due to vibrations) of the fast electron grating with respect to the slow responding hole grating. In the present experiments an increase of the deviation from zero with exposure time is observed. This increase of the deviation with increasing exposure is due to the increasing strength of the semipermanent grating which becomes comparable to the fast one. Phase fluctuations cause, therefore, larger expected intensity deviations verifying the random nature of this effect.

An estimation of the amplitude of the slow photorefractive grating due to hole SCD is given by the peak diffraction efficiency depicted in phase C of Figure 4.2. For long recording time periods very large diffraction efficiency of the slow grating is observed, which is comparable to the

diffraction efficiency of the fast gratings. The decay time of the slow hologram is also a function of the Bragg angle between the two recording beams.

In Figure 4.4 the decay of the slow hologram component is plotted for various fringe spacing values. It is observed that the decay time increases with decreasing fringe spacing. These fringe spacing dependence results agree with predictions of the theoretical model discussed here.

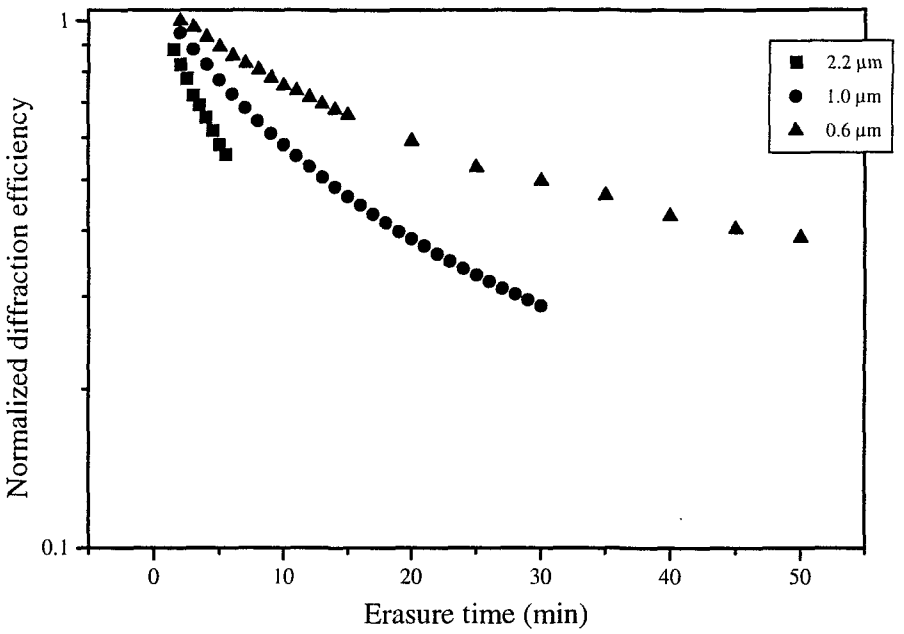

Figure 4.4 Decay of the observed slow hologram for various fringe-spacing values under uniform illumination with beam R with intensity I_R=56.6 mW/cm^2.

The longest observed decay time with I_R=56.6mW/cm^2 was τ=2160sec is corresponding to a fringe spacing of Λ=0.6 μm. Much longer decay

time periods than those shown in Figure 4.4 are observed for smaller reading beam intensities (3600sec for I_R=21.3mW/cm^2).

Uniform illumination with HeCd laser radiation enhances the semipermanent recording. This can be explained in terms of excitation of levels lying relatively deep inside the energy gap, producing free holes. Those get trapped in shallow states and they subsequent participate in the photorefractive process.

4.4 Theoretical Analysis

The departure from the usual photorefractive behavior, having holographic gratings erased by uniform illumination while they exhibit a simple exponential decay, has led investigators to propose charge transport models other than the single-level unipolar model of Kukhtarev[6]. Models which incorporated either two types of carriers[90], or multi-levels of impurities[91], but not both, failed to explain this anomalous behavior. Finally, Kukhtarev[92] and Valley[93] proposed a bipolar two-level transport model which predicted the multiple exponential decay that experimentalists had observed. According to their theory, one level closest to the conduction band participates in electron only transport and the other which is closest to the valence band in hole only transport. Bashaw[86] and Zhivkova,[85,94] independently, extended the work of Kukhtarev and Valley to solve analytically the materials equations (under the usual quasi-steady-

state approximation) for the time evolution of the amplitudes of the two gratings due to electrons and holes. Therefore, the evolution of the diffraction efficiency of the total holographic grating formed inside the crystal is obtained.

The description of the theoretical model starts with the incorporation of two independent sets of photoactive levels in the energy band gap. Electrons are the dominant carriers for the levels lying closer to the conduction band, and holes for those closer to the valence band. The electron transport system has a fixed number, N, of centers, N^+ of which are empty and N^- are electron filled. In the absence of charge gratings (i.e. dark) the corresponding concentrations are N_0^+ and N_0^-. For the hole transport system the corresponding quantities are P , P^+, P^- , and P_0^+, P_0^-. Overall charge neutrality is assumed. It is also assumed that a nonequilibrium state exists where both of these levels are partially filled and therefore photoinduced charge transport is possible. Furthermore, if the photon energy of the recording beams is less than half the band gap (as it is the case with the present work in which radiation at 780nm, corresponding to 1.59eV, is used to write gratings in BSO with band gap of 3.25eV), the cross excitation between the two levels is minimal. Sufficiently small values of hole-capture and electron-capture cross sections for the two systems respectively, also assures minimal cross relaxation. Finally, both levels are considered deep rather than shallow, and therefore none is thermally depleted.

For photorefractive crystals of sufficiently small thickness (~1 or 2mm) and for orientation geometries where there exist negligible beam coupling, the diffraction efficiency can be considered as being proportional to the square of the magnitude of the electric space charge field, E_{SC}, that is created in the crystal. E_{SC} can be calculated by solving Kuchtarev's materials equations which describe the physical processes in the crystal. These equations are presented in ANNEX 1 by considering only electron photoconductivity and include equations for the ionization rates, current densities, as well as continuity equations for both electron and hole systems:

$$\frac{\partial N^+}{\partial t} = (\beta_n + s_n I)(N - N^+) - \gamma_n N^+ n \tag{4.1}$$

$$\frac{\partial P^+}{\partial t} = (\beta_p + s_p I)P^+ - \gamma_p (P - P^+)p \tag{4.2}$$

$$\frac{\partial n}{\partial t} = \frac{\partial N^+}{\partial t} + \frac{1}{e}\frac{\partial J_n}{\partial x} \quad , \quad \frac{\partial p}{\partial t} = \frac{\partial P^+}{\partial t} - \frac{1}{e}\frac{\partial J_p}{\partial x} \tag{4.3}$$

$$J_n = e\mu_n nE + eD_n \frac{\partial n}{\partial x} \quad , \quad J_p = e\mu_p nE + eD_p \frac{\partial p}{\partial x} \tag{4.4}$$

Where β_i, s_i, γ_i, μ_i, D_i, are the dark generation rates, photoexcitation cross section, mobilities, and diffusion coefficients for electrons (i=n) and holes (i=p).

The coupling between the two transport mechanisms comes from Poisson's equation which relate to both N^+ and P^+ as follows.

$$\frac{\partial E}{\partial x} = \frac{e}{\varepsilon_0 \varepsilon_r}(p - n + N^+ + P^+ - N_{dark}) \tag{4.5}$$

Where N_{dark} are all the optically inactive charges that compensate the existence of N^+ and P^+ in the dark.

By following the standard linearization method, already presented in chapter 1, all the periodic quantities of interest, including the illuminating intensity distribution $I=I_0(1+m\cos(Kx))$ (where m is the modulation depth and K is the grating wavevector), are approximated by only the zero- and first-order Fourier harmonics and are given for example by:

$$N^+(t,x) = N_0^+ + N_1^+(t)e^{iKx} + c.c \ , \ P^+(t,x) = P_0^+ - P_1^+(t)e^{iKx} + c.c \tag{4.6}$$

Assuming quasi-steady state conditions and recording beams of relatively low intensity, the material equations can be simplified enough to yield a system of two coupled first order temporal differential equations concerning the first order magnitudes of the two gratings (as represented by the populations N_1^+ and P_1^+). Straightforward solution of these equations yields

$$N_1^+(t) = -\frac{B_1C_2 - B_2C_1}{a_1a_2} - \frac{a_1 + B_2}{A_2}K_1e^{a_1t} - \frac{a_2 + B_2}{A_2}K_2e^{a_2t} \tag{4.7}$$

$$P_1^+(t) = -\frac{C_1A_2 - C_2A_1}{a_1a_2} + K_1e^{a_1t} + K_2e^{a_2t} \tag{4.8}$$

$$\text{where: } A_1 = -B_1\left(1+\frac{E_D - iE_0}{E_{qn}}\right),\ A_2 = \frac{-1}{\tau_{mp}[1+L_{Dp}^2K^2+iKL_{0p}^2]}$$

$$B_1 = \frac{-1}{\tau_{mn}[1+L_{Dn}^2K^2+iKL_{0n}^2]},\ B_2 = -A_2\left(1+\frac{E_D - iE_0}{E_{qp}}\right) \qquad (4.9)$$

$$C_1 = -\frac{m\varepsilon_r\varepsilon_0}{e}K(E_D - iE_0)B_1,\ C_2 = -\frac{m\varepsilon_r\varepsilon_0}{e}K(E_D - iE_0)A_2$$

$$K_1 = \frac{a_1C_2 + A_1C_2 - A_2C_1}{a_1(a_1 - a_2)},\ K_2 = \frac{a_2C_2 + A_1C_2 - A_2C_1}{a_2(a_1 - a_2)}$$

$$a_{1,2} = \frac{-(A_1+B_2) \pm [(A_1+B_2)^2 + 4A_2B_1)]^{\frac{1}{2}}}{2} \qquad (4.10)$$

In the above equations, E_D, E_{qn}, E_{qp} are the characteristic fields of the crystal (diffusion, saturation fields) and they are given by

$$E_D = \frac{k_BT}{e}K,\ E_{qn} = \frac{e}{\varepsilon_r\varepsilon_0K}N_{eff1}, E_{qp} = \frac{e}{\varepsilon_r\varepsilon_0K}N_{eff2} \qquad (4.11)$$

Where the effective trap densities for the two transport systems are:

$$N_{eff1} = \frac{N_0^+N_0^-}{N} = \frac{N_0^+(N - N_0^+)}{N},\ N_{eff2} = \frac{P_0^+P_0^-}{P} = \frac{P_0^+(P - P_0^+)}{P} \qquad (4.12)$$

τ_{mn}, τ_{mp}, are the dielectric relaxation times, τ_n, τ_p are the respective lifetime constants of the free carriers given by:

$$\tau_{mn} = \frac{\varepsilon_r\varepsilon_0\gamma_nN_0^+}{e\mu_n(s_nI_0+\beta_n)N_0^-},\ \tau_{mp} = \frac{\varepsilon_r\varepsilon_0\gamma_pP_0^-}{e\mu_p(s_pI_0+\beta_p)P_0^+} \qquad (4.13)$$

$$\tau_n = \frac{1}{\gamma_n N_0^+} \quad , \quad \tau_p = \frac{1}{\gamma_p (P - P_0^+)} \tag{4.14}$$

Their diffusion and drift transport lengths are: L_{Dn}, L_{Dp}, L_{0n}, and L_{0p} respectively and are given by:

$$L_{Dn}^2 = \frac{k_\beta T}{e}\left(\frac{\mu_n}{\gamma_n}\right)\frac{1}{N_0^+}$$

$$L_{Dp}^2 = \frac{k_\beta T}{e}\left(\frac{\mu_p}{\gamma_p}\right)\frac{1}{(P - P_0^+)} \tag{4.15}$$

$$L_{0(n,p)} = \mu_{n,p}\tau_{n,p}E_0$$

The complex amplitude of the fundamental Fourier component of the electric space charge field is then:

$$E_{SC} = \frac{ie}{\varepsilon_r \varepsilon_0}[P_1^+(t) - N_1^+(t)] \tag{4.16}$$

Equations (4.7), (4.8) and (4.16) represent some of the main results of this model. They show that the distributions of negative and positive charges form and evolve inside the crystal simultaneously during the recording stage i.e. when the crystal is illuminated by a non-uniform intensity distribution. Each of them is strongly influenced by the presence of the other, as it can be seen by the temporal dependence of the evolution of each grating on two time constants $1/a_1$ and $1/a_2$. It must be emphasized here that each time constant depends on the material characteristics (e.g. concentrations of impurity levels,

mobilities, recombination coefficients etc.) of both electron and hole systems. This represents some difficulty in evaluating the two time constants separately, as it is generally difficult to experimentally measure some of the above parameters for both electrons and holes in a photorefractive crystal.

It is interesting to note that the above theory reduces to the single-level unipolar model of Kukhtarev when only one type of impurities is present. If this is the case, then $|a_1| = |A_1|$ and therefore the response time of, for example, the electron system is $\tau_1 = -1/a_1 = 1/A_1$ This is exactly the Kukhtarev's expression for the response of a photorefractive grating with both diffusion and drift present. Similarly, $\tau_2 = -1/B_2$ for a hole only system.

In the current situation, where both types of charge transport systems are present, it is useful to consider one limiting case in which transport is dominated by electrons. In this case, $A_1 >> B_2$, or equivalently $\tau_1 << \tau_2$, meaning that the response of the hole grating is much slower than the one of electrons. Even though both gratings start forming at the same time, the electronic one (primary) reaches saturation much faster. If the recording illumination stays on long enough, then the effect of the increase in the amplitude of the hole grating is evident in the form of a slow decrease in the amplitude of the total grating (compensation of the hologram).

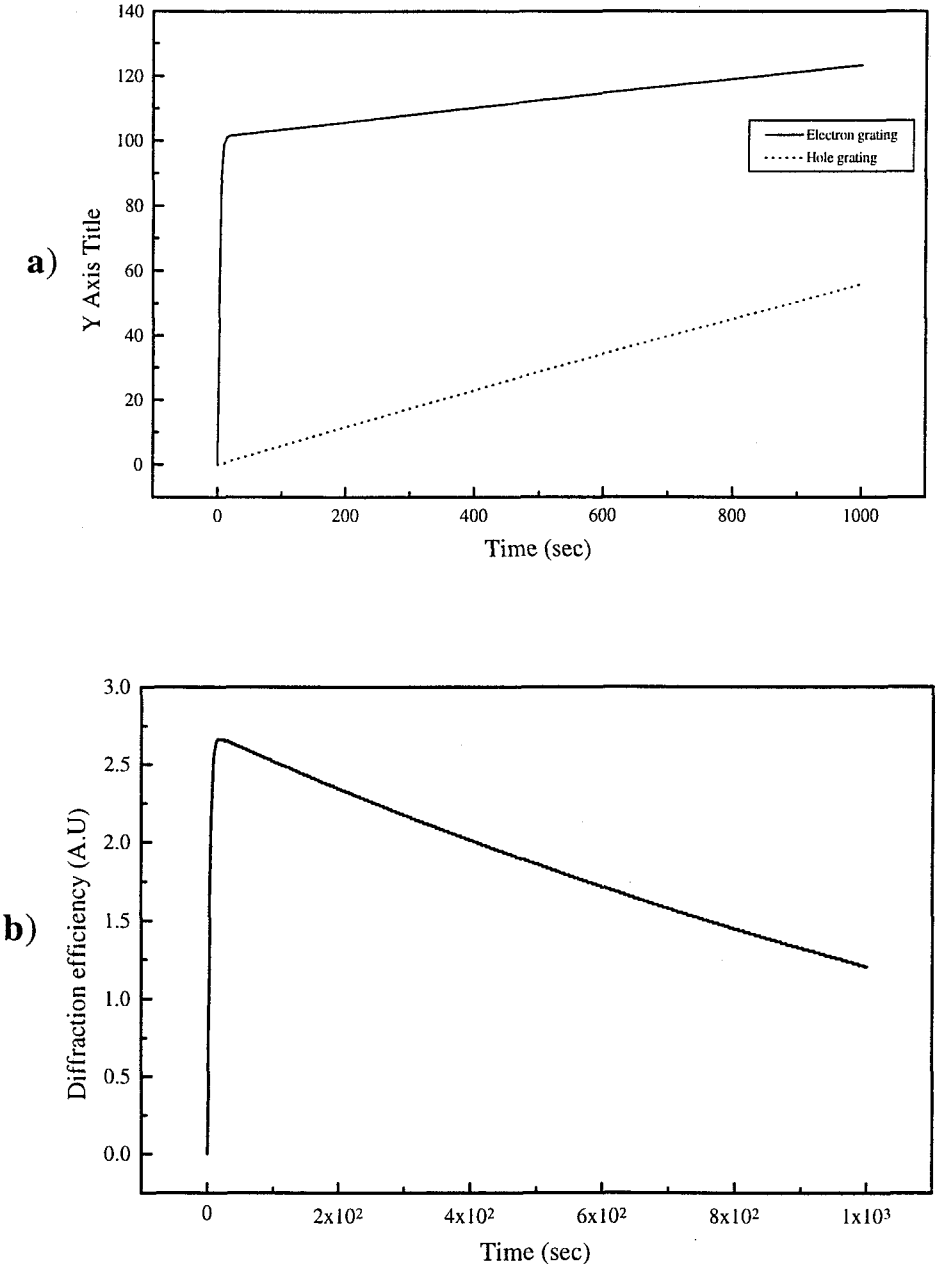

Figure 4.5 Theoretical curves of (a) the evolution of the electron grating (solid line) and the hole grating (dot line), during recording, (b) The resulting diffraction efficiency from the two gratings as a function of time. The parameters used for the curve calculation are: $\Lambda=1\mu m$, $E_0=0$ KV/cm, $N_{eff1}=2x10^{21}$ m^{-3}, $N_{eff2}=1.2x10^{25}$ m^{-3}, $L_{Dn}=1.7x10^{-5}$ m, $L_{Dp}=2.7x10^{-7}$ m, $\tau_{mn}=5.8x10^{-4}$ sec, $\tau_{mp}=1570$ sec.

Figure 4.5(a) shows theoretical curves of the evolution of the two gratings in the diffusion case (E_0=0), for Λ=1μm. The grating due to electrons (solid line) reaches saturation much faster than the secondary grating. The net result represented by the diffraction efficiency of the total grating can be seen in Figure 4.5(b) where the compensation phase is apparent.

According to the above discussion, prolonged illumination of the photorefractive crystal allows the secondary grating to increase in strength and, for long enough recording time, to completely compensate the primary grating. However, in order to exploit the longer lifetime of this hologram, for such applications such as optical signal processing and multiple image storage in associative memories, its contribution to the total diffractive properties of the crystal must be decoupled from the action of the primary fast hologram due to electrons. One way, which is used here, is to uniformly illuminate the crystal.

Since the decay time of the fast one is much smaller than the decay time of the secondary grating, after a short time, only the contribution of the slowly decaying secondary grating is present (revealing phase).

The dynamics of the erasure process can be found by setting the modulation index, m, of the illuminating light equal to zero. The

resulting expressions for the amplitudes of the two charge distributions are

$$N_{er}^{+}(t) = -\frac{a_1 + B_2}{A_2} Q_1 e^{a_1 t} - \frac{a_2 + B_1}{A_2} Q_2 e^{a_2 t} \tag{4.17}$$

$$P_{er}^{+}(t) = Q_1 e^{a_1 t} + Q_2 e^{a_2 t} \tag{4.18}$$

where

$$Q_1 = -\frac{A_2 N_{er}^{+}(0) + (a_2 + B_2) P_{er}^{+}(0)}{a_1 - a_2} \tag{4.19}$$

$$Q_2 = \frac{A_2 N_{er}^{+}(0) + (a_1 + B_2) P_{er}^{+}(0)}{a_1 - a_2}$$

$N_{er}^{+}(0)$ and $P_{er}^{+}(0)$ are the amplitudes of the two charge distributions at the start of erasure. The above equations are valid for observations following the start of erasure, i.e. after the crystal is illuminated uniformly. The coupling of the two gratings is still present during the erasure process as was the case with the recording process. This is evident from the dependence of each grating on both time constants. However, for electron dominant transport, the electron- formed grating decays much faster than the hole-formed one, and after a very short time the only sizable contribution to the total grating comes from the

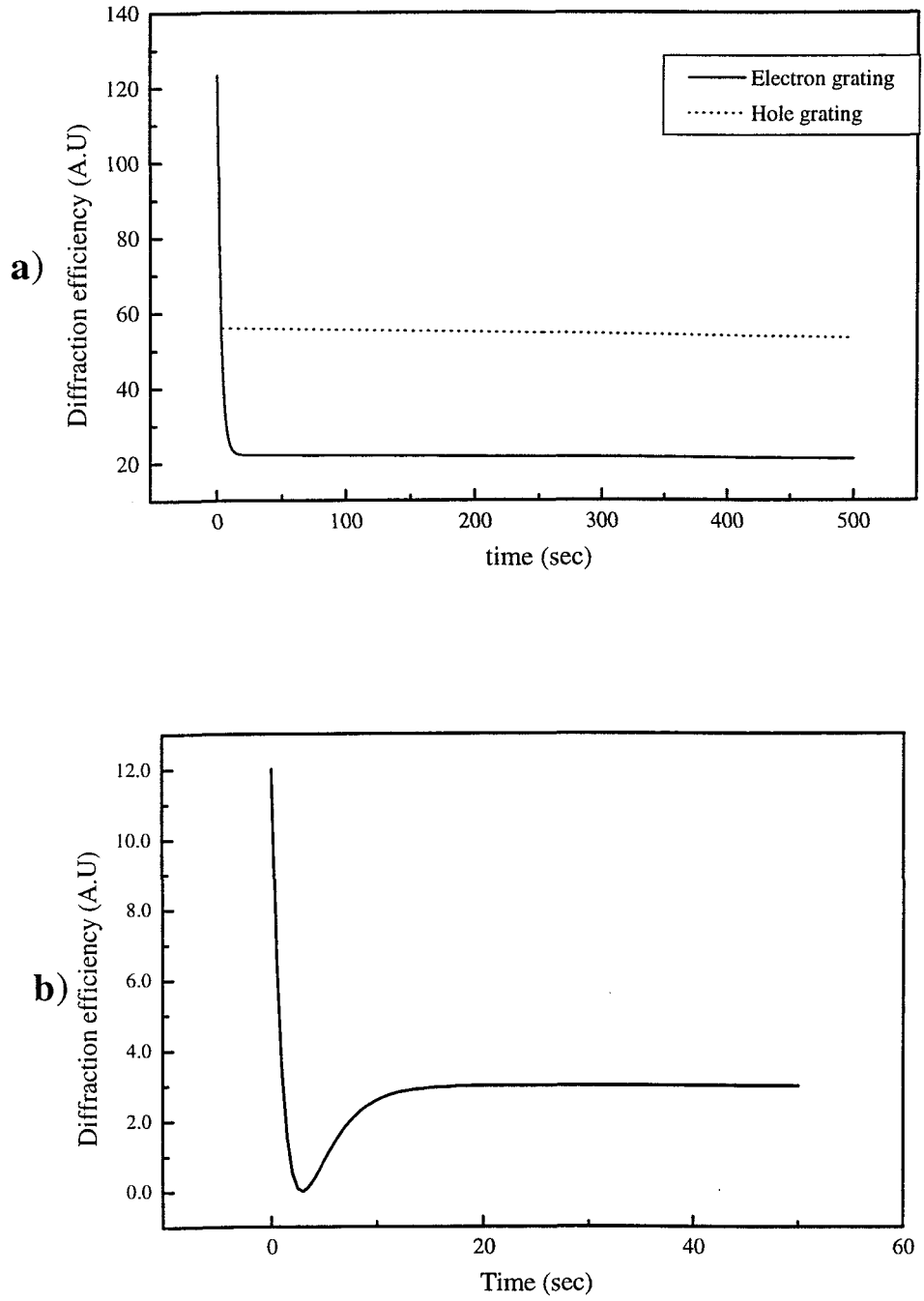

Figure 4.6 a) Theoretical curve of the evolution of the electron grating (solid line) and the hole grating (dot line), during erasure, b) The resulting diffraction efficiency from the two gratings as a function of time. The parameters used for the curve calculation are: $\Lambda=1\mu m$, $E_0=0$ KV/cm, $N_{eff1}=2x10^{21}m^{-3}$, $N_{eff2}=1.2x10^{25}m^{-3}$, $L_{Dn}=1.7x10^{-5}m$, $L_{Dp}=2.7x10^{-7}m$, $\tau_{mn}=5.8x10^{-4}sec$, $\tau_{mp}=1570sec$. The start of the erasure corresponds to the end of the recording stage (t=1000sec).

slow one. Figure 4.6 (a) depicts theoretical results for the time evolution of the two gratings after the start of erasure.

The grating period is assumed to be 1μm and no electric field is applied. The primary grating decays quickly, while the secondary one is erased at a much slower rate. It must be noted here that the individual decay curves deviate from the simple exponential form due to the strong coupling between the two gratings as shown in Figure 4.6 (a). For very strong applied electric fields this coupling weakens and the two gratings decay exponentially[86].

The temporal behavior of the diffraction efficiency, η, of the total grating during erasure, is found by recalling that η is proportional to the square of the electric space charge field which in turn is proportional to the difference between the amplitudes of the two charge distributions. Figure 4.6 (b) shows the whole revelation process of the semi-permanent hologram. During the first phase the primary grating, which initially is stronger, decays fast until its amplitude becomes exactly equal to the amplitude of the slow grating. During this time the efficiency decreases. At the moment of exact grating compensation the electric space charge field changes sign (equivalently the diffraction efficiency falls to zero) and subsequently the efficiency increases until it reaches a maximum. At this point the contribution of the electron-formed grating may not be exactly zero. Finally, the net efficiency, being proportional to the difference of the two gratings, slowly decays

to zero with a rate essentially equal to the one associated with the secondary grating.

4.5 A holographic method for the determination of fundamental PR parameters.

4.5.1 Description of the method

The above described model can be used for the determination of the three main photorefractive parameters, N_{eff}, L_D, and $\tau_{m(n,p)}$ for both types of charge carriers as well as other materials parameters with as few assumptions as possible. It can also be applied to any photorefractive material exhibiting a dual recording behavior. In order to compare theoretical results with the experiment it is useful to use a quantity that does not depend upon initial conditions (i.e the initial amplitudes of the gratings just before erasure) which can vary from one recording to the other, due to factors that cannot be controlled such as random vibrations.

The quantity $\eta(t+t_1)/\eta(t_1)$ where:

$$\eta(t) = \left| \frac{ie}{\varepsilon_0 \varepsilon_r K} (P_{er}^{+}(t) - N_{er}^{+}(t)) \right|^2 \qquad (4.20)$$

is a normalized to unity decaying function of time. The decay rate depends only on the material parameters through the quantities a_1 and a_2. This is a suitable quantity to be fitted against the experimental data

and yield the three photorefractive parameters without the knowledge of any other material parameter.

Setting $t=t_0$, the beginning of the erasure at t=0, the time instant $t=t_1$ at which the maximum value of the diffraction efficiency occurs is:

$$t_1 = t_0 + \frac{1}{a_1 - a_2} \ln \frac{a_2}{a_1} \tag{4.21}$$

and the time instant, at which the two gratings become equal (minimum of the diffraction efficiency) is:

$$t_0 = \frac{1}{a_1 - a_2} \ln\left(-\frac{\Theta_2(A_2 + B_2 + a_2)}{\Theta_1(A_2 + B_2 + a_1)}\right) \tag{4.22}$$

The decay of the overall grating was monitored using the experimental setup described in Figure 4.1 . s-polarized recording and readout beams are used. The intensities of the recording beams were I_S=64 mW/cm^2 and I_P=83mW/cm^2 for the signal and pump beam respectively and I_R=20mW/cm^2 for the readout beam. The crystal was preilluminated for 30sec with the HeCd beam (442 nm) of intensity 40mW/cm^2. The recording beams were turned on and the recording procedure proceeds until saturation is obtained (about 8 minutes for the fringe spacing used). The real time monitoring of the development of the recorded grating was possible with the setup used because the readout beam is present at all times. At this point the recording beams

a)

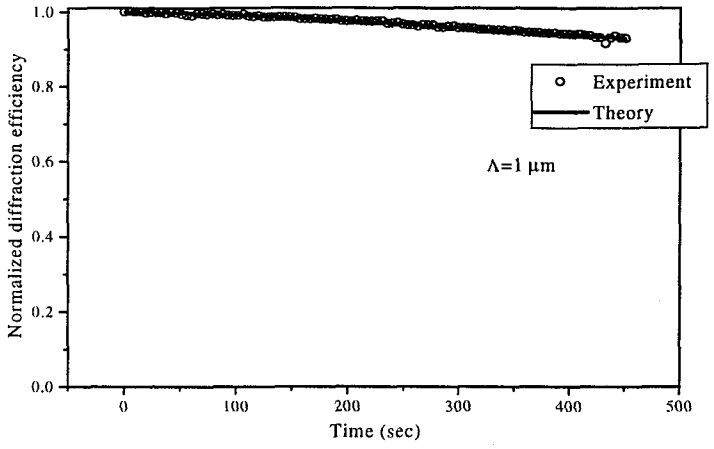

b)

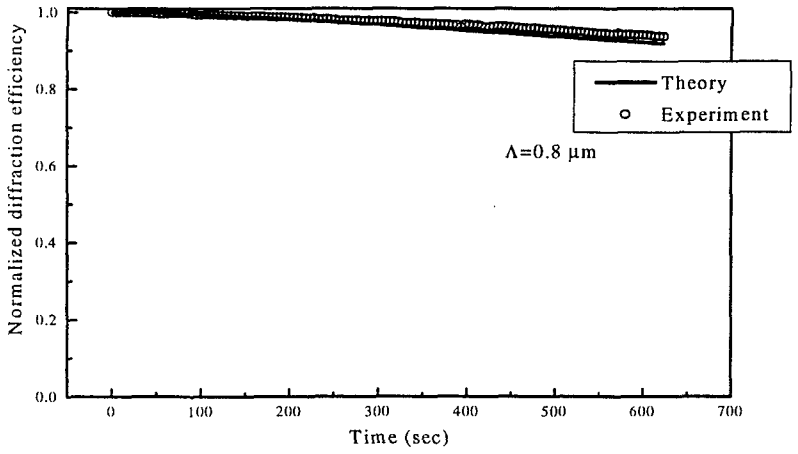

c)

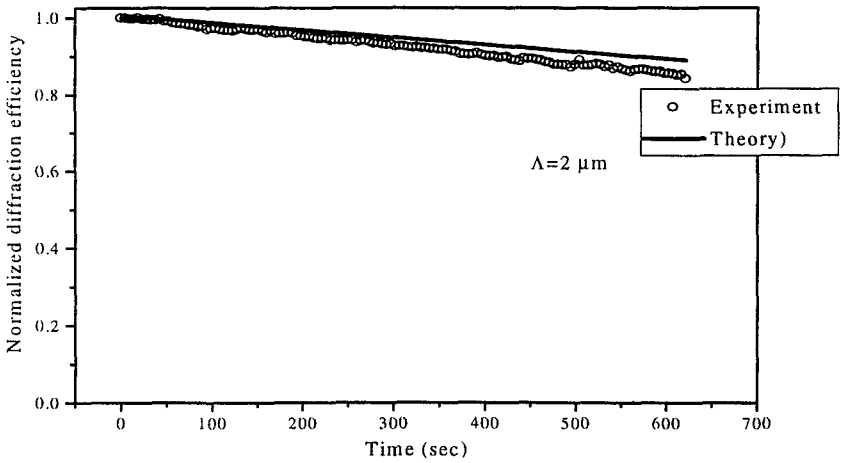

Figure 4.7 .Decay of the overall grating for a)Λ=1 μm, b) Λ=0.8 μm and c) Λ=2 μm fringe spacing. Comparison of experimental data points (open circles) with theoretical curves (solid line).

	N_{eff1} (m^{-3})	N_{eff2} (m^{-3})	L_{Dn} (μm)	L_{Dp} (μm)	τ_m^n I_R (mJ/cm^2)	τ_m^p I_R (mJ/cm^2)
Present method	$2x10^{21}$	$1.2x10^{25}$	97	0.27	0.012	$3.14x10^{4}$
Mullen et al.[95]	10^{22}		4		0.0016	
Pauliat et al. [96]	$7.7x10^{21}$		3.4		0.0018	
Peltier et al. [97]	10^{22}		2.1			
Huignard et al.[98]	$2x10^{22}$		0.6		0.068	
Grousson et al. [99]			3.6			
Huignard et al. [100]	10^{21}					

Table 4.1 Values of the photorefractive parameters of BSO, related to both types of charge carriers, found by fitting the experimental decay of the overall grating with theory. The values of the same parameters (related to electrons) found by other methods are also presented.

were blocked and the readout beam monitors the decay of the overall grating. The fringe spacing was 1 μm.

The quantity $\eta(t+t_1)/\eta(t_1)$ was fitted to the experimental data for the decay of the overall grating. The Nelder-Meade simplex algorithm[101] was used for the fitting process. The best fit values for the PR parameters are presented in Table 4.1 and they are compared with values found in the literature for only one charge carrier (electrons). The solid curve in Figure 4.7 (a) corresponds to the theoretical results based on the estimated PR parameters while the observed experimental behavior is described by the solid circles. In order to check the consistency of the model two more experiments were performed using different fringe spacing values of Λ=0.8 μm and Λ=2μm Figure 4.7 (b) and (c) show the comparison between experimental and theoretical results obtained using the above estimated set of PR parameters.

4.5.2 Discussion

The estimated value for the N_{eff1} (electrons) is $2x10^{21}$ m^{-3} and it is 5 times smaller than the values met in the literature. This is attributed to the preillumination with the HeCd radiation for 30 seconds. This causes excitation from the hole producing traps (and the valence band) to the electron producing traps (and the conduction band) and therefore, an increased number of filled electron traps and empty hole traps, which also explains the larger value of N_{eff2} compared to N_{eff1}.

There is experimental verification, which will be shown later, that prior illumination with blue light causes an increase of the effective trap density for holes and a decrease of the effective trap density for electrons.

The increased number of filled electron traps also explains the one order of magnitude larger value of the electron diffusion length (L_{Dn}=9.7x10^{-5} m) estimated here, compared to the values found in the literature (Table 4.1). The diffusion length associated with holes however is relatively small (L_{Dp}=2.7x10^{-7}m), since there are less filled hole centers and therefore the average distance of a free hole before trapping is relatively smaller.

The estimated relaxation time, $\tau_{mn}I_R$=0.012mJ/cm^2, is larger than most values found in the literature. Here also the effect of the HeCd laser pre-illumination on the absorption coefficient and therefore the photoexcitation cross section may explain this difference.

Further evaluation of the used model can be derived by comparing the results for a_1 and a_2 as a function of the fringe spacing with experimental results found in the literature. These are the individual grating decay coefficients and they depend upon both electron and hole related parameters. In Figure 4.8 (a) and (b) are depicted plots of the a_1 and a_2 values respectively versus the fringe spacing of the recording interference pattern.

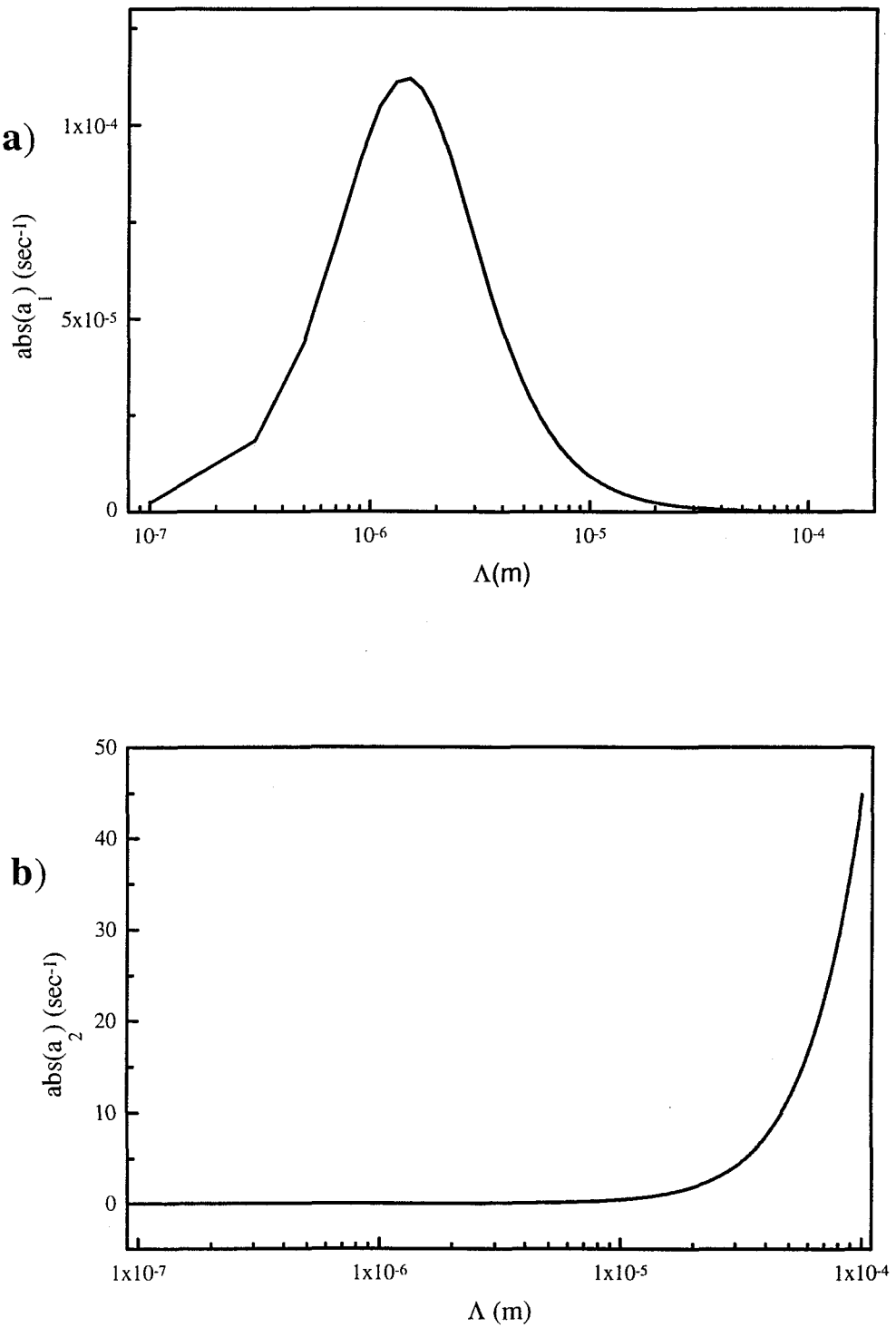

Figure 4.8 Fringe spacing dependence of the a) a_1 and b) a_2 parameters. The curves were calculated from equation (4.10) using the materials parameters found from the fitting process.

The obtained curves are derived by equations (4.7)-(4.10) using the values for the six PR parameters estimated by the fitting process. It is observed that a_1 is much larger than a_2 indicating that a_1 is the decay rate of the hole grating which is expected to have a much slower response. Similar behavior has been observed by G. Montemezzani *et al*[102] for $KNbO_3$ due to ionic charges.

For small Λ ($K\rightarrow\infty$), $A_2\rightarrow 0$ and $B_2\rightarrow 0$, and therefore, $|a_1|\rightarrow B_2\rightarrow(l_{Dp}/L_{Dp})^2/\tau_{mp}$, where l_{Dp} is the Debye screening length for holes given by:

$$l_{Dp}^2 = \frac{\varepsilon_r \varepsilon_0}{e^2}\frac{k_\beta T}{N_{eff2}} \qquad (4.23)$$

Substitution of the fitted values in the above equation yields $|a_1|\rightarrow 5.66\times10^{-8}$ sec^{-1}.

This value represents the dielectric limit and it is the same for all recording regimes with or without the application of external electric field. Finally it must be noted that the decrease of $|a_1|$ in the submicron regime observed in Figure 4.8 (a) agrees with the experimental behavior shown in Figure 4.4 where an increase of the decay rate, with increasing Λ, is observed for submicron fringe spacing.

4.5.3 HeCd laser preillumination

In the previous sections it was mentioned that prior illumination with blue light affects the characteristics for both electron and hole grating

recording due to the redistribution of effective trap densities. This is attributed to cross excitations between electron and hole trapping levels. In this section the effect of prior illumination is studied, using the above described model.

The decay of the overall grating during the erasure stage was fitted against the theory for increasing HeCd exposure times and the corresponding effective trap densities were estimated for each case.

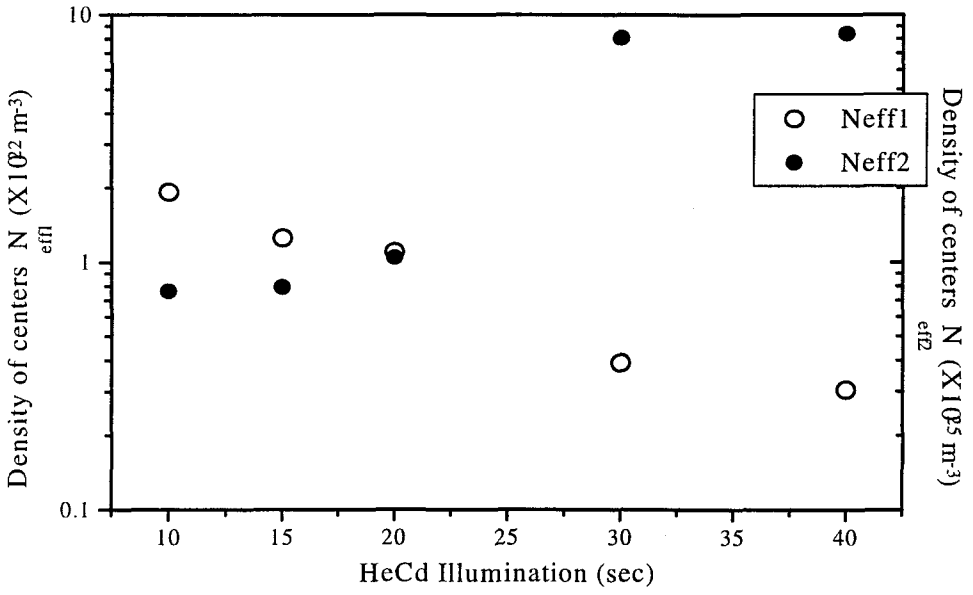

Figure 4.9 Dependence of the effective trap densities N_{eff1} and N_{eff2} of the electron and hole transport systems on prior illumination of the BSO crystal with HeCd light (442 nm) of intensity of 40 mW/cm^2.

The results are depicted in Figure 4.9 where the effective trap densities N_{eff1} and N_{eff2} associated with electron and holes respectively are plotted against HeCd exposure time. A change of the relative

occupation of the two different types of levels is observed due to HeCd illumination.

The exact transitions are not known but the results depicted in Figure 4.9 provide a strong indication that the number of empty states, N_0^+ of the electron transport system decreases, while at the same time the density, P_0^+, of the hole transport system increases.

This photoinduced phenomenon seems to reach a saturation after a certain illumination time interval at the intensities used.

4.6 Applications.

4.6.4 Image addition and subtraction.

By utilizing the dual temporal recording behavior of the crystal as well as the already existing shift between the two recorded gratings it is possible to perform image synthesis and logic operations[103,104]. The slow response of the semipermanent photorefractive recording allows the real time image addition and subtraction of images.

Image addition and subtraction is performed by multiplexing in the same crystal volume real-time and semipermanent mutually phase shifted holograms carrying different images/information in a four-wave-mixing arrangement. During recording, image subtraction occurs spontaneously due to the inherent phase shift between the two

gratings. If an additional phase shift is introduced in one of the writing beams then image addition can be achieved. The operation lasts as long as the decay time of the semipermanent grating and there are no synchronization requirements as in ref. 103.

Addition and subtraction of bright horizontal and vertical bar chart images is depicted in Figure 4.10 . In a binary mode the above represents operations such as, for example, XOR and OR and those may be realized for all image elements in parallel.

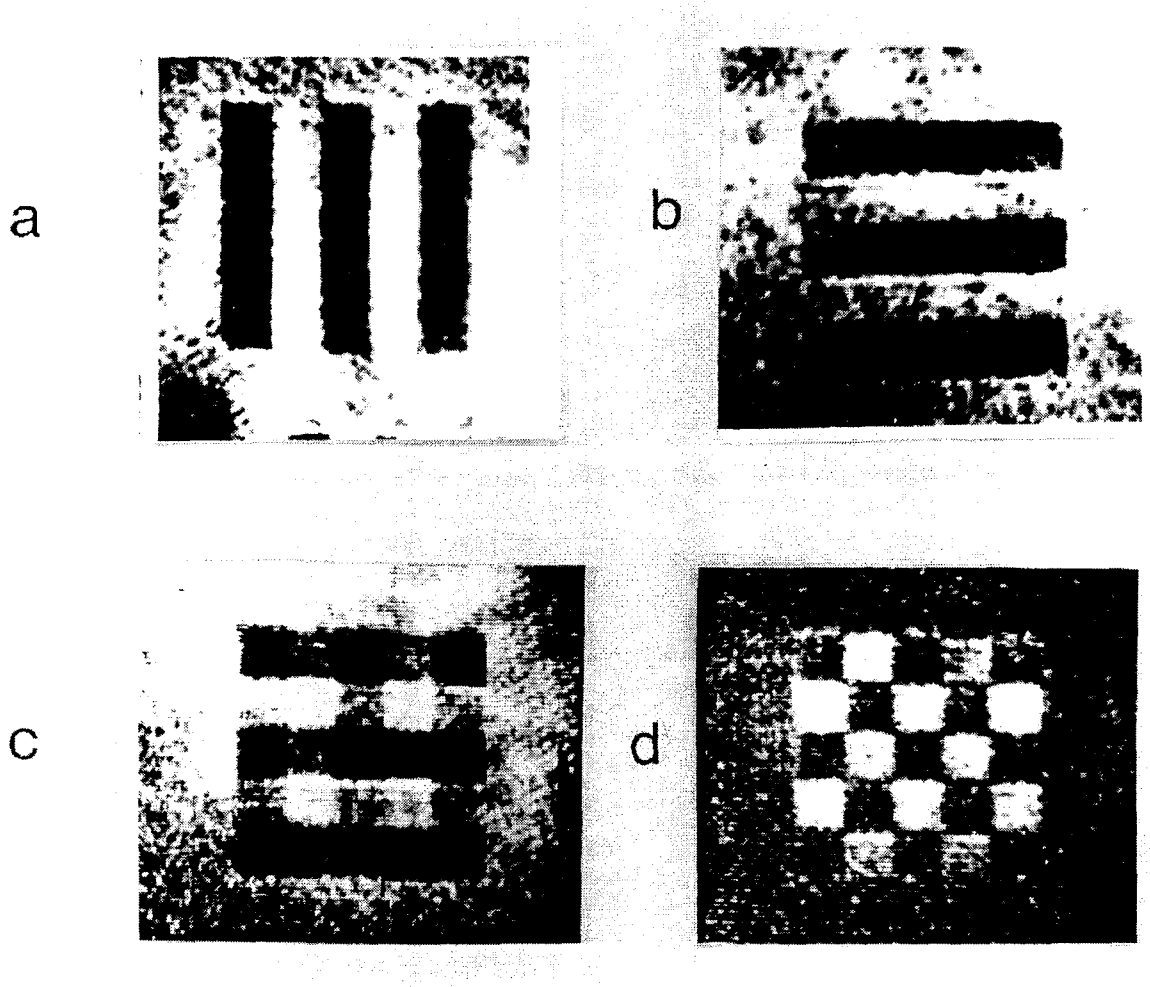

Figure 4.10 Pictures of input images (a) and (b) and their addition (c) and subtraction (d), achieved by superposition of fast and slow holograms in the same crystal volume.

4.6.5 Spatial Optical Sensitization-Incoherent to Coherent Information Transfer

Crystal preillumination with blue light leads to the enhancement of semipermanent recording as it has been discussed in previous sections. In respect, with the crystal illuminated by a spatially modulated incoherent beam a spatially selective sensitization of the recording volume can be achieved. In the blue-illuminated areas, the observed semipermanent recording is much more efficient than in the dark areas, for the same recording conditions.

Using this particular property in photorefractive recording, incoherent-to-coherent information transfer can be performed in two distinct operation modes. Such operation is extremely useful in coherent processing input devices for spatial light modulation.

The first, preillumination, mode relates to the spatial sensitization of the crystal which selectively enhances the recorded grating. Second, in the post-illumination mode selective erasure of a uniform semipermanent grating previously recorded in the crystal is used. In both cases information in a two-dimensional image format is transferred from the blue "incoherent" beam to the near infra-red coherent output. Incoherent-to-coherent information transfer have been realized with dynamic photorefractive recording[105] in the visible region under the application of high electric fields. In addition, diffraction efficiency enhancement effects[106] have been observed in

photochromic gratings, but they have been attributed to the modification (decrease) of the strength of "parasitic" photorefractive gratings associated with the primary permanent photochromic gratings. Both the above schemes are distinctly different in nature than our case in which sensitization occurs due to activation of additional centers. In the preilluminated area enhancement of the semipermanent recording occurs. As a result, the diffraction efficiency of the overall grating, recorded in the preilluminated area, is poorer than in the surrounding area because a strong semipermanent grating is now present, together with the dynamic one, which is π-shifted. This leads to destructive interference of light diffracted off the two gratings. For this reason, a dark replica of the projected image appears immediately after the erasure procedure starts. This reverses in contrast during the revelation of the semipermanent grating thus producing a bright replica of the projected image. This sequence of events is shown in Figure 4.11 (a), (b).

In the second mode (selective erasure), the projected image selectively erases the uniform hologram of the beam producing a dark replica of the projected image (Figure 4.11 c).

For the realization of the above a simple hologram recording arrangement has been used. Following semipermanent recording, one of the two participating beams is turned off and the other is used for reconstructing the recorded hologram as it has been spatially

modulated by the incoherent beam Figure 4.11 (c). Various combinations of the two operation modes have been realized, producing a plethora of interesting effects.

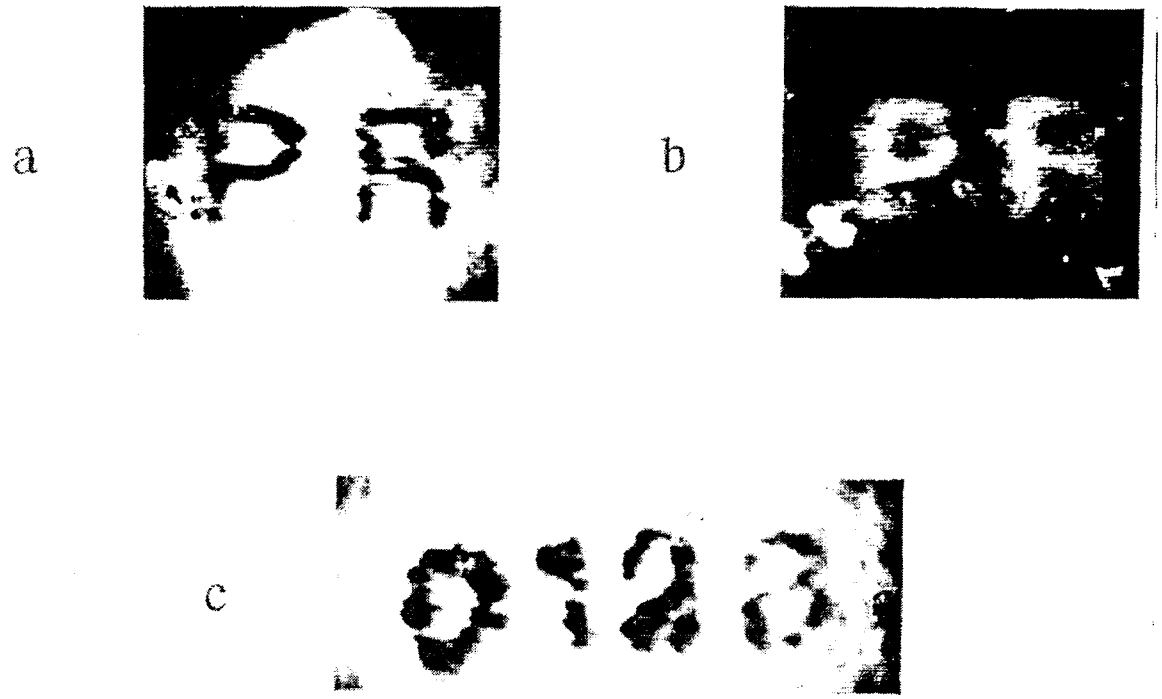

Figure 4.11 Example of incoherent to coherent image transfer. a) Reconstruction of the hologram recorded in the preilluminated area immediately after the start of the erasure, b) revelation of the enhanced semipermanent recording and c) selective erasure of a semipermanent grating formed by two single beams.

4.7 Conclusions.

Semipermanent photorefractive recording of holograms, exhibiting very long lifetime, by using near infrared radiation is achieved in BSO crystals simultaneously with the usual dynamic recording. Neither special fixing techniques nor an external electric field are applied for the revelation of these holograms. Experimental investigation of the properties of these semipermanent holograms is presented, and a

model is incorporated to explain the experimental results. This model is suitably modified and a method for the determination of important photorefractive parameters has been developed. Dynamic and semipermanent photorefractive holograms, multiplexed in the same crystal volume, may be used for image processing applications and examples are presented. Illumination with blue light enhances semipermanent recording characteristics and this effect is used to achieve spatial sensitization of the material, thus leading to various incoherent-to-coherent information transfer operations.

Chapter 5

HOLOGRAPHIC RECORDING IN INDIUM OXIDE (In_2O_3) AND INDIUM TIN OXIDE (In_2O_3:Sn) THIN FILMS

5.1 Introduction

In_2O_3 (InO_x) and In_2O_3:Sn (ITO) films are very well investigated materials due to their interesting electrical and optical properties and their suitability for potential technological applications. Thin films of the above material, grown by various methods[107], as discussed in chapter 1, may be transparent in the visible and near infrared region of the electromagnetic spectrum while their electrical state can be either conductive or insulating. Due to their good conductivity and extended transparency, as well as their relatively high refractive index[108] (n > 1.8) and good adhesion and structural properties, InO_x and ITO films have been used as conductive transparent optical coatings in electro-optic devices[31].

The conductivity of polycrystalline InO_x and ITO films can be modified upon illumination with ultraviolet (UV) radiation (hv>3.5 eV), resulting in a variable electrical state of the films from resistive to a purely conductive[34]. Such effects have also been verified recently[109] at very low temperatures (4.2°K), at which diffusion effects are inhibited.

In this chapter dynamic changes of the refractive index and/or absorption coefficient of InO_x and ITO thin films, grown by DC sputtering, and InO_x films, under exposure to UV radiation which leads to the formation of real time holographic gratings, are investigated. The observed grating recording appears to be independent of the electrical state of the film (insulating or conducting), and exhibits a slow but dynamic behavior. The recorded hologram decays exponentially in the absence of UV light with a characteristic time that depends on the material's specific properties. Such effects are distinctly different from permanent changes of the optical absorption of ITO films, upon irradiation with visible light, which have been attributed to conductivity changes of the films[110].

5.2 DC-Magnetron Sputtering grown thin films

5.2.1 Experiments and results

Several thin films were deposited on glass substrates by DC magnetron sputtering in a mixture of argon-oxygen plasma at a total pressure of $8x10^{-3}$ mbar using a 99.999 % pure indium target. The thickness of the films was in the range of 250nm to 1000nm. A typical holographic setup, shown in Figure 5.1, was used. The beam of a HeCd laser emitting at λ= 325 nm was divided into two mutually coherent beams, by means of a dielectric beam splitter. The two beams, R_1 and R_2, with intensities of 300mW/cm^2 each, were subsequently directed onto the

sample, forming an intensity interference pattern. Numerous recordings at various fringe spacing values (Λ) have been studied.

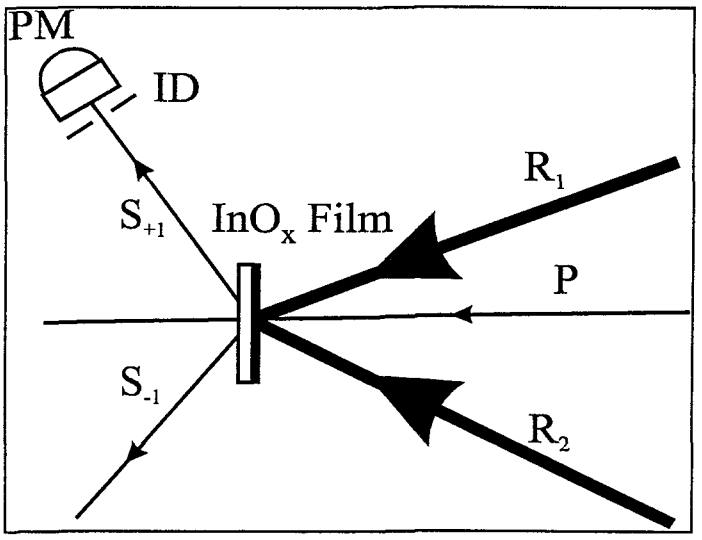

Figure 5.1 Schematic of the experimental setup used for holographic recording. R_1, R_2 : recording beams at 325 nm, P : HeNe probe beam at 633 nm, $S_{\pm1}$: Diffracted HeNe beam, PM : Power meter head, ID : Iris diaphragm.

A HeNe laser beam was used to monitor the recording of the holographic grating. The 5.7 mW HeNe probe beam, P, was incident normally onto the surface of the film. Two scattered beams, $S_{\pm1}$, of equal intensity were observed corresponding to the ±1 diffraction orders of the recorded sinusoidal grating. One of the two diffracted beams was monitored, by using an optical power meter and a storage oscilloscope, in order to investigate the temporal characteristics of the recorded gratings.

A typical sequence of holographic grating recording and decay in InO_x and ITO films is depicted in Figure 5.2 (a) and (b), respectively.

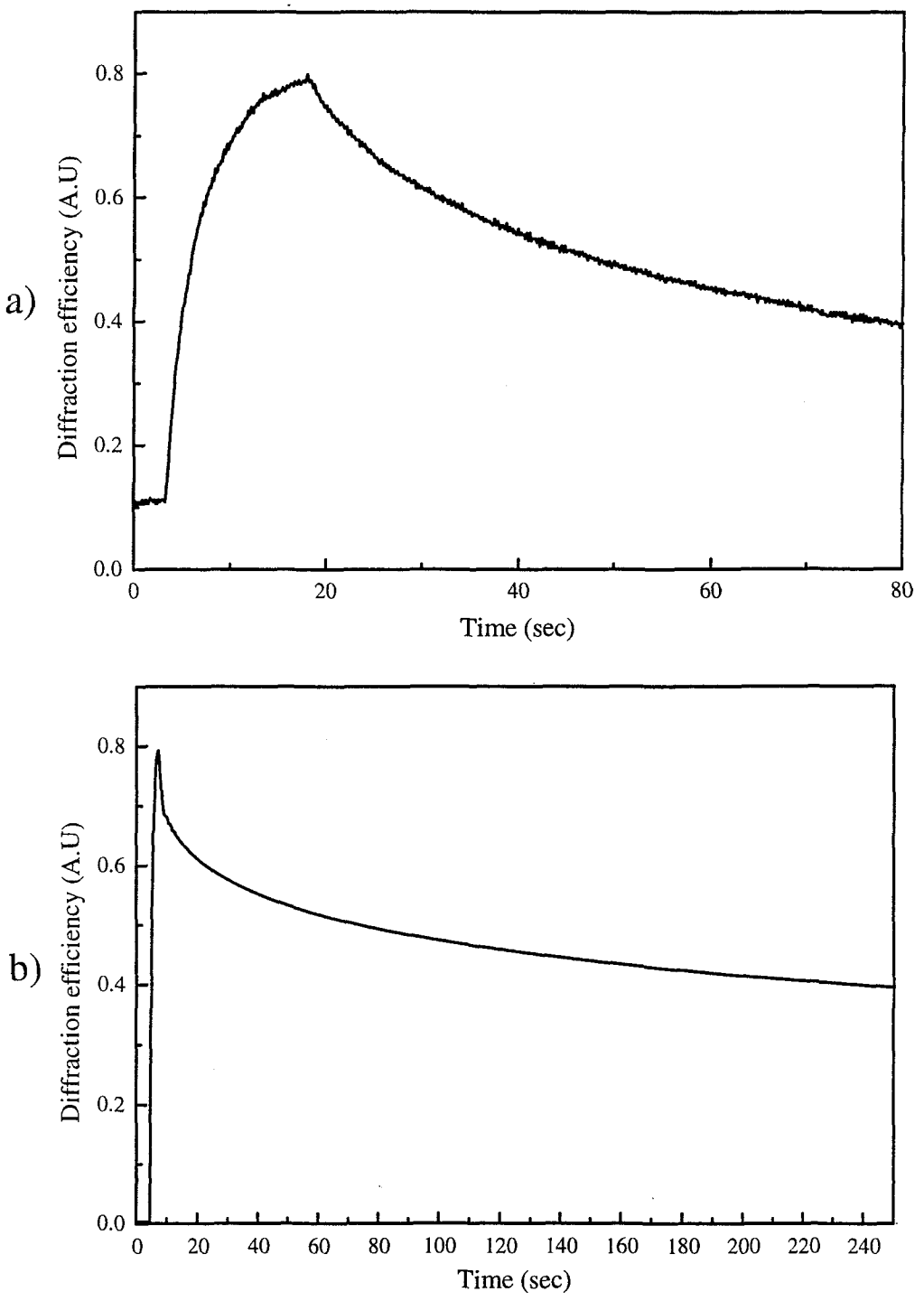

Figure 5.2 Temporal behavior of holographic recording of gratings in InO_x film (a), and ITO film (b).

A maximum diffraction efficiency of $\eta=2.5x10^{-5}$ is observed for a grating recorded in a 270 nm thick InO_x film. Assuming that a pure phase grating was recorded, a coupling coefficient value of 190 cm^{-1} can be estimated. In the rising part of the trace, all three (recording and probe) beams are present, while the decay is observed in the absence of both recording beams. The HeNe beam is always present to probe the evolution of the grating being recorded. It was observed that the probe beam does not affect the recording characteristics which are solely associated with UV radiation. No darkening or coloration of the film was observed nevertheless, the existence of an absorption component of the grating cannot be excluded.

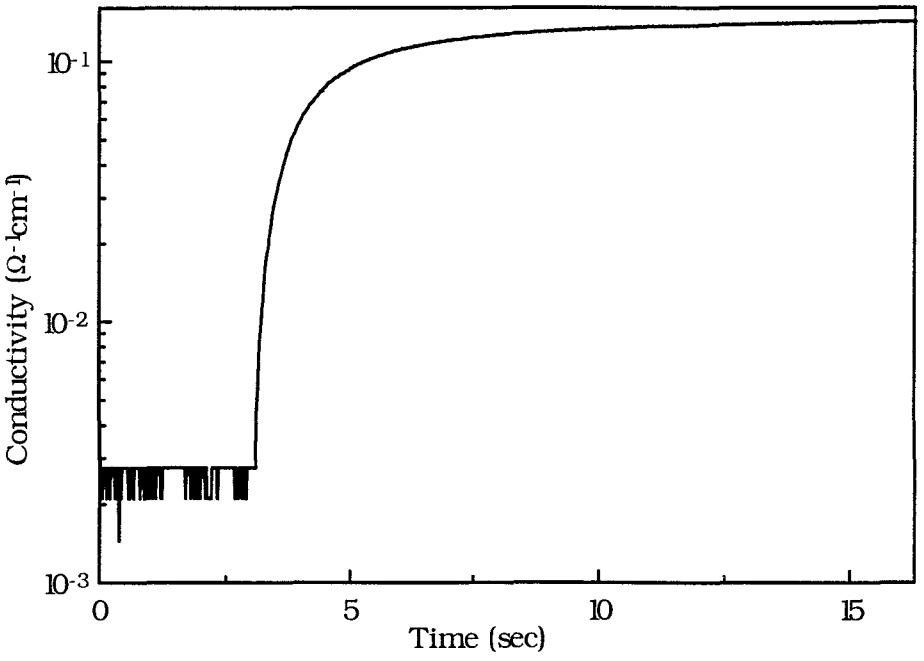

Figure 5.3 Change of the conductivity of an InO_x film under uniform UV laser illumination of constant intensity.

Illumination with UV light in air increases the conductivity of a InO_x film by 2 orders of magnitude.

Figure 5.3 depicts the absolute change of conductivity of InO_x film of thickness d=270 nm, upon illumination with a HeCd laser beam of intensity I=2.8 mW/cm^2. The new electrical state of the film is maintained until the film is exposed to an ozone atmosphere.

Holographic recording is observed in both insulating and conducting states of the same film and both recordings exhibit similar diffraction efficiency values. The above mentioned experimental results suggest that optically induced conductivity changes are not responsible for holographic recording. If that were the case, then spatial modulation of conductivity would imply a permanent recording behavior and different diffraction efficiency levels for specimens of differing conductivity. This is not observed here.

The hologram decay does not follow a simple exponential form. Double exponential decay curves fit well to the decay data, as it is shown in Figure 5.4. Time constants of τ_1=6.7sec and τ_2=48sec have been extracted from the fitting procedure. The decay time constants remain practically the same for all values of Λ in the range 0.6μm to 3μm. This is in contrast to the well known case of non-localized photorefractive materials involving charge diffusion or drift[111], verifying the localized nature of the observed effects.

A possible explanation of the origin of the observed behavior may involve active centers, such as oxygen vacancies, related to the growth

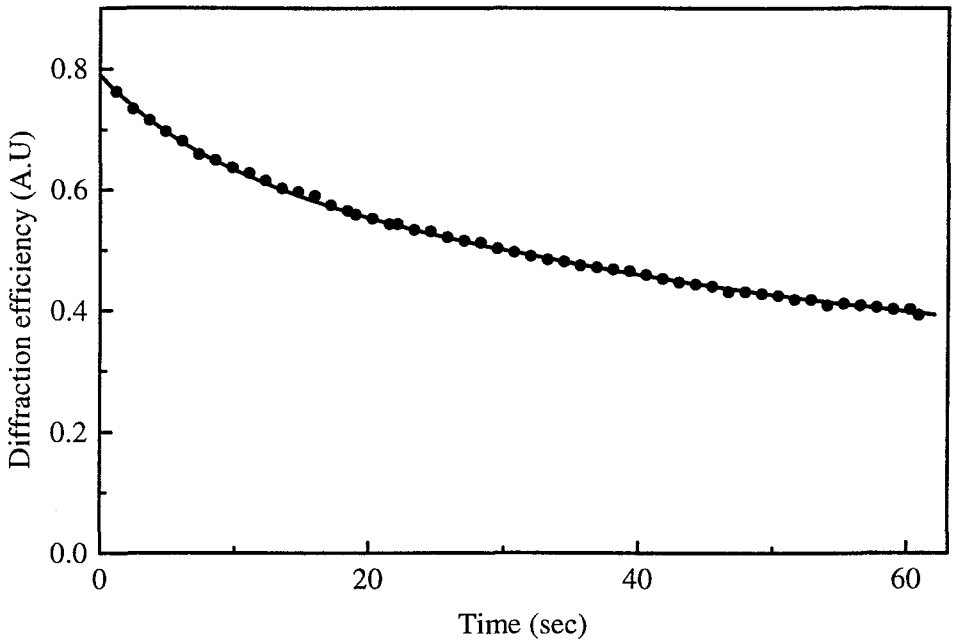

Figure 5.4 Decay in the dark of hologram recorded in InO_x film. The solid line represents the double exponential decay fitted to the decay data.

conditions and specific nature of the material. These localized states can be altered by UV radiation and their decay to the initial condition is associated with characteristic time constants that depend on the specific nature of the active centers and the material. It is verified by pulsed laser deposition experiments that growth conditions play an important role in the recording characteristics and decay time of the recorded holograms.

The above arguments may explain the difference in the observed decay behavior for gratings recorded in InO_x (τ_1=6.7 sec and τ_2=48 sec) and ITO (τ_1=14.5sec and τ_2=137.8sec). It is noted here that holographic recording measurements were performed with a large variety of

specimens. Even though they were grown during different runs of the sputtering machine, they all exhibited identical temporal behavior under the same experimental conditions.

Recording of more complicated holograms has been performed in indium oxide films. One of the UV recording beams, was modulated by passing through a resolution chart and let to interfere with a reference. A HeNe probe beam was used for the readout of the recorded hologram and the reconstructed holograms are depicted in Figure 5.5. Recording was performed in a sample ~1μm thick in order to achieve large diffraction efficiency and a bright holographic reconstruction. The observed optical noise is due to the low quality film surface. The restricted resolution of the test chart reconstruction is due to the optical system used for the projection and reconstruction of the hologram.

a)

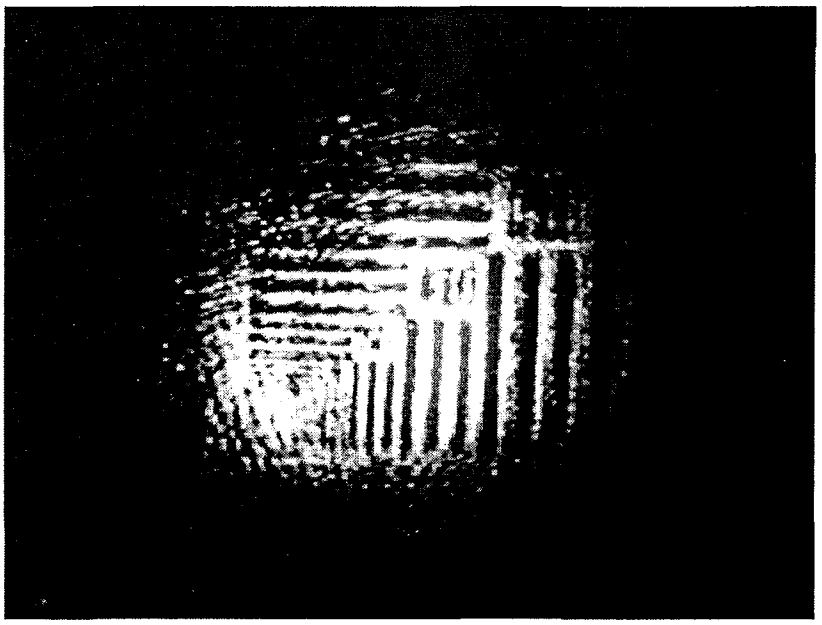

b)

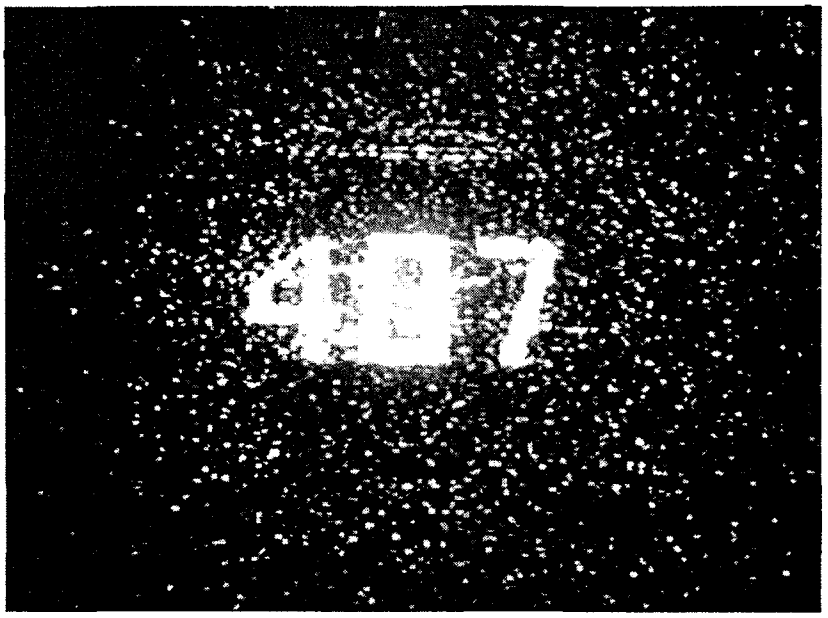

Figure 5.5 Reconstruction of holograms of a resolution chart recorded in a 1μm thick InO_x film. The numbers in a) refers to microns.

5.3 PLD grown InO_x films

5.3.1 Experimental considerations

InO_x films can also be grown by Pulsed Laser Deposition (PLD). This growth technique is extensively used for growing optical materials and its operation principle has been outlined in the corresponding part of the introduction (chapter 1.6).

For the growth of InO_x films a PLD machine was used as shown in Figure 5.6. A KrF excimer laser (delivering 20nsec pulses FWHM at 248 nm), focused by a spherical lens to yield a fluence of $2J/cm^2$ was used, in order to ablate material from a pure indium target (99.999%) in an oxygen reactive environment.

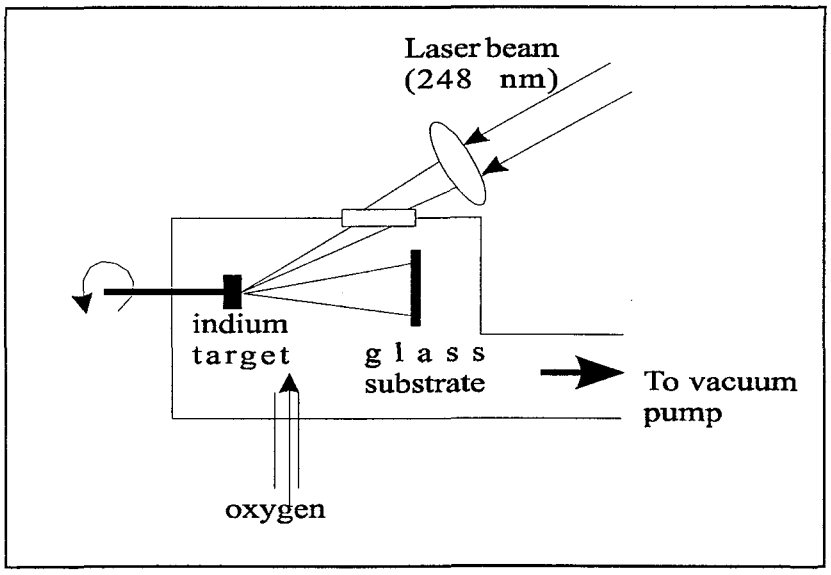

Figure 5.6 Experimental apparatus for PLD growth of InOx films.

The deposition was carried out in a stainless steel chamber with a background pressure of $5x10^{-6}$mbar. The substrate holder was rotating

for achieving uniform deposition. The reactor chamber was operated using a slow flow of molecular oxygen at pressures ranging from $2x10^{-2}$ to $4x10^{-1}$ mbar. The substrate could be heated by a pair of halogen lamps encapsulated in the substrate holder for study of the deposition at higher temperatures.

For substrate heating at temperatures over 400°C a CO_2 laser was incorporated because the indium target melted due to radiation of the lamp heat source. The InO_x films were deposited on Corning glass substrates placed at a 7cm distance from the indium target.

5.3.2 Growth parameters and thin film characterization

Several films were grown for various values of oxygen partial pressure and substrate temperature. A fixed distance (of 7cm) between substrate and indium target and a laser beam of $2J/cm^2$ are used.

Films analyzed by x-ray diffraction (XRD) exhibited a transition from the amorphous (or polycrystalline with very small grain size) phase to the crystalline phase with increasing substrate temperature. For an oxygen pressure of $5.5x10^{-2}$mbar this transition occurred at 150°C. For high oxygen pressures ~10^{-1}mbar, InO_x peaks in x-ray diffraction spectra can be observed even at room temperature.

A sequence of x-ray diffraction spectra (θ-2θ) of films grown with an oxygen partial pressure of $5.5x10^{-2}$mbar is depicted in Figure 5.7 . It can be seen that at room temperature, metallic indium dominates the

a)

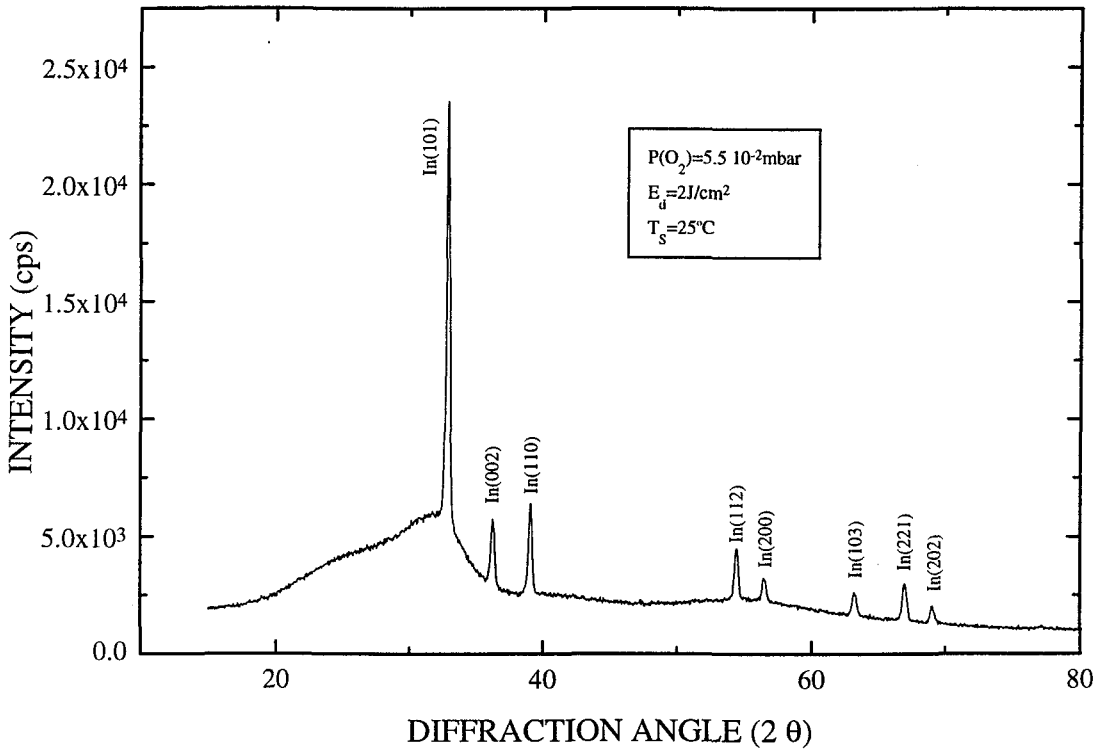
2.5x10⁴
2.0x10⁴
1.5x10⁴
1.0x10⁴
5.0x10³
0.0
INTENSITY (cps)
20
40
60
80
DIFFRACTION ANGLE (2 θ)
P(O2)=5.5 10-2mbar
Ed=2J/cm2
TS=25°C
In(101)
In(002)
In(110)
In(112)
In(200)
In(103)
In(221)
In(202)

b)

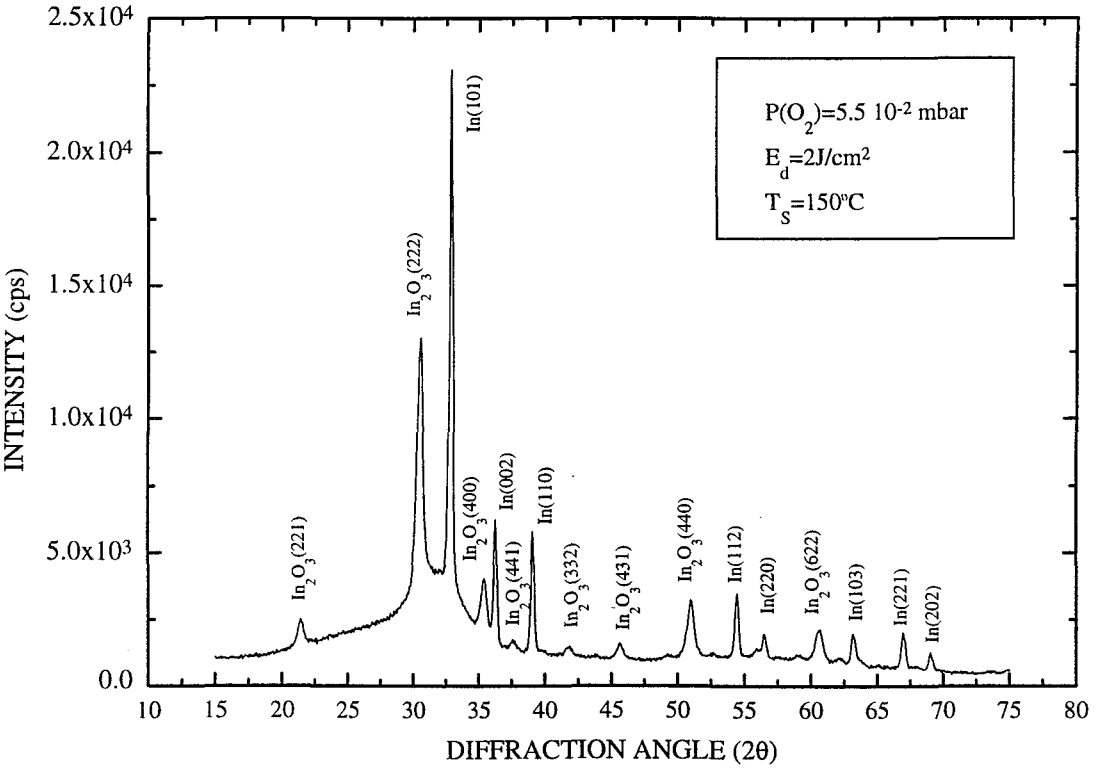
2.5x10⁴
2.0x10⁴
1.5x10⁴
1.0x10⁴
5.0x10³
0.0
INTENSITY (cps)
10
15
20
25
30
35
40
45
50
55
60
65
70
75
80
DIFFRACTION ANGLE (2θ)
P(O2)=5.5 10-2 mbar
Ed=2J/cm2
TS=150°C
In2O3(221)
In2O3(222)
In(101)
In2O3(400)
In(002)
In2O3(441)
In(110)
In2O3(332)
In2O3(431)
In2O3(440)
In(112)
In(220)
In2O3(622)
In(103)
In(221)
In(202)

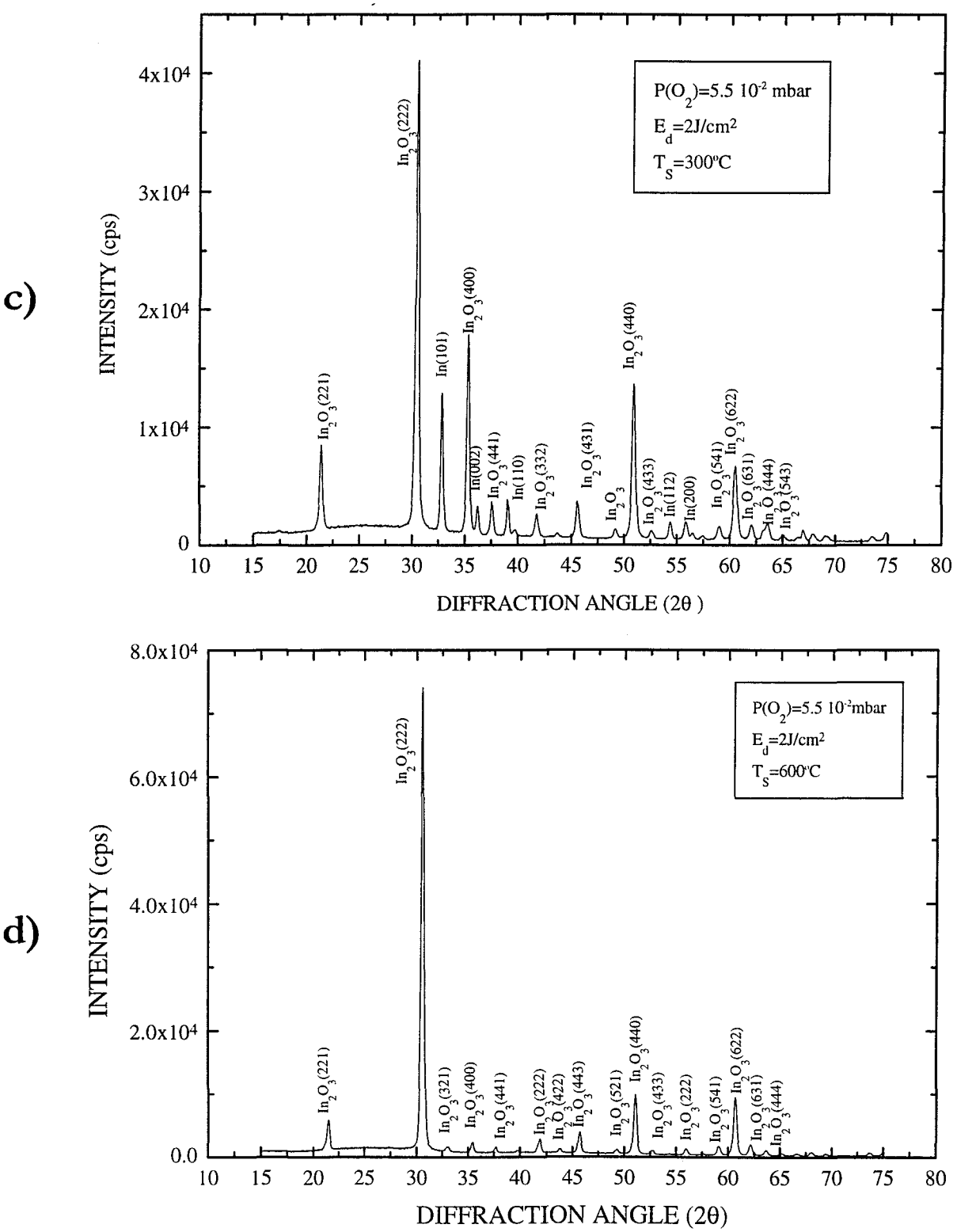

Figure 5.7 XRD spectra of InO_x films grown by PLD at various substrate temperatures.

XRD spectra. These peaks decrease and disappear at high temperatures while peaks corresponding to indium oxide crystal planes are increasing.

As evidenced in the XRD spectra pure, polycrystalline films with body-centered cubic structure and no preferential orientation were grown for oxygen partial pressure of $5.5x10^{-2}$mbar and a substrate temperature of 600°C. The lattice constant estimated by the XRD data is found $a_0=10.118\pm0.005$Å, which is in excellent agreement with $a_0=10.118$Å given in the literature, suggesting stoichiometric growth.

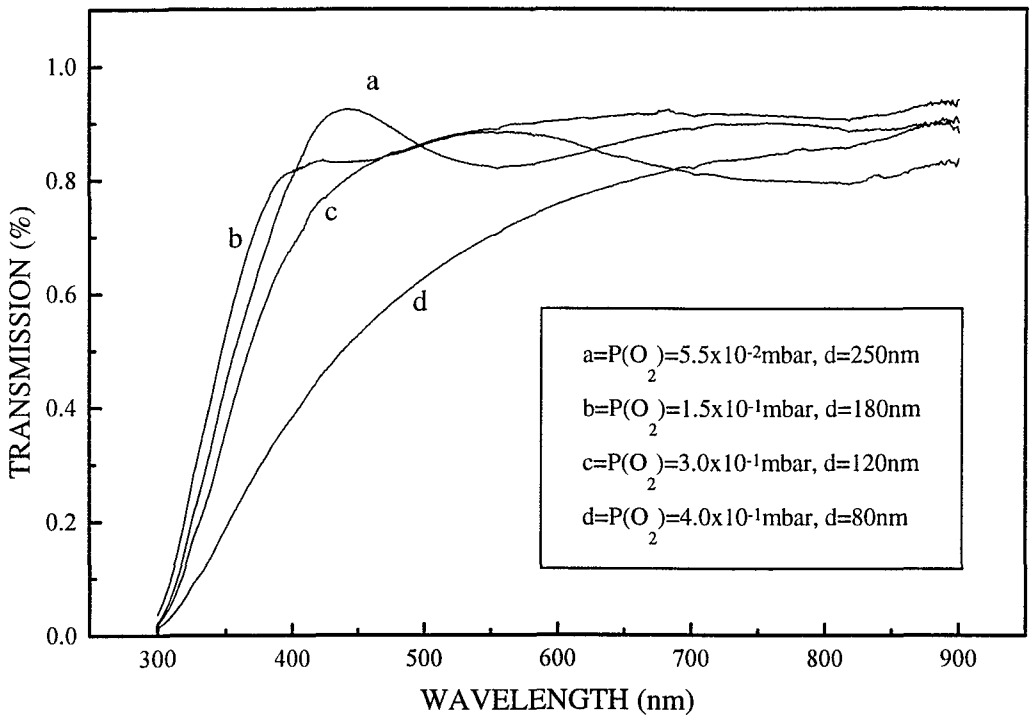

Figure 5.8 Transmission spectra of InO_x films grown at varying oxygen partial pressures.

Films grown at room temperature and oxygen partial pressure in the range of $5x10^{-2}$ to $1x10^{-1}$ mbar exhibited very good optical transmission

(approaching unity) as shown by the optical transmission spectra presented in Figure 5.8 in which the transmission of InO_x films grown at various oxygen partial pressures is depicted.

5.4 Holographic recording

For holographic recording in PLD grown indium oxide films the experimental arrangement shown in Figure 5.1 was used. In Figure 5.9 a typical recording -decay sequence is depicted. Like in the case of films grown by DC sputtering, a decay of the recorded grating is observed in the absence of UV recording beams.

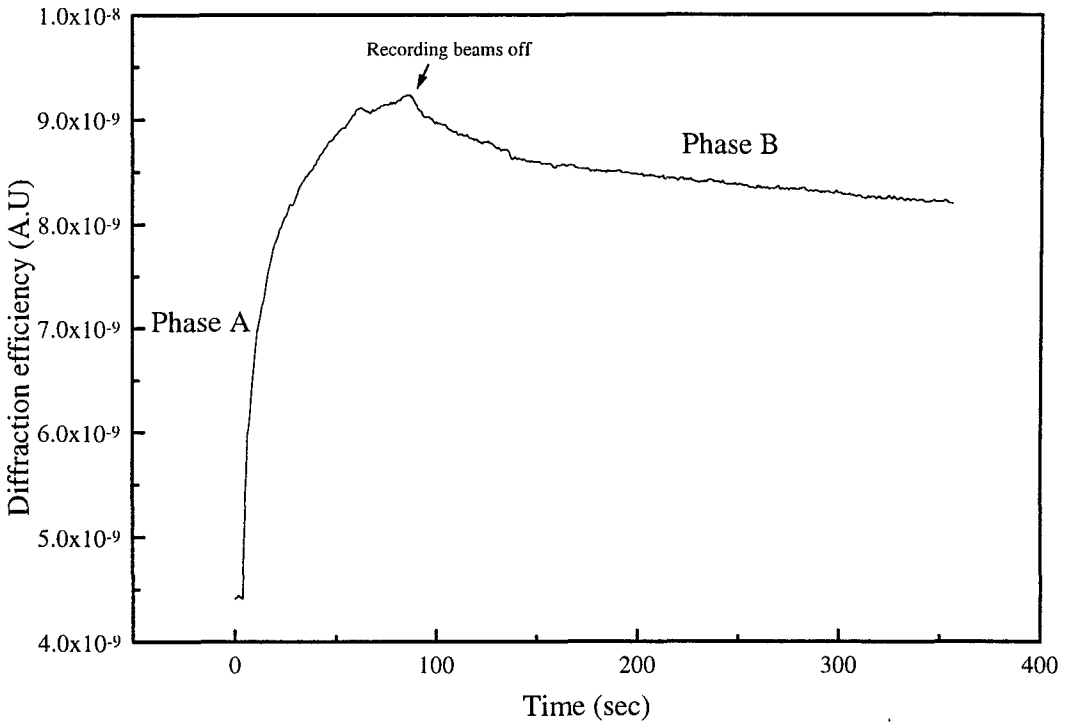

Figure 5.9 Hologram evolution in PLD grown InO_x film at room temperature. Oxygen partial pressure during growth $3.5x10^{-2}$mbar. Phase A recording, phase B decay in the dark.

The decay time, however, as well as the diffraction efficiency of the recorded gratings, varies with oxygen pressure during growth. Films grown at low oxygen pressures ~$5x10^{-2}$mbar and at room temperature presents larger diffraction efficiencies and longer decay times. Holographic recording behavior is seen to decrease as the pure polycrystalline phase is approached.

The dark decay time of the recorded gratings, extracted from a single exponential decay fitting function, is plotted against oxygen partial pressure (during growth) in Figure 5.10 . Films were grown at room temperature.

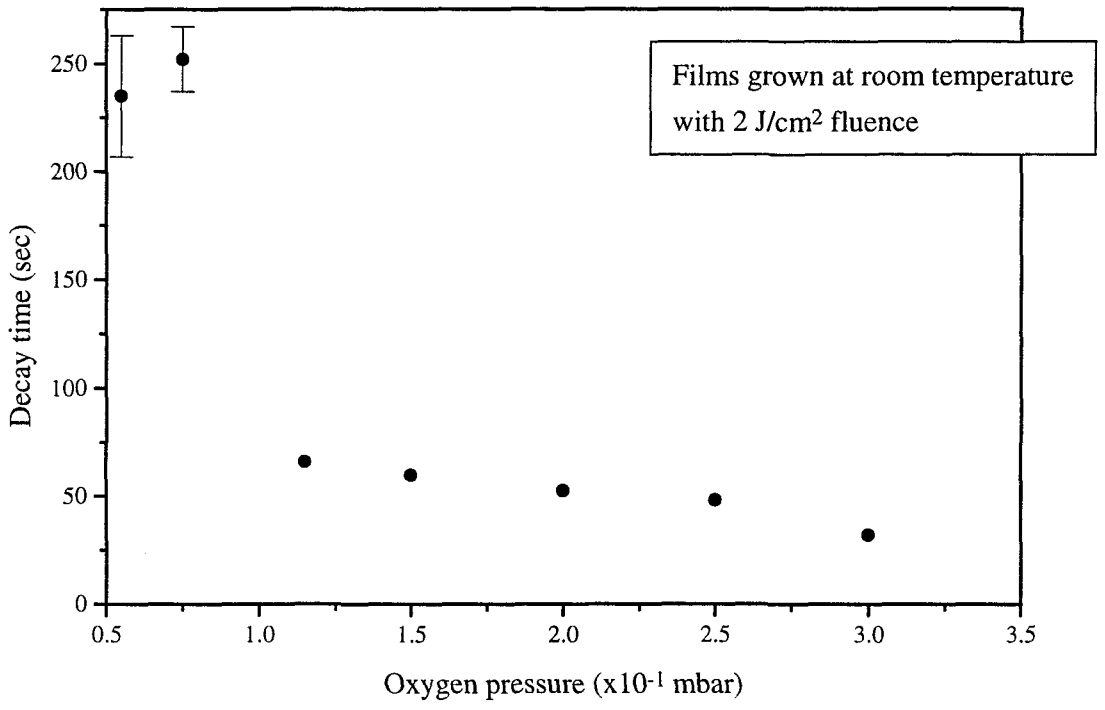

Figure 5.10 Plot of the decay time constant of gratings recorded in indium oxide films grown at different oxygen pressures as a function of oxygen partial pressure. All films are grown at room temperature.

A systematic increase of the decay time constant is observed with decreasing oxygen pressure and a peak value of τ=250sec is observed for films grown at an oxygen pressure of $7.5x10^{-2}$mbar. This exciting result indicates the potential of InO_x in optical storage applications and encourages further action.

5.5 Conclusions

Holographic recording in indium oxide and indium tin oxide transparent thin films in the ultraviolet has been observed and studied. Thin films used were grown by DC Magnetron sputtering and PLD. Growth parameters and characterization of the PLD grown films as well as the temporal characteristics of the recording in relation with growth parameters are presented. The observed holographic behavior exhibits unusually large coupling strengths. This dynamic, yet slow, behavior is seen to be associated with the localized modification of the optical properties of the material. No fatigue effects were observed and no correlation between hologram recording and the UV laser induced change of conductivity is found. The observed behavior is attributed to the existence of active centers in the material and the investigation of their nature is under progress. Most significantly, the recording characteristics can be controlled by the film growth parameters and the relatively long dark storage time observed here encourages further investigation of these alternative holographic media.

CONCLUSIONS

Optical methods are receiving great attention in telecommunications and information technology. Research now targets to optical storage, processing and transmission of information and concerns new materials, methods, components and prospective systems.

In conformity with current trends the objectives of the present work are concentrated on the investigation of materials properties, new processing methods as well as new, alternative holographic media operating in the short wavelength spectral range.

The study is, first, concerned with the fundamental behavior of photorefractive materials relating to holographic storage and processing. Materials properties are investigated and new effects are presented. Analysis of such fundamental aspects leads to a better understanding of the nature of the materials used and new optical schemes are developed for the determination of important materials parameters. Second, novel optical methods emphasizing on dynamic holographic projection, adaptive signal transmission and processing are demonstrated. Finally, alternative holographic recording materials, such as indium oxide thin polycrystalline films, are developed by pulsed laser deposition and used for dynamic holographic recording in the ultraviolet.

A novel scheme for pulse amplification of low intensity CW signals has been studied. The output of an argon ion laser, being pulse-amplified by a series of dye amplifiers, has been used to amplify a low intensity CW signal, delivered by the same CW source, by two beam coupling in a photorefractive $BaTiO_3$ crystal. The two-beam-coupling gain of almost 10^4 observed is one order of magnitude larger than the corresponding purely CW amplification gain. The system is capable of performing high-gain coherent amplification at extremely low signal intensity, in a non-mechanically stabilized environment, combining the advantages of both CW and pulsed recording configurations. The proposed method may be used for the pulsed recording and projection of moving object scenes targeting to cineholographic applications.

An adaptive signal transmission system has been demonstrated and analyzed. The system relies on a combination of two photorefractive crystals, respectively performing amplification and phase conjugation. It is capable of generating an amplified, phase modulated, phase conjugate replica of a weak unmodulated signal beam. The observed amplification performed by the system appears, so far, to be limited within a specific range of pump-to-signal beam intensity ratio, nevertheless it facilitates potential applications. Gratings in photorefractive elements are recorded between an unmodulated signal beam and the central carrier frequency of a phase modulated pump beam. The temporal frequency side bands, representing the

information content of the transmitted signal, are not altering the gratings due to the finite response time of the photorefractive materials. This grating "inertia" enables the use of such a system in the very high, GHz, frequency regime. During the operation, the system preserves its real-time phase-conjugation characteristics. Finally, the operation principle has been extended to a multi-beam scheme. Hologram multiplexing in a single crystal phase-conjugator operating in an adaptive transmitter mode serves to link information channels and presents a great potential in communications.

Semipermanent photorefractive recording has been demonstrated in BSO crystals using near infrared radiation. This semipermanent recording is observed and studied in combination with the usual dynamic behavior. No special fixing techniques or external electric fields are applied. A bipolar photorefraction theoretical model is incorporated and further developed to explain the experimental observations. On the basis of this model, a unique method for the determination of important materials parameters is proposed. The dynamic and semipermanent holograms coexisting in the same crystal volume have also been used for image processing applications and examples are presented. Illumination of the crystal with blue light causes redistribution of the active photorefractive centers thus enhancing the semipermanent recording features. This effect studied

and applied in the spatial sensitization of the material, enables the demonstration of incoherent-to-coherent spatial information transfer.

Dynamic holographic recording at the ultraviolet wavelengths has been successfully performed in polycrystalline In_2O_3 and In_2O_3:Sn thin films, grown either by DC-Magnetron sputtering, or by pulsed excimer laser deposition. This recording is characterized by a very large coupling strength which yields a diffraction efficiency of $\sim 10^{-4}$ for 300 nm thick films. The growth parameters for the PLD method have been investigated and optimized. Further work on this subject may involve control of recording and erasure characteristics as well as the systematic investigation of the holographic recording mechanism in these alternative materials.

This work represents a contribution towards the understanding of material-related issues influencing performance and efficiency as well as the development of new methods targeting to optical information storage and processing.

ANNEX 1

The band transport model

Assuming only electron photoconductivity, the band transport model is described by the following set of equations.

A continuity equation describing the charge balance inside the material

$$\frac{\partial n}{\partial t} = \frac{\partial N_D^+}{\partial t} + \frac{1}{e}\nabla \cdot \mathbf{J} \tag{1.1}$$

A rate equation giving the dynamics of the charge generation.

$$\frac{\partial N_D^+}{\partial t} = (\beta - sI)(N_D - N_D^+) - \gamma n N_D^+ \tag{1.2}$$

The current density is described by the following equation where the three terms represent contributions due to drift (first term), diffusion (second term) and the photovoltaic effect.

$$\mathbf{J} = e\mu n(E_{SC} - \frac{V}{L}) - k_B T \mu \nabla n + pI \tag{1.3}$$

Where: n= free electron number density

N_D = number density of donors

N_D^+ = number density of ionized donors

$\frac{V}{L} = E_0$: external applied electric field

t= time

s= free electron photoexcitation cross section

γ= free electron recombination rate

β= thermal electron excitation rate

e= electronic charge

J= electron current density

μ= mobility of the charge carriers

T= temperature

p= photovoltaic tensor

I= Intensity distribution inside the crystal (the result of the interference between two coherent beams)

The resulting space-charge field is given by the Poisson equation:

$$\nabla(\varepsilon_0 \varepsilon_r E_{SC}) = \rho = e(n + N_A - N_D^+) \qquad (1.4)$$

where: N_A is the number density of compensating acceptors and ρ is the density of charges.

In the absence of illumination the charge neutrality is expressed as:

$$n + N_A - N_D^+ = 0$$

ANNEX 2

PUBLISHED WORK

Journal Publications

"Pulsed amplification of CW signals in photorefractive $BaTiO_3$ "

N. A. Vainos, S. Mailis and M. C. Gower,

Appl. Phys. Lett.. 60 (13),1992

"Photorefractive adaptive transmission system"

S. Mailis and N. A. Vainos,

Appl.Opt.32, 1993.

"Multiplexed static and dynamic photorefraction at 780nm in $Bi_{12}SiO_{20}$"

S. Mailis, L. Boutsikaris and N.A.Vainos,

J. Opt. Soc. Am. B 11, 1996 (1994).

"Photorefraction at 780nm in $Bi_{12}SiO_{20}$ crystals: effects and applications"

S. Mailis, L. Boutsikaris and N. A. Vainos,

Asian Journal of Physics, 4 31 (1995)

"Holographic recording in indium oxide (In_2O_3) and indium tin oxide (In_2O_3:Sn) thin films".

S. Mailis, L. Boutsikaris, N. A. Vainos, C. Xirouhaki, G. Vasiliou, N. Garawal, G. Kyriakidis, and H. Fritzsche.

Appl. Opt. 69, 2459 (1996)

"Dynamic holography in indium oxide and indium-tin-oxide thin films"

S. Mailis, C. Grivas, D. Gill L. Boutsikaris, N. A. Vainos, C. Xirouhaki, G. Vasiliou, N. Garawal, G. Kyriakidis, and H. Fritzsche.

Optical Memory and Neural Networks 5(3), (1996)

Related Subjects

"Excimer laser use for microetching Computer Generated Holographic structures"

N. A. Vainos, S. Mailis, S. Pissadakis, L. Boutsikaris, P. Dainty, Ph. Parmitter and T. J. Hall.

Appl. Opt., 35, 6304 (1996).

"Fabrication of surface relief microstructures for optical interconnects by excimer laser microetching"

N. A. Vainos, S. Mailis, S. Pissadakis, L. Boutsikaris, P. Dainty, Ph. Parmitter and T. J. Hall.

Optical Memory and Neural Networks 5(4), (1996)

Conference presentations

"Multiplexed static and dynamic photorefraction at 780nm in $Bi_{12}SiO_{20}$"

S. Mailis and N. A. Vainos,

Proc 4th Inter. Conf. on Holographic Systems, Comp and Applications, Neuchatel Sept. 93.

"Photorefractive signal modulation and adaptive transmission",

S. Mailis and N. A. Vainos

Proc 4th Inter. Conf. on Holographic Systems , Comp and Applications, Neuchatel Sept. 93.

"Excimer laser Micromachining: Materials Reference Library and Microetching of Computer Generated Holographic Optical Interconnect Structures"

N. A. Vainos, S. Mailis, S. Pissadakis, P. Dainty and T. J. Hall.

Proc 4th Inter. Conf. on Holographic Systems , Comp and Applications, Neuchatel Sept. 93.

"Excimer laser microetching: microoptics & computer generated holography"

N. A. Vainos, S. Mailis, S. Pissadakis, N. Madamopoulos, L. Boutsikaris, G. Patrinos and A. Petrakis.

NATO ASI on EXCIMER LASERS: The tools, fundamental processes and applications. ELOUNDA, CRETE, GREECE, Sept. 6-17, 1993.

"Computer generated holographic diffractive structures fabricated by direct excimer laser microetching"

L. Boutsikaris, S. Mailis, S. Pissadakis, N. Madamopoulos, G. Patrinos, A. Petrakis, N. A. Vainos, P. Dainty, P. J. Parmitter and T. J. Hall.

Proc. SPIE 2403, 448, Photonics West 95 Conf. on Laser Induced Thin Film Processing San Jose, CA, USA. 1995

BIBLIOGRAPHY

[1] G. W. Stroke, "An Introduction to coherent optics and holography", Academic Press 1966

[2] D. Gabor, Proc. Roy. Soc. **A197** (1949)

[3] A. Ashkin, G. D. Boyd, J. M. Dziedzik, R. G. Smith, A. A. Ballman and K. Nassan, Appl. Phys. Lett. **9**, 72 (1966)

[4] F. S Chen, J. T. La Macchia, and D. B. Fraser, Appl. Phys. Lett. **13**, 223 (1968)

[5] F. S Chen, J. Appl. Phys. **40**, 3389-3396, (1969)

[6] N. V. Kukhtarev, V. B. Markov, S. G. Odulov and V. L. Vinetskii, Ferroelectrics, **22**, 949-960 (1979)

[7] M. G. Moharam, T. K. Gaylord, R. Magnusson, and L. Young, J. Appl. Phys. **50**, 4642 (1979)

[8] H. Kogelnik, The Bell System Technical Journal, **48**, 2909-2948 (1969)

[9] A. Yariv, IEEE Journal of Quantum Electronics, **9**, 650-660 (1978)

[10] M. Kaczmarek, R. W. Eason, M. H. Garrett and D. Rytz, Technical Digest of the conference on photorefractive materials, effects and devices, Estes Park. June 11-14, p 132, 1995

[11] "Photorefractive materials and their applications", Vol II, P. Gunter and J.-P. Huignard (Springer, Berlin-Heidelberg 1988) p 258.

[12] J. O. White, M. Cronin-Golomb, B. Fischer, A. Yariv, Appl. Phys. Lett. **40**, 450 (1982)

[13] J. Feinberg, Opt. Lett. **7**, 486 (1982)

[14] G. W. Ross, R. W. Eason, M. H. Garrett and D. Rytz, Opt. Comm. **101**, 60 (1993)

[15] G. W. Ross and R. W. Eason, Opt. Lett., **8**, 571 (1993)

[16] K. Meerholz, B. Volodin, S. Sandalphon, B. Kippelen and N. Payghambarian, Nature, **371**, 497 (1994)

[17] M. B. Klein, in "Photorefractive materials and applications" Vol I, (Springer, Berlin-Heidelberg 1988) Vol I, P. Gunter, J-P. Huignard Eds., p 195-236

[18] R. L. Townsend, J. T. La Macchia, J. Appl. Phys. **41**, 5188 (1970)

[19] S. H. Wemple, M. DiDomenico, Jr., I. Camlibel, J. Phys. Chem. Solids, **29**, 1797 (1968)

[20] "Principles and Applications of Ferroelectrics and Related Materials", M. E. Lines, A. M. Glass: Clarenton, Oxford 1977.

[21] V. Berlus, J Kalinajs, A. Linz, R. C. Folwailer, Mater. Res. Bull. **6**, 899 (1971)

[22] I. P. Kaminow, Appl. Phys. Lett. **7**, 123 (1965)

[23] S. Ducharme, J. Feinberg, R. R. Neurgaonkar, IEEE J. QE-**23**, 2116 (1987)

[24] A. R. Johnston, J. M. Weingart, J.Opt. Soc. Am. **55**, 828 (1965)

[25] I. P. Kaminow, Appl. Phys. Lett. **8**, 305 (1966)

[26] A. R. Johnston, Appl. Phys. Lett. **7**, 195 (1965)

[27] "Photorefractive materials and their applications", Vol II, P. Gunter, J-P. Huignard Eds., (Springer, Berlin-Heidelberg 1988) p 7.

[28] R. R. Neurgaonkar, K. Cory, R. Oliver, D. Ewbank and F. Hall, Opt. Eng. **26**, 392 (1987)

[29] J.-P. Huignard and P. Gunter in "Photorefractive materials and their applications", Vol II, (Springer, Berlin-Heidelberg 1988) p 67.

[30] J. P. Herriau, J. P. Huignard, P. Aubourg, Appl. Opt. **17**, 1851 (1978)

[31] C. G. Grankvist, Appl. Phys. A 57, 19 (1993)

[32] P. Nath, and R. F. Bunshah, Thin Solid Films, **69**, 63 (1980)

[33] K. L. Chopra, S. Major and D. K. Pandya, Thin Solid Films, **102**, 1 (1982)

[34] H. Fritzsche, B. Pasmakov, B. Claflin, Solar Energy Materials and Solar Cells, **32**, 383 (1994)

[35] S. Mailis, L Boutsikaris, N. A. Vainos, C. Xirouhaki, G. Vasiliou, N. Garawal, G. Kiriakidis and H. Fritzsche, Appl. Phys. Lett. **69**, 17 (1996)

[36] "Pulsed Laser Deposition of Thin Films" D. B. Chrisey, G. K. Hubler eds. Wiley (1994).

[37] H. M. Smith, and A. F. Turner, Appl. Opt. **4**, 147-148 (1965).

[38] D. Dijkkamp *et al.*, Appl. Phys. Lett., **51**, 619-621 (1987)

[39] X. D. Wu, *et al.*, Mater. Res, Soc. Symp. Proc., **191**, 129-140.

[40] J. S. Horwitz, K. S. Grabowski, D. B. Chrisey, and R. E. Leuchtner, Appl. Phys. Lett., **59**(13), 1565-1567

[41] R. Ramesh, *et al.*, Mater. Res, Soc. Symp. Proc., **191**, 129-140.

[42] S. Yilmaz, T. Venkatesan, and R. Gerhard-Multhaupt, Appl. Phys. Lett., **58**, 2479 (1991).

[43] K. E. Youden, R. W. Eason, M. C. Gower and N. A. Vainos, Appl. Phys. Lett., **59**, 1929 (1991)

[44] D. S. Gill, R. W. Eason, C. Zaldo, H. Rutt and N. A. Vainos, Journal of Non-Crystalline Solids, **191**, 321 (1995)

[45] Photorefractive Materials and their Applications I&II P. Gunter, J-P. Huignard Eds.,Springer, Berlin-Heidelberg, 1988.

[46] L. K. Lam, T. Y. Chang, J. Feinberg, and R. W. Hellwarth, Opt. Lett. **6**, 475 (1981).

[47] J. P. Hermann, J. P. Herriau, and J. P. Huignard, Appl. Opt. **20**, 2173 (1981).

[48] N. A. Vainos, S. Mailis and M. C. Gower, Appl. Phys. Lett. 60, 1529 (1992).

[49] F. P. Strohkendl, J. M. Jonathan, and R. W. Helwarth, Opt. Lett. **11**, 312 (1986).

[50] N. Barry and M. J. Damzen, J.Opt.Soc.Am B, **9**, 1488 (1992)

[51] N. A. Vainos, S. L. Clapham, and R. W. Eason, Appl. Opt. **28**, 4381 (1989).

[52] D. Mahgerefteh and J. Feinberg, Opt. Lett. **13**, 1111 (1988).

[53] M. C. Gower, Opt. Lett. 11, 458 (1986).

[54] "Photorefractive Materials and Their Applications I and II", P. Gunter and J.- P. Huignard (Eds). Springer- Verlag, Berlin (1990-1991).

[55] H. Rajbenbach, J.- P. Huignard, and Ph. Refregier, Opt. Lett., **9**, 558 (1984).

[56] N. A. Vainos, Opt. Lett., 14, 128 (1989).

[57] D.M. Lininger, P.J Martin and D.Z. Anderson, Opt. Lett., **14**, 697 (1989).

[58] Hisao Yoshinaga, Ken-ichi Kitayama, and Hitoshi Oguri, Opt. Lett., **9**, 669 (1991).

[59] D. Psaltis, D. Brady and K. Wagner, Appl. Opt. **27**, 1752 (1988)

[60] N. A. Vainos and M. C. Gower, Opt. Lett., **16**, 363 (1991).

[61] D. M. Pepper, Appl. Phys. Lett., **49**, 16, 1001 (1986).

[62] T. J. Hall, M. A. Fiddy, and M. S. Ner, Opt. Lett., **5**, 485 (1980).

[63] A. A. Kamshiling, E. V. Mokrushina, and M. P. Petrov, Opt. Eng. **28**, 580 (1989).

[64] S. I. Stepanov, in "International trends of optics", J. W. Goodman (Ed), Ch. **9**, p 125-140, Academic Press (1991).

[65] G. Hamel de Montchenault, B. B. Loiseaux, and J.- P. Huignard, Appl. Phys. Lett., **50**, 1794 (1988).

[66] G. Hamel de Montchenault, and J.- P. Huignard, J. Appl. Phys., **63**, 624 (1988).

[67] F. Davidson, and L. Boutsikaris, Opt. Eng., **29**, 369 (1990).

[68] J. Khoury, V. Ryan, C. Woods, and M. Cronin-Golomb, Opt. Lett. **16**, 1442 (1991).

[69] J. Khoury, V. Ryan, M. Cronin-Golomb, and C. Woods, J. Opt. Soc. Am. **B**, **10**, 72 (1993).

[70] S. Mailis and N. A. Vainos, Appl. Opt., **32**, 7285 (1993).

[71] S. I. Stepanov, and M. P. Petrov, "Photorefractive Materials and Their Applications I and II", P. Gunter, J-P. Huignard Eds., Springer- Verlag, Berlin (1990-1991) p 365-268.

[72] P. H. Refriegier, L. Solymar, H. Rajbenbach and J. P. Huignard,J. Appl. Phys., **58**, 45-57 (1985).

[73] G. Valley, Appl. Phys. **A**, **55**, 82-90 (1992)

[74] N. A. Vainos, and M. C. Gower, J. Opt. Soc. Am. **B**, **8**, 2355-2361 (1991)

[75] N. A. Vainos, S. Mailis, S. Pissadakis, L. Boutsikaris, P. Dainty, Ph. Parmitter and T. J. Hall. Appl. Opt., **35**, 6304 (1996).

[76] A. Marrakchi and W. M. Hubbard, Opt. Lett., **16**, 417 (1991)

[77] L. Arizmenti, J. Appl. Phys. **65**, 423 (1989)

[78] F. Micheron and G. Bismuth, Appl. Phys. Lett. **20**, 79 (1972)

[79] D. von der Linde, A. M. Glass and K. F. Rogers, Appl. Phys. Lett. **26**, 22 (1975)

[80] .J. P. Herriau and J. P. Huignard, Appl. Phys. Lett. **49**, 1140 (1986)

[81] M. C. Bashaw, T-P. Ma, R. C. Barker, S. Mroczkowski and R. R. Dube, Phys. Rev. B, **42**, 5461 (1990)

[82] M. Miteva and L. Nikolova, Opt. Comm. **67**, 192 (1988)

[83] D. Kirillov and J. Feinberg, Opt. Lett. **16**, 1520 (1991)

[84] S. Mailis, L. Boutsikaris, and N. A. Vainos, J. Opt. Soc. Am. B 11, 1996 (1994)

[85] S. Zhivkova and M. Miteva, J. Appl. Phys. **68**, 3099 (1990)

[86] M. C. Bashaw, T-P. Ma, R. C. Barker, S. Mroczkowski and R. R. Dube, JOSA B **7**, 2329 (1980)

[87] P. M. Jeffrey, S. C. Clapham, R. W. Eason, D. A. Fish, A. K. Powell, T. J. Hall and N.A.Vainos, Opt. Comm. **98**, 357 (1993)

[88] L. M. Bernardo, J. C. Lopez and O. D. Soares, Appl. Opt. **29**, 12 (1990)

[89] S. Zhivkova and M. Miteva, Opt. Comm. **86**, 499 (1991)

[90] F. P. Strohkendl, J. M. C. Jonathan and R. W. Hellwarth, Opt. Lett. **11**, 312 (1986)

[91] G. C. Valley, Appl. Opt. **22**, 3160 (1983)

[92] N. V. Kukhtarev, G. E. Dovgalenko and V. N. Starkov, Appl. Phys. A **33**. 227 (1984)

[93] G. C. Valley, J. Appl. Phys. **59**, 3363 (1986)

[94] S. Zhivkova, J. Appl. Phys **71**, 581 (1992)

[95] R. A. Mullen and R. W. Hellwarth, J. Appl. Phys. **58**, 40 (1985)

[96] G. Pauliat, J. M. C. Jonathan, M. Allain, J. C. Launay, and G. Roosen, Opt. Commun. 59, 266 (1986)

[97] M. Peltier, and F. Micheron, J. Appl. Phys. **48**, 3683 (1977)

[98] J. P. Huigrard and F. Micheron, Appl. Phys. Lett. **29**, 591 (1976)

[99] R. Grousson, M. Henry, and S. Mallick, J. Appl. Phys.**56**, 224 (1984)

[100] J. P. Huignard, J. P. Herriau and G. Rivet, Opt. Lett. **5**, 102 (1980)

[101] J.E. Dennis and D. J. Woods, New Computing Enviroments: Microcomputers in Large-Scale Computing, A. Wouk, ed. SIAM, 116(1987)

[102] G. Montemezzani, M. Zgonic and P. Gunter, J. Opt. Soc. Am. **B 10**, 171 (1993)

[103] Y. H. Ja, Opt. Comm. **42**, 377 (1982)

[104] N. A. Vainos, S. L. Clapham, and R. W. Eason, Appl. Opt. **28**, 4386 (1989)

[105] A. Marrakchi, A. R. Tanguay Jr, J. Yu, D. Psaltis, Opt. Eng. **24**, 124 (1985)

[106] S. L. Clapham, R. W. Eason and N. A. Vainos, Opt. Comm. **74**, 290 (1990)

[107] J. R. Bellingham, W. A. Phillips and C. J. Adkins, J. Phys. Cond. Matter. **2**, 6207 (1990)

[108] R. T. Chen and D. Robinson, Appl. Phys. Lett. **60**, 1541 (1992)

[109] H. Fritzsche, University of Chicago, James Frank Institute, Private communication

[110] M. C. de Andrade, S. Moehlecke, Appl. Phys. A **58**, 503 (1994)

[111] "Photorefractive Materials and their Applications" Vol I, P. Gunter and J-P. Huignard, (eds), (Springer, Berlin-Heidelberg 1988) p 178.